



Publicly Accessible Penn Dissertations


2017

Rate And State Friction Laws For Interfacial Chemical Bond-Induced Friction At The Nanoscale

Kaiwen Tian

University of Pennsylvania, kaiwentn@gmail.com

Follow this and additional works at: <https://repository.upenn.edu/edissertations>

 Part of the [Condensed Matter Physics Commons](#), [Mechanical Engineering Commons](#), and the [Nanoscience and Nanotechnology Commons](#)

Recommended Citation

Tian, Kaiwen, "Rate And State Friction Laws For Interfacial Chemical Bond-Induced Friction At The Nanoscale" (2017). *Publicly Accessible Penn Dissertations*. 2887.
<https://repository.upenn.edu/edissertations/2887>

This paper is posted at ScholarlyCommons. <https://repository.upenn.edu/edissertations/2887>
For more information, please contact repository@pobox.upenn.edu.

Rate And State Friction Laws For Interfacial Chemical Bond-Induced Friction At The Nanoscale

Abstract

Rate and state friction (RSF) laws are widely-used empirical relationships that describe macroscale frictional behavior of a broad range of materials, including rocks. Conventional RSF laws entail a linear combination of the direct effect (friction increasing with sliding velocity) and evolution effect (evolution of the state of the contact). One manifestation of evolution effect is "ageing", where static friction increases logarithmically with contact time. In order to understand the physical origins of RSF laws, we use atomic force microscope (AFM) to study nanoscale friction of silica, which is one important component of rocks. Overall, we observe RSF behavior, due to interfacial chemical bond-induced (ICBI) friction, which is manifested in several ways. The first aspect is the load and time dependence of ageing, whereby ageing magnitude increases approximately linearly with the product of the normal load and the log of the hold time. The second aspect is a physically-based RSF law we establish for single asperity contact, which we call the Prandtl-Tomlinson with temperature and evolution effect (PTTE) model. In PTTE model, the velocity for the direct effect is loading point velocity rather than tip velocity. Also, the combination of direct effect and evolution effect is nonlinear. The third aspect is the velocity dependence of kinetic friction, which reflects the competition of direct effect and evolution effect. Kinetic friction first decreases and then increases logarithmically with sliding velocity (the increase corroborates PTTE model). We explain the logarithmic decreasing by assuming that during low-velocity sliding, after an interfacial bond breaks, the resulting dangling bond can easily bond with other dangling bonds on the opposing surface. The fourth aspect is stick-slip, which could be better understood with PTTE model. We observe quasi-periodic stick-slip at lower velocities and uncover the velocity dependence of stick-slip. We also observe partial dropping of lateral force in some slip events in the transition regime between quasi-periodic stick-slip and smooth sliding, which corroborates the physical picture of dangling bonds forming interfacial bonds. In conclusion, these four aspects together demonstrate the nature of RSF behavior for nanoscale single-asperity contacts, and establish new, physically-based frictional laws for nanoscale contacts.

Degree Type

Dissertation

Degree Name

Doctor of Philosophy (PhD)

Graduate Group

Physics & Astronomy

First Advisor

Robert W. Carpick

Second Advisor

Joshua R. Klein

Keywords

Atomic force microscope, Chemical bonds, Friction, Nanotribology, Rate and state friction laws, Rock friction

Subject Categories

Condensed Matter Physics | Mechanical Engineering | Nanoscience and Nanotechnology

This dissertation is available at ScholarlyCommons: <https://repository.upenn.edu/edissertations/2887>

RATE AND STATE FRICTION LAWS FOR INTERFACIAL CHEMICAL BOND-INDUCED
FRICTION AT THE NANOSCALE

Kaiwen Tian

A DISSERTATION

in

Physics and Astronomy

Presented to the Faculties of the University of Pennsylvania

in

Partial Fulfillment of the Requirements for the

Degree of Doctor of Philosophy

2017

Supervisor of Dissertation

Robert W. Carpick, John Henry Towne Professor, and Department Chair, Mechanical Engineering and
Applied Mechanics

Graduate Group Chairperson

Joshua R. Klein, Professor, Physics and Astronomy

Dissertation Committee

Douglas J. Jerolmack, Graduate Chair & Associate Professor, Earth and Environmental Sciences

David L. Goldsby, Associate Professor, Earth and Environmental Sciences

Douglas Durian, Professor, Physics and Astronomy

Jay Kikkawa, Professor, Physics and Astronomy

Justin Khoury, Professor and Undergraduate Chair, Physics and Astronomy

RATE AND STATE FRICTION LAWS FOR INTERFACIAL CHEMICAL BOND-INDUCED
FRICTION AT THE NANOSCALE

COPYRIGHT

2017

Kaiwen Tian

ACKNOWLEDGEMENT

I would like to acknowledge all the support I've received for the past six years of my Ph.D. program. My father Xiaobing and my mother Qunhua have always been there for support. My adviser, Prof. Robert W. Carpick, has advised me in the past five years, and I will always be very grateful for his great guidance. I am also grateful to my mentor Prof. Nitya Gosvami. I'd like to thank my dissertation committee: Profs. David L. Goldsby, Douglas Durian, Douglas J. Jerolmack, Jay Kikkawa, and Justin Khoury. I also would like to thank my collaborators: Prof. Izabela Szlufarska, and Dr. Yun Liu. From the Carpick group: Xin Z. Liu, Qunyang Li, Prathima Nalam, Philip Egberts, Filippo Mangolini, Tevis Jacobs, Imene Lahouij, Harman Khare, Rodrigo Bernal, Frank Streller, James Hilbert, Joel Lefever, Brandon McClimon, Zachary Milne, Kathryn Hasz, Han Ye, and Charles Stovall.

In no particular order, I'd like to thank everyone else who's helped me along the way: Zhen Zheng, Wenxiang Chen, Qianyuan Tang, Swarmagent Club.

ABSTRACT

RATE AND STATE FRICTION LAWS FOR INTERFACIAL CHEMICAL BOND-INDUCED FRICTION AT THE NANOSCALE

Kaiwen Tian

Robert W. Carpick

Rate and state friction (RSF) laws are widely-used empirical relationships that describe macroscale frictional behavior of a broad range of materials, including rocks. Conventional RSF laws entail a linear combination of the direct effect (friction increasing with sliding velocity) and evolution effect (evolution of the state of the contact). One manifestation of evolution effect is "ageing", where static friction increases logarithmically with contact time. In order to understand the physical origins of RSF laws, we use atomic force microscope (AFM) to study nanoscale friction of silica, which is one important component of rocks. Overall, we observe RSF behavior, due to interfacial chemical bond-induced (ICBI) friction, which is manifested in several ways. The first aspect is the load and time dependence of ageing, whereby ageing magnitude increases approximately linearly with the product of the normal load and the log of the hold time. The second aspect is a physically-based RSF law we establish for single asperity contact, which we call the Prandtl-Tomlinson with temperature and evolution effect (PTTE) model. In PTTE model, the velocity for the direct effect is loading point velocity rather than tip velocity. Also, the combination of direct effect and evolution effect is nonlinear. The third aspect is the velocity dependence of kinetic friction, which reflects the competition of direct effect and evolution effect. Kinetic friction first decreases and then increases logarithmically with sliding velocity (the increase corroborates PTTE model). We explain the logarithmic decreasing by assuming that during low-velocity sliding, after an interfacial bond breaks, the

resulting dangling bond can easily bond with other dangling bonds on the opposing surface. The fourth aspect is stick-slip, which could be better understood with PTTE model. We observe quasi-periodic stick-slip at lower velocities and uncover the velocity dependence of stick-slip. We also observe partial dropping of lateral force in some slip events in the transition regime between quasi-periodic stick-slip and smooth sliding, which corroborates the physical picture of dangling bonds forming interfacial bonds. In conclusion, these four aspects together demonstrate the nature of RSF behavior for nanoscale single-asperity contacts, and establish new, physically-based frictional laws for nanoscale contacts.

TABLE OF CONTENTS

ACKNOWLEDGEMENT	III
ABSTRACT	IV
LIST OF ILLUSTRATIONS.....	X
CHAPTER 1: INTRODUCTION	1
1.1: Rate and state friction laws for macro and microscale contacts	1
1.2: Experimental studies of nanoscale interfacial chemical bond-induced ageing	13
1.3: Theoretical studies of nanoscale interfacial chemical bond-induced ageing.....	16
1.4: Motivations and overall review of the work in this project.....	20
1.5: List of papers and manuscripts in this project	20
CHAPTER 2: EXPERIMENTAL METHODS AND SAMPLE PREPARATION	22
2.1: Preparation of tips and substrates, and experimental setups.....	22
2.2: Characterizing the atomic force microscope tips used for the experiments	23
2.3: Calibration procedure	26

CHAPTER 3: LOAD AND TIME DEPENDENCE OF INTERFACIAL CHEMICAL BOND-INDUCED AGEING AT THE NANOSCALE	28
3.1: Experimental results for the load and time dependence of ageing	29
3.2: Derivation of the load and time dependence of ageing	31
3.3: Building models for the load and time dependence of ageing	33
3.3.1: The nonlinear model	33
3.3.2: The first stage of the linear approximation	34
3.3.3: The second stage of the linear approximation.....	41
3.4: Discussion regarding the value of τ_0.....	44
3.5: Possible relationship between nanoscale interfacial chemical bond-induced friction, macroscale friction, and the macroscopic rate and state friction laws	48
3.6: Discussions of the novelty and physical importance of this work	49
3.7: Discussions of the "step" in the data in Fig. 3.1(b).....	50
3.8: The validity of using Derjagin-Muller-Toropov model to establish the relationship of contact area and load.....	52
3.9: Summary.....	52
CHAPTER 4: A PHYSICALLY-BASED RATE AND STATE FRICTION LAW FOR NANOSCALE CONTACTS.....	54
4.1: Prandtl-Tomlinson with temperature model for atomic stick-slip	55

4.2: Prandtl-Tomlinson with temperature and evolution effect model for nanoscale interfacial chemical bond-induced friction.....	58
4.3: Experimental evidence for and discussions of the Prandtl-Tomlinson with temperature and evolution effect model	59
4.4: Summary.....	64
CHAPTER 5: KINETIC FRICTION AND MEMORY DISTANCE FOR INTERFACIAL CHEMICAL BOND-INDUCED FRICTION AT THE NANOSCALE	65
5.1: Velocity dependence of kinetic friction	66
5.2: A fundamental explanation of the logarithmic decrease of kinetic friction with velocity and the memory distance.....	71
5.3: Experimental results corroborating our explanation	74
5.4: Discussion of the dependence of single bond strength on loading point velocity.....	76
5.5: Variations of surface chemistry with time and location	77
5.6: Summary.....	80
CHAPTER 6: STICK-SLIP INSTABILITIES FOR INTERFACIAL CHEMICAL BOND-INDUCED FRICTION AT THE NANOSCALE.....	81
6.1: Experimental results of interfacial chemical bond-induced stick-slip friction at the nanoscale ...	81
6.2: Discussions on the experimental results	86

6.3: Summary.....	91
CHAPTER 7: CONCLUDING REMARKS AND OUTLOOK.....	93
7.1: Load and time dependence of interfacial chemical bond-induced ageing at the nanoscale.....	94
7.2: A physically-based rate and state friction law for interfacial chemical bond-induced friction at the nanoscale.....	95
7.3: Kinetic friction and memory distance for interfacial chemical bond-induced friction at the nanoscale	96
7.4: Stick-slip instabilities for interfacial chemical bond-induced friction at the nanoscale.....	98
7.5: Outlook	99
BIBLIOGRAPHY	104

LIST OF ILLUSTRATIONS

Fig. 1.1. (a) Schematic of the spring-block model. (b) Schematic of VS test.

Fig. 1.2: A typical SHS test for quartz gouge. The slide, hold, and slide regimes are shown. During hold, the lateral force (*i.e.*, the spring force) drops, due to the relaxation of the system.

Fig. 1.3: A typical ageing result of rocks. It could be seen that the coefficient of static friction increases logarithmically with contact time, from 1 s to 10^5 s.

Fig. 1.4: The evolution term vs. time according to the solution to the slowness law (when $v > 0$). Here $t_c = \frac{D_c}{v}$. The solution is $\theta(t) = \frac{D_c}{v} (1 - \frac{A}{D_c} e^{-\frac{vt}{D_c}})$, and $\ln(1 - \frac{A}{D_c} e^{-\frac{vt}{D_c}})$ is used to represent the evolution term. Six different $\frac{A}{D_c}$ values are used. Generally speaking, the evolution term increases almost logarithmically with time at middle times, and saturates at large times. Except for $A = D_c$, where the evolution term is almost linear with time at small times, the evolution term levels-off (for a logarithmic plot) at small times for all other $\frac{A}{D_c}$ values.

Fig. 1.5: The plot of $\ln(1 + \frac{t}{\tau})$ vs. t where $\tau = 1$ s. This function describes the evolution effect, *i.e.*, the third term in Eq. 1.1, as a function of time for small v . The transition between the logarithmic dependence at large times and the behavior at small times (which appears like a leveling-off on a logarithmic plot) is around the value of τ (1 s).

Fig. 1.6: Kinetic friction vs. sliding velocity for PMMA on silanized glass contacts. The kinetic friction first decreases then increases with velocity logarithmically.

Fig. 1.7: Shear stress vs. time in a typical rock friction experiment. Three different loading point velocities are used. It can be observed that the stick-slips are quasi-periodic, and both the amplitude and recurrence of stick-slip decrease with loading point velocity.

Fig. 1.8: Stress drop vs. recurrence interval of stick-slip for different loading point velocities. Data from experiments on quartz powders. It can be observed that, under a given normal pressure, the stress drop data fall into different clusters corresponding to different loading point velocities. In every cluster the stress drop increases logarithmically with recurrence interval; for all clusters the stress drop also increases logarithmically with the recurrence interval but with a different increasing rate.

Fig. 1.9: Schematic of AFM. The base of the cantilever is controlled by a piezoelectric scanner. The laser beam is shone on the back of the cantilever and reflected to a four-quadrant photo detector. The lateral force on the tip twists the cantilever, which is read as the lateral signal on the photo detector. The normal force (*i.e.* the applied load) will cause normal bending of the cantilever which is read as the normal signal on the photo detector.

Fig. 1.10: Lateral force vs. lateral displacement (of the loading point) for four different hold times, ranging from 0.1 s to 100 s. The inset shows the logarithmic dependence of the friction drop on hold time. The hold time is varied randomly to exclude systematic errors.

Fig. 1.11: Normalized friction vs. lateral displacement from three sequential SHS tests. Hold time = 100 s, RH = 40 %. Ageing is largely suppressed after the tip is lifted out of contact for a while. The magnitude of ageing recovers after run-in scans are performed.

Fig. 1.12: SHS tests between silica tips and three different surfaces. Hold time = 100 s, RH = 60 %. Only the silica-silica contact exhibits significant ageing.

Fig. 1.13: Schematic of interfacial siloxane bond formation.

Fig. 1.14: Histogram of interaction energy in the simulation.

Fig. 1.15: Siloxane concentration vs. time for different initial barrier distribution. (a) - (c) show three different initial barrier distributions (blue curves): pressure-induced (*i.e.*, due to the distribution of pressure on the surfaces), geometry-induced (*i.e.*, due to the distribution of distances between neighboring silanol groups on opposing surfaces), and from MD simulations. The dark red curves are the distributions before ageing. (d), (e) and (f) correspond to (a), (b) and (c) respectively. The green curves are with interactions, while the bright red curves are without interactions. With interactions, all three initial barrier distributions result in logarithmic ageing with time from 0.1 s to 100 s, which is consistent with AFM experiments.

Fig. 2.1: TEM image of a typical AFM tip used before experiments. The tip radius is about 130 nm. We do not have TEM images of tips after each experiment in this thesis.

Fig. 2.2: The topographic scan images (a) and (b) of a typical tip on a UNCD substrate and the tip profiles (c) and (d). The tip was scanning on a piranha-cleaned silica substrate for approximately 6.8 mm between the measurement in (a) and the measurement in (b). Plots (c) and (d) are cross-sectional profiles of the tip in fast scan direction as determined by the SPIP software, corresponding to (a) and (b) respectively. The blue curves are the tip profile and the red curves are parabolic fit. The tip radius is measured to be 105 ± 15 nm and 166 ± 14 nm respectively in (a)/(c) and (b)/(d). It could be seen from (d) that after sliding for 6.8 mm, the tip surface is still not flat, and could be fitted by a parabola well.

Fig. 3.1: Effect of hold time and applied normal load on static ageing. Relative humidity (RH) = 53%, temperature $T = 24$ °C and the loading point velocity is 500 nm/s. **(a)** Friction drop vs. log of hold time for different normal loads. The inset shows the lateral force vs. lateral displacement curve from the test for 100 s hold time and 23 nN applied load, and indicates how we measure friction drop. The linearity of friction drop vs. log of hold time is seen for all normal loads. **(b)** The slope of each linear fit in **(a)** vs. load. The slope varies linearly with load. **(c)** Friction drop vs. load for different hold times. For a given hold time, friction drop increases linearly with load. **(d)** The slope of the linear fits from **c** vs. log of hold time. The slope increases linearly with log of hold time. Loads and hold times are varied randomly to exclude systematic errors.

Fig. 3.2: Extracting L_0 and τ_0 from Fig. 3.1. To obtain L_0 , all the data points in Fig. 3.1 (a) are divided (normalized) by $(L+L_0)^{\frac{2}{3}}$, and then L_0 is varied so that all the data points converge as closely as possible into one master curve. To do this, for a given L_0 and hold time, we calculate the mean value and standard deviation of $\Delta F/(L+L_0)^{\frac{2}{3}}$ for the data from all six applied loads L . We then divide the standard deviation by the mean value to obtain the relative standard deviation. Finally, we calculate the average value of this relative standard deviation over all four hold times. (a) shows the dependence of this average relative standard deviation on L_0 , with the global minimum point seen to be $L_0 = 253 (\pm 4)$ nN, which is the extracted value of L_0 . (b) shows the normalized friction drop vs. log of hold time when $L_0 = 253$ nN. For τ_0 , similar to the procedure for determining L_0 , we divide all the data points in Fig. 3.1 (c) by $[2.3\log(t) - 2.3\log(\tau_0) + 0.58]$. We then tune τ_0 to make all the data points converge with minimal deviation onto one master curve in the same manner as for L_0 . (c) shows the dependence of the average relative standard deviation on τ_0 , with the global minimum point seen to be $\tau_0 = 0.033 (\pm 0.001)$ s, *i.e.*, $\log(\tau_0) = -1.48 (\pm 0.03)$, which is the extracted value of τ_0 . (d) shows the normalized friction drop vs. load when $\tau_0 = 0.033$ s.

Fig. 3.3: Fitting of friction drop vs. load for all 4 hold times. The fitting is according to Eq. (3.7). It can be extracted from the fitting that for 0.1 s hold time, $G_0 = (1.06 \pm 0.21)$ eV, $V_0 = (78 \pm 28)$ Å³; for 1 s hold time, $G_0 = (0.32 \pm 0.05)$ eV, $V_0 = (-8.5 \pm 5.4)$ Å³; for 10 s hold time, $G_0 = (0.23 \pm 0.05)$ eV, $V_0 = (-11.9 \pm 5.4)$ Å³; for 100 s hold time, $G_0 = (0.41 \pm 0.14)$ eV, $V_0 = (11 \pm 15)$ Å³.

Fig. 3.4: Kinetic friction vs. normal load. The silica substrate was cleaned with piranha solution before experiment. The load is systematically varied from 0 to 325 nN.

Fig. 3.5: Distributions of reaction barriers (left column) and the corresponding time evolutions of normalized ageing (right column). Reaction barrier distributions are (a1) pressure-induced distribution, where reaction energy barrier is controlled by atomic pressure; (b1) geometry-controlled distribution, where the orientation of hydroxyl groups on the surface determines the barrier; and (c1) distribution directly calculated from MD simulations. In (a2)-(c2), red lines and blue lines represent time evolutions of ageing amplitude with and without considering interactions between neighboring siloxane bridges, respectively. Static friction of 1.0 corresponds to the strength of the interface when all siloxane bonds are formed and are independent of each other (*i.e.*, there is no decay of strength).

Fig. 3.6: Dependence of the slope of friction drop vs. log of hold time on load after omitting the data associated with the 100 s hold time in Fig. 3.1(a).

Fig. 4.1: PTT model. (a) Schematic of PTT model. The total potential energy is the sum of the tip-substrate interaction potential and the spring potential. In the inset on the top, the tip/block-spring model is shown with spring stiffness k_{eff} and loading point velocity v . The tip-substrate interaction potential is modelled as sinusoidal with the barrier height being ΔE^* . For the total potential energy, the energy barrier under an applied lateral force is ΔE . For nonzero temperatures, thermal fluctuations assist the system in jumping over the energy barrier even when $\Delta E > 0$. (b) Typical friction vs. velocity data from atomic stick-slip experiments. The logarithmic increase, transition and plateau regimes could be seen.

Fig. 4.2: Lateral force vs. lateral displacement for two loading point velocities. Both original data and the smoothed curves (to reduce noise) are shown. The measurement of the maximum static friction, the kinetic friction and the friction drop are also shown. At the larger loading point velocity, the maximum static friction and the kinetic friction are both larger. RH = 45 %, temperature = 24 °C, applied normal load = 149 nN, adhesion = 682 nN, hold time = 4.64 s.

Fig. 4.3: Friction vs. log of velocity for different hold times. (a) Results showing the maximum static friction, kinetic friction, and friction drop vs. loading point velocity for a 1.28 s hold time. Both show a logarithmic increase with v . The friction drop happens to be almost independent of velocity since the slope of the maximum static friction and kinetic friction with log of velocity are the same. (b) Results showing the maximum static friction, kinetic friction, and friction drop depend on loading point velocity for a 4.64 s hold time. The maximum static friction, kinetic friction, and friction drop all increase with velocity logarithmically (the slope of the maximum static friction with log of velocity is rather different than that of the kinetic friction, resulting in a clear dependence of the friction drop on v). For both (a) and (b), the loading point velocity is varied randomly to exclude systematic error. The conditions are the same as those in Fig. 4.2, and the same tip is used.

Fig. 5.1: The dependence of kinetic friction on sliding velocity in the steady sliding regime. Kinetic friction first decreases linearly with the log of velocity, and then increases linearly with log velocity. (a) Results showing a logarithmic decrease in friction, followed by a logarithmic increase in friction. (b) Another result showing the logarithmic decrease in friction with velocity which levels off, presumably prior to an increase that would occur at higher velocities. (c) Another result showing the tail end of the logarithmic decrease of friction with velocity, followed by a logarithmic increase. The tips and conditions

given in the insets are different in (a), (b), and (c). For each test, the velocity is varied randomly to exclude systematic errors.

Fig. 5.2: Measurement of the transition velocity where the dependence of the kinetic friction on velocity deviates from logarithmic. (a) corresponds to Fig. 5.1(a) and (b) corresponds to Fig. 5.1(b). (c), (d) and (e) are from additional tests. In (a), the left-most five points are fit linearly and extended with a dashed red line, with a velocity of the fifth point of 27 nm/s. The y-value of the horizontal dashed blue line is the mean value of the kinetic friction of the lowest three points. The dashed blue line and dashed red line intersect at 47 nm/s. Thus, we estimate that the transition velocity in (a) is between 27 and 47 nm/s, as indicated in the light yellow colored region. In (b), the leftmost four points are fit linearly, and extended with a dashed red line, with a velocity of the fourth point of 10 nm/s. The y-value of the horizontal dashed blue line is the mean value of the kinetic friction of the two rightmost points. The dashed blue line and dashed red line intersect at 68 nm/s. Therefore, we estimate a transition velocity in (b) between 10 nm/s and 68 nm/s. In (c), the leftmost three points are fit linearly, and extended with a dashed red line, with a velocity of the third point of 5 nm/s. The y-offset of the horizontal dashed blue line is the mean value of the kinetic friction of the rightmost two points. The dashed blue line and dashed red line intersect at 25 nm/s. Thus, we estimate that a transition velocity in (c) between 5 nm/s and 25 nm/s. In (d), the leftmost nine points are fit linearly, and extended with a dashed red line, with a velocity of the ninth point of 32 nm/s. The y-offset of the horizontal dashed blue line is the mean value of the kinetic friction of the lowest three points. The dashed blue line and dashed red line intersect at 40 nm/s. Thus, we estimate a transition velocity in (d) between 32 nm/s and 40 nm/s. In (e), the leftmost three points are fit linearly, and extended with a dashed red line, with a velocity of the fifth point of 50 nm/s. The y-offset of the horizontal dashed blue line is the mean value of the kinetic friction of the lowest three points. The dashed blue line and dashed red line intersect at 295 nm/s. Thus, we estimate that the transition velocity in (e) is between 50 nm/s and 295 nm/s.

Fig. 5.3: Results of a static ageing test. The contact time is the sum of hold time and stick time. The hold time is varied randomly to exclude systematic errors. The tip and conditions are the same as those in Fig. 5.1 (c), and the test was conducted just before the test in Fig. 5.1 (c). The static friction for the 1 s hold time (which is measured at the beginning of the test, and is 253.5 ± 8.3 nN) is only 6.5% different than the static friction for 1 s hold time (271.2 ± 7.4 nN) measured immediately after the test done in Fig. 5.1 (c) indicating that there were no significant surface chemistry changes between these two tests. The dependence of ageing on time deviates from logarithmic between 0.1 s and 1 s. The red curve is a fit to the function $F = F_0 + g \cdot \log(1 + \frac{t}{\tau})$, where F is the static friction, F_0 is the offset of static friction, g is a constant, and τ is some characteristic transition time. As discussed in Section 1.1, this form of the RSF law avoids the singularity when t approaches zero. The value of τ extracted in this way is 0.058 ± 0.025 s. We comment that the transition time extracted in this way is expected to be smaller than the time where the ageing vs. time begins to deviate from the logarithmic trend.

Fig. 5.4: Schematic of the life cycle of reaction sites. The silicon atom of reaction site X is colored blue. From (a) to (e), the tip continuously moves to the right with equal displacement between each successive figure, followed by a larger displacement between (e) and (f). The dashed blue line is to guide the eye. In (a) to (e) the same region of the substrate is shown. (f) corresponds to the configuration wherein the tip has moved a distance D_C and site X becomes passivated, and represents a different region of the substrate than the one shown in (a) through (e).

Fig. 5.5: Stick-slip in the quasi-periodic regime and the transition regime. (a) A representative lateral force vs. lateral displacement curve in the quasi-periodic stick-slip regime, well below the velocity at which the transition from stick-slip to steady sliding occurs. The stick-slip period and amplitude are highly regular. (b) A representative force vs. lateral displacement curve for the same tip under the same conditions, for which the sliding velocity is in the transition regime between stick-slip and steady sliding. The stick-slip

events are less periodic than those in (a). Additionally, for some slip events, the lateral force only drops partially. Two representative partial-slip events are labeled in dashed blue ellipses.

Fig. 5.6: Static friction vs. the time when static friction measurements are performed, measured for the same tip at the same nominal location on the sample. The hold time is 4.6 s for each static ageing test. $T = 24\text{ }^{\circ}\text{C}$, $\text{RH} = 52\%$, applied load = 26 nN, adhesion = 497 nN. The mean static friction forces are $98.0 \pm 5.2\text{ nN}$, $77.1 \pm 4.0\text{ nN}$, and $70.4 \pm 5.5\text{ nN}$ for times of 0 min, 22 min, and 30 min respectively. The static friction decreases about 28 % with 30 mins, attributed to the adsorption of contaminants on the substrate. Other SHS tests were performed between these three static ageing tests, so the tip was scanning on the substrate during a portion of the time intervals during these 30 mins. The substantial decay of static friction indicates that these scans are not sufficient to remove contaminants and prevent static friction from dropping significantly. The inset shows a typical lateral force vs. lateral displacement curve at time 0 min.

Fig. 5.7: Lateral force scan map showing stick-slip events. $\text{RH} = 40\%$, $T = 24\text{ }^{\circ}\text{C}$, load = 130 nN, adhesion = 88 nN. The fast scan direction is from left to right, and the slow scan direction is from top to bottom. The scan size is $400\text{ nm} \times 400\text{ nm}$. The scan speed is 1000 nm/s. The heterogeneity of stick-slip amplitude and spatial period can easily be seen in both fast and slow scan directions.

Fig. 6.1: Lateral force vs. lateral displacement under two loads. The loading point velocity is 95 nm/s, $T = 24\text{ }^{\circ}\text{C}$, $\text{RH} = 80\%$, hold time = 0.1 s, the adhesion is undetermined (at least 976 nN). The measurements of the peak force, lowest force and stick-slip amplitude are shown. It could be seen that the stick-slip is quasi-periodic, and the stick-slip amplitude and spatial period increase with load.

Fig. 6.2: Lateral force vs. lateral displacement for different loading point velocity. $T = 24\text{ }^{\circ}\text{C}$, $\text{RH} = 42\%$, hold time = 0.1 s, applied normal load = 65 nN, the adhesion is undetermined. The stick-slip amplitude and spatial period decreases with the loading point velocity, and the stick-slip transitions to smooth sliding when the velocity is large enough. The velocity is varied randomly to exclude systematic errors.

Fig. 6.3: stick-slip behavior under varying loading point velocities. The tip and conditions are the same as that in Fig. 6.2. (a) Peak force vs. log of temporal period. With decreasing period, the peak force decreases with log of period linearly, and deviates from this dependence below a period between 0.1 s and 1 s. (b) Dependence of peak force and lowest force on loading point velocity. The peak force first decreases with velocity logarithmically, and then levels off, while the lowest force is nearly independent of velocity. (c) Power law scaling of the temporal period with velocity, with an exponent of -1.41 ± 0.02 . The velocities are varied randomly to exclude systematic errors.

Fig. 6.4: Another set of data on stick-slip behavior under varying loading point velocities. $T = 24\text{ }^{\circ}\text{C}$, $\text{RH} = 80\%$, applied load = 819 nN, and the adhesion is undetermined (due to being too large to measure; it was at least 834 nN). (a) Peak force vs. log of period (in time). With decreasing period, the peak force decreases with log of period linearly, and begins to deviate below a period between 0.1 s and 1 s, consistent with the data in Fig. 6.3. The inset shows a typical quasi-periodic stick-slip result. (b) Dependence of peak force and lowest force on loading point velocity. The peak force first decreases with velocity logarithmically, and then begins to level off, while the lowest force is nearly independent of velocity. This is consistent with the data in Fig 6.3. (c) Power law scaling of the period and velocity, with an exponent of -1.67 ± 0.03 . The velocities are varied randomly to exclude systematic errors.

Fig. 6.5: Power law scaling of stick-slip period and velocity.

Fig. 6.6: Schematic of the velocity (a) and load (b) dependence of stick-slip. The vertical axis is lateral force, *i.e.*, either the static friction at the interface (the force required to initiate slip), or the force in the spring (due to its elongation). The horizontal axis is time. For both (a) and (b), the labeled solid red curves

show how the static friction and the spring force evolve with time, for a given loading point velocity, under a given load. For simplicity, the initial spring force is set to 0. The curve along points JEA represents how static friction increases with time. The line segment OA shows how the spring force increases with time, with the slope proportional to the effective stiffness. At point A, the spring force reaches the static friction force, the tip slips and the spring force drops, following the dashed red line from A to B. Since slips are usually extremely fast in AFM, segment AB is drawn as a vertical line. The horizontal segment BD represents the resetting of the time axis so that the system starts the next cycle at point D, with the spring force maintained at the value at the end of the last slip event (point B). Segment DE represents the second stick. When the spring force reaches the static friction force this time (point E), slip again occurs and the spring force drops from E to C. Point C is chosen to lie on segment BD, since the lowest forces in each slip event are assumed to be the same, based on our experimental results (Figs. 6.2 and 6.3(b)). The starting spring force of the third stick is the same as the second stick (*i.e.*, also at point D). Therefore, subsequent stick-slips will repeat regularly, producing the regular periodicity observed in experiments. The length of AB is larger than EC, thus, the observation that the peak force of the first stick is larger than the peak forces of the subsequent sticks is explained by this model. (a) The green curves show the spring force for a higher loading point velocity than that for the red curves (the static friction force vs. time remains the same, *i.e.* the curve lying along points JEA). Since the velocity is higher than in the case of the red curves, the slope of the spring force vs. time (segment OF) is greater, but the evolution of static friction with time is unaffected. Therefore, the system reaches the point of slip at an earlier time and a lower static friction force. This explains the experimental observation that the greater the loading point velocity, the smaller the static friction force. Since the effective stiffness is independent of velocity (Fig. 6.2), the spatial period of stick-slip is thus smaller at higher velocity (*i.e.* the time elapsed for segment OF is smaller than for OA, and likewise is smaller for DI than for DE). Slip then occurs at point F, and the cycle repeats as described for the red curve (segments DIH). (b) The labeled blue curves show the evolution of the static friction (lying along points QPK) and spring force (segments OK and NP) under a higher load. Here we assume that increasing the load magnifies the static friction values by a multiplicative factor, consistent with experimental observations [1]. Since the effective stiffness is independent of load (Fig. 6.1), the segment representing the spring force during the sticking phase for both loads, OK and OA, must overlap. Since the stick-slip amplitude and spatial period are larger for higher load according to Fig. 6.1, the length of PM is larger than EC, and MN larger than CD. Slip then occurs, and the cycle repeats as described for the red curve.

Fig. 7.1: Friction drop vs. effective contact time. Relative humidity (RH) = 80 %, applied normal load = 332 nN, adhesion undetermined (at least 976 nN), temperature $T = 24$ °C and the loading point velocity is 1.53 $\mu\text{m/s}$. The upper left inset shows the data points from *ca.* 5 ms to 0.11 s, with linear time scale. It could be seen that the friction drop increases linearly with effective contact time from *ca.* 5 ms to 0.09 s. The linear fitting line is the red solid line in the inset. It could also be seen that data points for contact time 1 s, 10 s, and 100 s fall nicely on a linear fitting line, which is the red solid line in the main plot and is extended by a red dashed line. The data points for the contact time of 0.1 s are clearly above this red dash line. It could thus be estimated that the transition time where the logarithmic dependence of ageing on time ends is between 0.1 s and 1 s. The lower right inset shows one lateral force vs. lateral displacement curve for 0.07 s hold time. The hold times are varied randomly to exclude systematic errors.

Fig. 7.2: Contact area vs. contact time of quartz in nanoindentation tests. The dark gray, black, and light gray data points correspond to loads of 15 mN, 50 mN and 150 mN respectively. The fractional contact area (the ratio of newly formed area over the initial area) increases with contact time logarithmically between 1 s and 10,000 s.

Chapter 1: Introduction

1.1: Rate and state friction laws for macro and microscale contacts

Friction is important in a wide range of technological, industrial, biological, and natural systems [2-15]. One of the most general approaches describing macroscale friction is the rate and state friction (RSF) formalism [6, 16-29]. Often deemed a "law", RSF models are empirical, lacking a complete physical basis. In spite of this, RSF models fit friction data for a remarkably wide range of materials including paper [30], organic monolayer-coated microelectromechanical systems [5, 31, 32], granular media [24, 33], and rocks [6, 16, 18, 24, 30, 34, 35]. For a macroscopic sliding block, the mathematical expression for the coefficient of friction μ as a function of contact time t and block velocity v_{block} from the RSF law is given by:

$$\mu(t) = \mu_0 + a \ln \frac{v_{block}}{v_0} + b \ln \left(\theta(t) \frac{v_0}{D_C} \right) \dots\dots\dots(1.1)$$

where v_0 is a reference velocity, μ_0 is the reference friction coefficient corresponding to v_0 , D_C is a length scale known as the memory distance, which is the length a population of contacts must slide in order to refresh itself, and θ is called the "state variable" which is a function of time. The state variable represents the state of the contact and is modelled using different relations depending on the specific RSF model being followed. The behavior described by the second term in Eq. (1.1) is called the "direct effect", whose physical basis lies in the fact that thermal energy assists sliding more strongly at slower velocities [36]. The behavior described by the third term is called the "evolution effect", in which θ evolves with the duration of interaction at the sliding interface. The factors a and b represent the magnitudes of the direct and evolution effects, respectively.

In rock friction experiments, the system (including the rock substrate, the rock block, and the instrument) can be simply represented by a spring-block model, as shown in Fig. 1.1 (a). The stiffness of the spring in this schematic is the total stiffness of the system.

The physical meaning of each parameter in Eq. (1.1) can be seen in the schematic of a velocity-stepping (VS) test (Fig. 1.1 (b)), which is a commonly employed test in the study of rock friction. In VS tests, the block initially slides on the substrate with velocity v_1 (which is also the loading point velocity). At a certain time, the loading point velocity is suddenly increased to v_2 ($v_2 > v_1$). Since the stiffness of the system is usually relatively large, the sliding velocity of the block will also immediately jump to v_2 . A sudden jump of the lateral force (measured by the spring) is observed and its magnitude is represented by a . After the jump, the lateral force gradually decreases to a new steady value which can be either higher or lower than the friction observed at the lower velocity. In the case shown in Fig. 1.1, steady state friction at the higher velocity v_2 is lower than at v_1 , which is called "velocity weakening" behavior, a necessary condition for frictional instability and, ultimately, earthquakes. The characteristic decay distance is D_c , and the magnitude of the decay from the peak to the new steady lateral force, is represented by b .

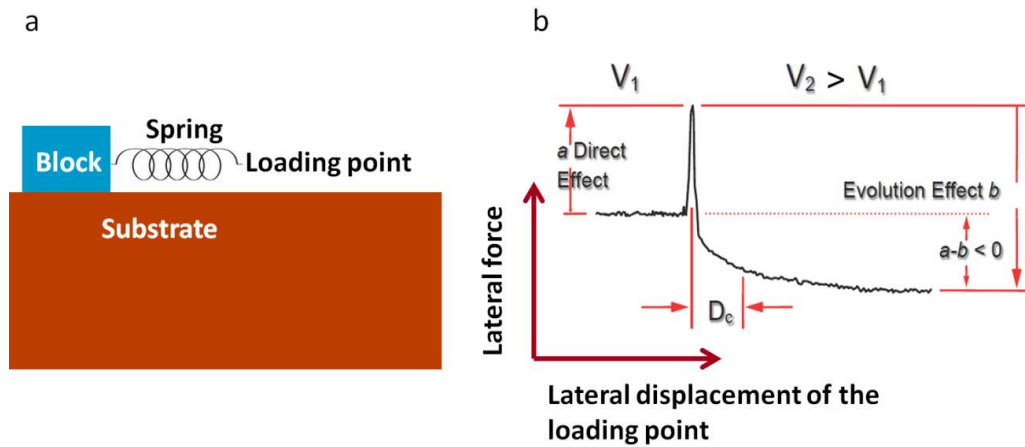


Fig. 1.1. (a) Schematic of the spring-block model. (b) Schematic of VS test. From Goldsby *et al.* [37].

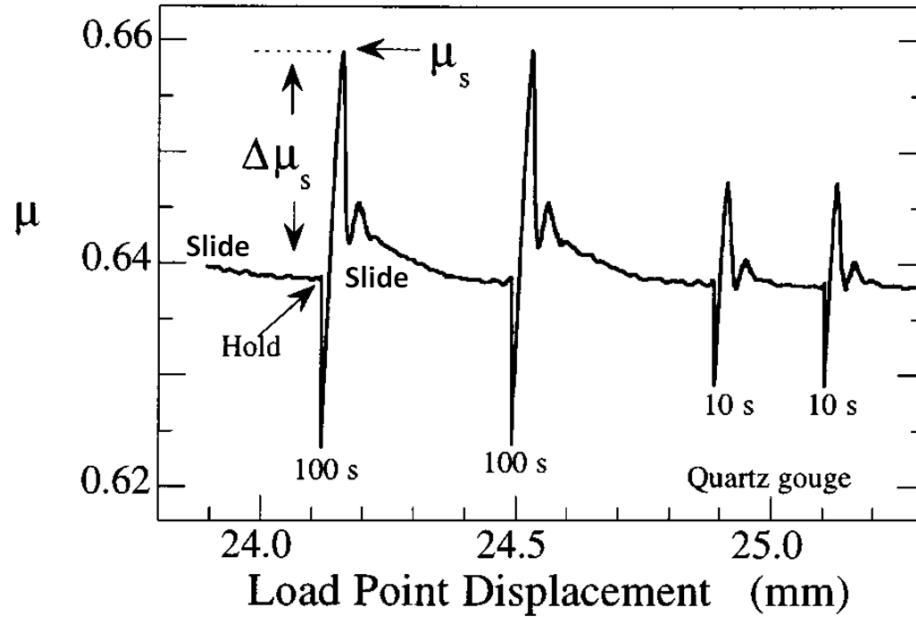


Fig. 1.2: A typical SHS test for quartz gouge. The slide, hold, and slide regimes are shown. During a hold, the lateral force (*i.e.*, the spring force) decreases, due to the relaxation of the system. From Marone [6].

One manifestation of the evolution effect is the logarithmic increase of static friction with hold time, *i.e.* the time in static contact before sliding in SHS tests. Known as “ageing”, this effect has been observed in many macroscopic rock friction experiments for a range of conditions for hold times from 1 to 10^5 s [6, 16, 17, 38]. One typical ageing result for rocks is shown in Fig. 1.3. Two ageing mechanisms have been proposed. The first is an increase in real contact area (to which friction is often directly proportional [39, 40]) with time, due to plastic creep of asperity contacts, referred to as an increase in “contact quantity”. The second is due to the formation of chemical bonds across the frictional interface, causing an increase in friction, without any change in the contact area, sometimes referred to as an increase in “contact quality”. At the macroscale, multiple mechanisms may contribute to friction simultaneously, making it difficult to deconvolve their effects. This is one reason why macroscopic RSF laws remains largely empirical in form.

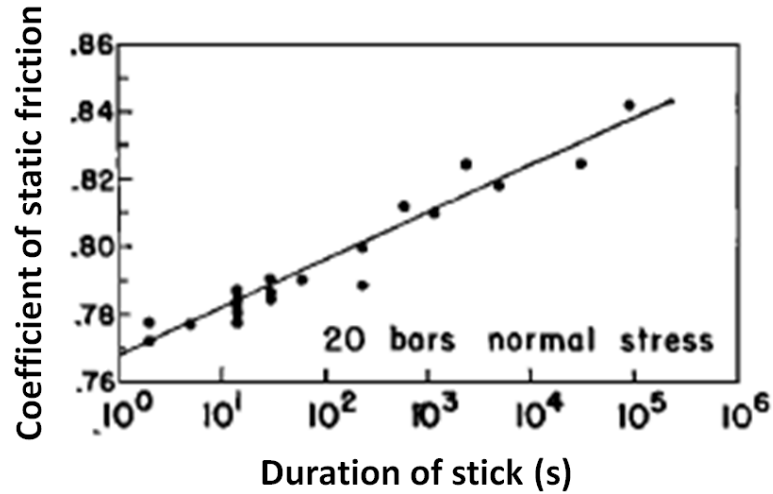


Fig. 1.3: A typical ageing result for rocks. The coefficient of static friction increases logarithmically with contact times of from 1 s to 10⁵ s. From Dieterich [16].

This logarithmically increasing trend of friction with time is well fit by the empirical slowness law (sometimes called the Dieterich law):

$$\frac{d\theta}{dt} = 1 - \frac{v\theta}{D_c} \dots\dots\dots(1.2)$$

which describes the evolution of the state variable with contact time (or hold time) during the hold portion of slide-hold-slide (SHS) tests on rocks. In those tests, the block of rock initially slides on the rock substrate at a given velocity, after which the loading point velocity is set to zero. The block remains in quasi-stationary contact with the substrate for a specified time, after which the loading point velocity is fixed at the prehold value, and sliding resumes. During reloading, a peak in the friction force is observed, and with further sliding friction returns to the value observed prior to the hold. A typical result of a SHS test, in this case on quartz powders, is shown in Fig. 1.2. The force drop after the hold starts in Fig. 1.2 is due to relaxation of the system.

Eq. (1.2) could be easily solved analytically, with the solution $\theta(t) = \frac{D_c}{v} \left(1 - \frac{A}{D_c} e^{-\frac{vt}{D_c}}\right)$ when $v > 0$. Here A is a positive constant. If we set $\frac{D_c}{v} = t_c$, then $\theta(t) = t_c \left(1 - \frac{A}{D_c} e^{-\frac{t}{t_c}}\right)$. Therefore, the evolution effect term becomes $b \ln \left(\theta(t) \frac{v_0}{D_c}\right) = b \ln \left(\frac{v_0}{D_c} t_c \left(1 - \frac{A}{D_c} e^{-\frac{t}{t_c}}\right)\right) \propto \ln \left(1 - \frac{A}{D_c} e^{-\frac{t}{t_c}}\right)$. For all $t > 0$, in order to make certain the argument of the logarithmic function is positive, this relationship must be satisfied: $A \leq D_c$. The behaviors of $\ln \left(1 - \frac{A}{D_c} e^{-\frac{t}{t_c}}\right)$ as a function of $\frac{t}{t_c}$ for six different $\frac{A}{D_c}$ values are shown in Fig. 1.4. For all six $\frac{A}{D_c}$ values, the evolution term saturates at large times, and an approximate logarithmic increase of the evolution term vs. time is seen at middle times. For $A < D_c$, the evolution term levels-off (when the time axis is on a logarithmic scale) at small times. For $A = D_c$, the evolution term is approximately linear with log time at small times. We comment that the apparent leveling-off (which appears when the function is plotted on a logarithmic scale; there is no leveling off on a linear scale) at small times, the logarithmic increase at middle times, and saturation at large time is consistent with previous simulation results for chemical bond-induced ageing at the nanoscale [41] (also see Fig. 1.15).

However, since the velocity of the block is usually small during a hold (*i.e.*, $v \rightarrow 0$), the second term on the right side of Eq. (1.2) could be ignored, thus Eq. (1.2) becomes $\frac{d\theta}{dt} = 1$, resulting in $\theta(t) = t + B$, where B is a constant. Therefore, the evolution term in Eq. (1.1) becomes $b \ln \left(\frac{v_0}{D_c} (t + B)\right)$. Note that this form of the evolution term does not saturate at large t . When the contact time is longer than 1 s, B is usually chosen to be zero for simplicity [21, 38], and the evolution term becomes $b \ln \left(t \frac{v_0}{D_c}\right)$. However, when describing the apparent levelling-off of ageing (when the time axis is on a logarithmic scale) when the contact time is below about 1 s [21, 27, 38], the evolution effect term is often written as $b \ln \left(1 + \frac{t}{\tau}\right)$, where τ is the cut-off time and is around 1 s for many macroscale contacts. Note that $b \ln \left(\frac{v_0}{D_c} (t + B)\right) =$

$b \ln\left(1 + \frac{t}{B}\right) + b \ln\left(B \frac{v_0}{D_c}\right)$, so $\tau = B$. A plot of $\ln\left(1 + \frac{t}{\tau}\right)$ vs. t where $\tau = 1$ s is shown in Fig. 1.5, where the transition at around 1 s can be seen.

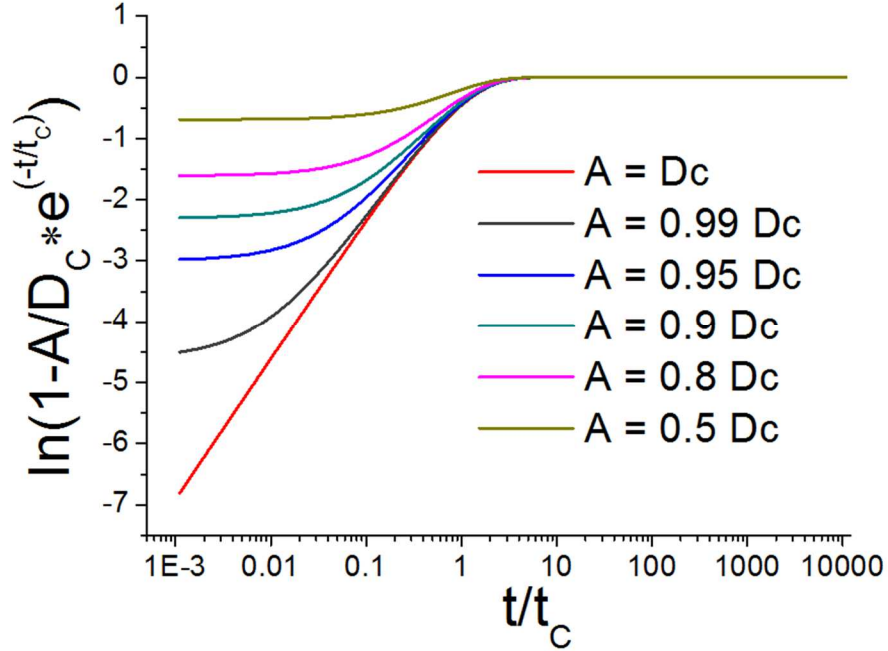


Fig. 1.4: The evolution term vs. time according to the solution to the slowness law (when $v > 0$). Here $t_c = \frac{D_c}{v}$. The solution is $\theta(t) = \frac{D_c}{v} \left(1 - \frac{A}{D_c} e^{-\frac{vt}{D_c}}\right)$, and $\ln\left(1 - \frac{A}{D_c} e^{-\frac{t}{t_c}}\right)$ is used to represent the evolution term. Six different $\frac{A}{D_c}$ values are used. Generally speaking, the evolution term increases almost logarithmically with time at middle times, and saturates at large times. Except for $A = D_c$, where the evolution term is almost linear with time at small times, the evolution term levels-off (for a logarithmic plot) at small times for all other $\frac{A}{D_c}$ values.

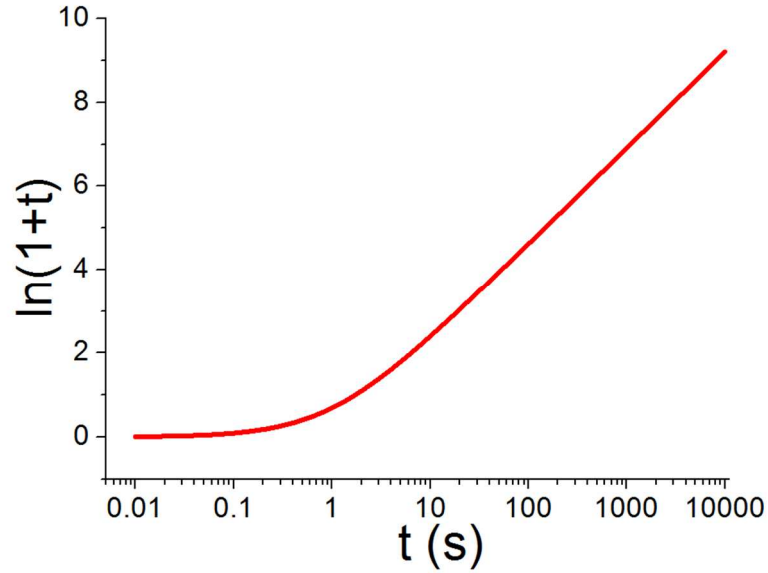


Fig. 1.5: The plot of $\ln(1 + \frac{t}{\tau})$ vs. t where $\tau = 1$ s. This function describes the evolution effect, *i.e.*, the third term in Eq. 1.1, as a function of time for small v . The transition between the logarithmic dependence at large times and the behavior at small times (which appears like a leveling-off on a logarithmic plot) is around the value of τ (1 s).

Another manifestation of the evolution effect is the logarithmic decrease of kinetic friction with sliding velocity, which is observed in many macroscale friction experiments [6, 21, 30, 42]. A typical result is shown in Fig. 1.6. In RSF laws, the concept of the memory distance D_c helps explain this velocity dependence of friction. The memory distance represents the distance the contact must slide to refresh itself. One conventional explanation for the logarithmic decrease of kinetic friction with velocity is as follows [21, 30, 43]: while sliding at a given constant velocity v , contacts at the interface have an average "effective contact time" equal to D_c/v , and according to the slowness law, ageing over this time contributes $b \ln(D_c/v)$ (*i.e.*, the evolution effect term in Eq. (1.1), which decreases with v ; here the slowness law is used to describe the state variable during smooth sliding) to the kinetic friction coefficient. The magnitude of D_c in

this scenario is equal to the average size of the asperities in contact on the frictional interface. In contrast, the direct effect term, $a \ln(v)$, increases with v . Therefore, the resultant kinetic friction f , which is proportional to the summation of the direct and evolution effect terms, satisfies $f \propto a \ln(v) + b \ln\left(\frac{D_c}{v}\right) \propto (a - b) \ln(v)$. If $a < b$, then $f \propto -\ln(v)$, which is termed velocity-weakening behavior in the geophysics literature, and which explains the logarithmic decrease of kinetic friction with sliding velocity. In this manner, the concept of the memory distance connects static friction (ageing behavior) and kinetic friction [43]. We point out that this conventional explanation of the memory distance and the logarithmic decrease of kinetic friction with velocity is phenomenological, and the physical meaning of the "effective contact time" remains vague.

The transition from decreasing friction to increasing friction with increasing velocity in Fig. 1.6 may be explained as follows: As velocity increases, contact lifetimes decrease, such that there is less time available for contact ageing, resulting in lower friction at higher sliding velocities. Above a critical velocity, there is insufficient time for contact ageing, such that the direct effect dominates, leading to the logarithmic increase of friction with velocity.

Another equation that is used to describe the evolution of θ is the slip law (sometimes called the Ruina law). It states

$$\frac{d\theta}{dt} = -\frac{v\theta}{D_c} \ln\left(\frac{v\theta}{D_c}\right) \dots\dots\dots(1.3)$$

Unlike the slowness law, there is no evolution of friction at zero velocity, *i.e.*, evolution of friction requires interfacial slip. To solve this differential equation for a VS test as shown in Fig. 1.1(b), we first write it as

$$\frac{d\theta}{\theta} = -\frac{v_2}{D_c} \ln\left(\frac{v_2\theta}{D_c}\right) dt. \text{ Since } \frac{d\theta}{\theta} = d(\ln(\theta)) = d\left(\ln\left(\frac{v_2\theta}{D_c}\right)\right), \text{ we get } d\left(\ln\left(\frac{v_2\theta}{D_c}\right)\right) = -\frac{v_2}{D_c} \ln\left(\frac{v_2\theta}{D_c}\right) dt. \text{ Thus}$$

$$\frac{d\left(\ln\left(\frac{v_2\theta}{D_c}\right)\right)}{\ln\left(\frac{v_2\theta}{D_c}\right)} = d\left(\ln\left(\ln\left(\frac{v_2\theta}{D_c}\right)\right)\right) = -\frac{v_2}{D_c} dt. \text{ If we choose the time when the velocity jumps as the starting time,}$$

then $\theta(t)$ could be solved straightforwardly, with the initial condition $\theta(t = 0) = \frac{D_c}{v_1}$, which is the state variable during steady sliding at velocity v_1 . The solution is $\theta(t) = \frac{D_c}{v_2} \left(\frac{v_2}{v_1}\right) e^{-\frac{v_2 t}{D_c}}$. According to this solution, when t is large enough, $\theta(t) \rightarrow \frac{D_c}{v_2}$, which is the state variable during steady sliding at velocity v_2 . Since the lateral displacement of the block $x = v_2 t$, in the regime in which friction is decaying $\mu(x) = \mu_0 + a \ln \frac{v_2}{v_0} + b \ln \left(\theta \frac{v_0}{D_c}\right) = \mu_0 + (a - b) \ln \frac{v_2}{v_0} + b \ln \frac{v_2}{v_1} e^{-\frac{x}{D_c}}$, which well fits the exponential decaying behavior in Fig. 1.1.

The slip law may also be applied to steady sliding. As discussed earlier, during steady sliding, $\theta = \frac{D_c}{v}$, where v is the sliding velocity. Substituting $\theta = \frac{D_c}{v}$ (which is a constant) into both sides of the slip law (Eq. (1.3)) results in $0 = 0$, which indicates that $\theta = \frac{D_c}{v}$ is a solution to Eq. (1.3).

We note that SHS tests are better described by slowness law than slip law, VS tests are better described by slip law than slowness law, and both slowness law and slip law could well apply to steady sliding [6, 19].

We comment that for steady sliding, when the sliding velocity of the block is v_0 , the state variable during sliding is $\theta = \frac{D_c}{v_0}$, as discussed above. Therefore, the argument of the logarithmic function of the evolution effect term $\theta \frac{v_0}{D_c} = 1$, which causes the evolution effect term in Eq. (1.1) to vanish. Also, since $\frac{v}{v_0} = 1$, the direct effect term also vanishes. Thus we get $\mu = \mu_0$. This shows how v_0 corresponds to μ_0 .

According this analysis, we can see that for steady sliding, both the direct and evolution effect terms in Eq. (1.1) do not fully represent the real contribution to friction from the direct and the evolution effects, respectively, because when the sliding velocity is v_0 , the real contribution from both the direct and the evolution effects should be non-zero. The functional forms (including the arguments of the logarithmic functions of) the direct and evolution effect terms in Eq. (1.1) contain constant offsets of the two effects.

A question that might arise to the reader is: why does the reference velocity v_0 , which is related to the direct effect, also appear in the evolution effect term? This is because the functional forms of the evolution and direct effect terms contain a constant offset, to make the functional forms of Eq. (1.1) concise (e.g., making μ_0 be a single term), and allows easy comparison with other laws like the slowness law (Eq. (1.2)) and the slip law (Eq. (1.3)) [6]. Otherwise, v_0 appearing in the evolution effect term has no real physical meaning.

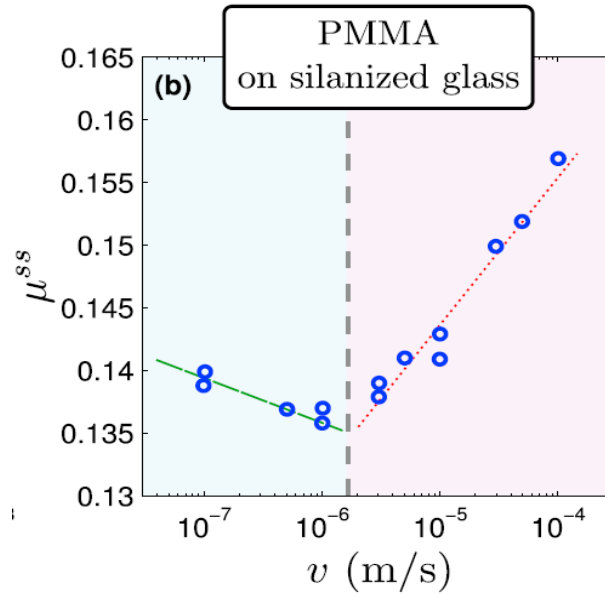


Fig. 1.6: Kinetic friction vs. sliding velocity for PMMA on silanized glass contacts. The kinetic friction first decreases then increases with velocity logarithmically. From Sinai *et al.* [42].

Another important manifestation of RSF laws is the stick-slip instability. In rock friction experiments, quasi-periodic stick-slips are often observed. Also, both the recurrence time and the peak-to-trough amplitude of stick-slip decrease with the loading point velocity. These phenomena are shown in Fig. 1.7.

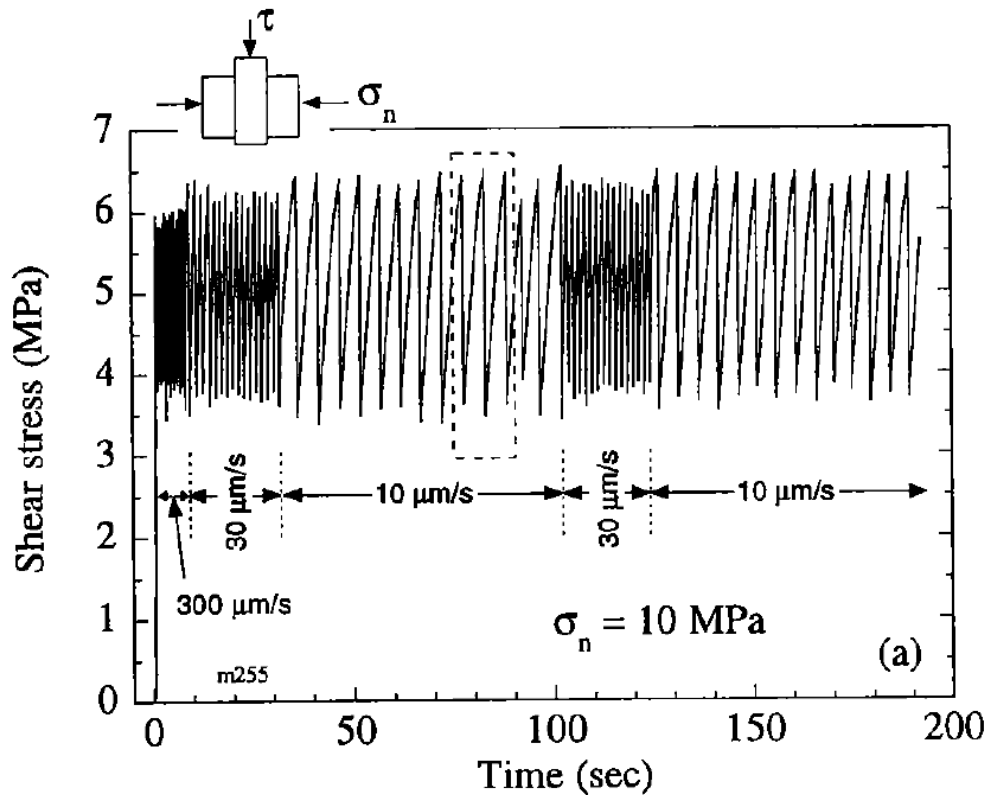


Fig. 1.7: Shear stress vs. time in a typical rock friction experiment. Data from friction experiments on quartz powders. Three different loading point velocities are used. The stick-slips are quasi-periodic, and both the amplitude and recurrence of stick-slip decrease with loading point velocity. From Karner and Marone [44].

Similar to ageing in SHS tests, the stick-slip amplitude also increases with recurrence interval (the counterpart to the hold time in SHS ageing tests) logarithmically, as shown in Fig. 1.8. Under a given load, the stress-drop data fall into different clusters corresponding to different loading point velocities. In each cluster, the stress drop increases logarithmically with recurrence interval; for all clusters, the stress drop also increases logarithmically with the recurrence interval, but with a different increasing rate.

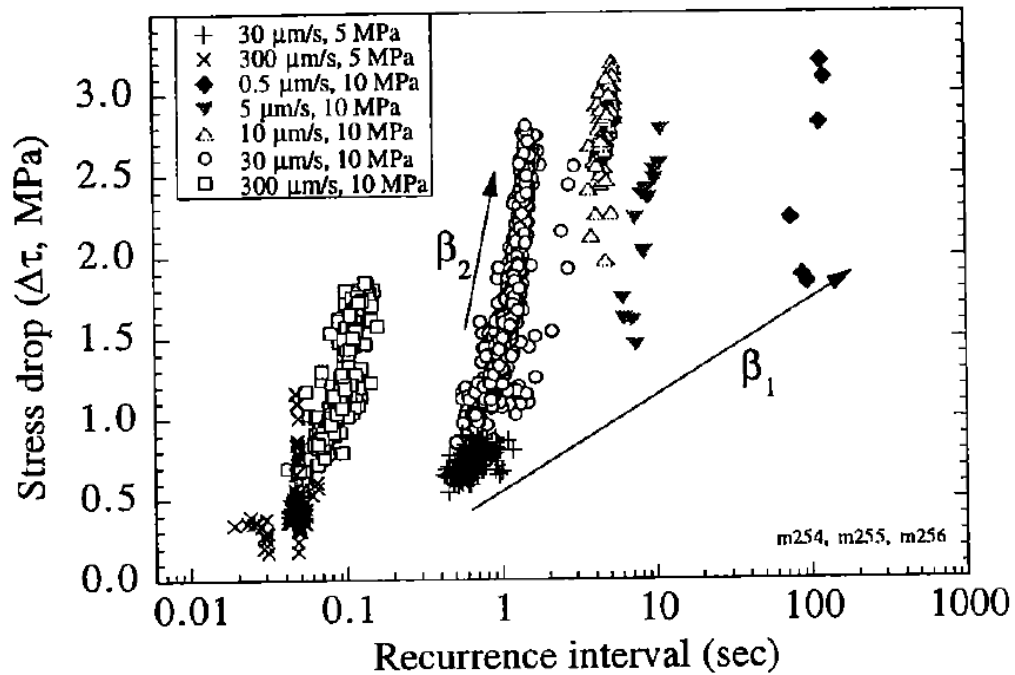


Fig. 1.8: Stress drop vs. recurrence interval of stick-slip for different loading point velocities. Data from experiments on quartz powders. It can be observed that, under a given normal pressure, the stress drop data fall into different clusters corresponding to different loading point velocities. In every cluster the stress drop increases logarithmically with recurrence interval; for all clusters the stress drop also increases logarithmically with the recurrence interval but with a different increasing rate. From Karner and Marone [44].

Though conventional RSF laws were originally established to describe frictional behavior of macroscale contacts, which may be composed of many asperities, recent progress shows that RSF laws can be used to describe data from microscale contacts which are composed of only a few asperities [45-47]. A non-geophysical example of where microscale contacts are relevant is microelectromechanical systems (MEMS).

1.2: Experimental studies of nanoscale interfacial chemical bond-induced ageing

To isolate and explore the physical mechanisms that underpin RSF laws, Li (from Prof. Carpick's group), Tullis, Goldsby and Carpick performed SHS experiments for single-asperity silica-silica nanocontacts using an atomic force microscope (AFM). A schematic of an AFM is shown in Fig. 1.9. The silica substrates were treated with piranha solution before the experiments, which leaves them hydrophilic due to substantial termination by hydroxyl groups. In these tests, which mimic macroscopic SHS tests on rock samples, the AFM tip, after sliding on the substrate, is held stationary for some time, and is then slid again. An amorphous silica tip and substrate were used because silicate minerals dominate the lithology of crustal rocks. Faults in the Earth are also often mineralized with silica due to flow of silica-rich fluids through faults (even when the fault-bounding rocks are not siliceous), and silicate rocks have similar frictional behavior to amorphous silica [48, 49]. Hold times were varied from 0.1 to 100 s, and a logarithmic increase of the friction drop ΔF , defined as the difference between the static friction force after holding, and the subsequent kinetic friction force, was observed across this entire range, as shown in Fig. 1.10. These data indicate that one part of the conventional RSF laws—the ageing law—can be well applied at the nanoscale.

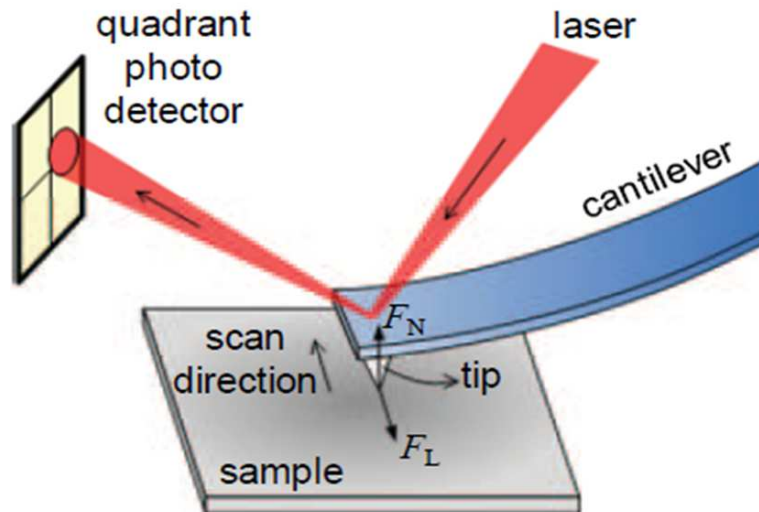


Fig. 1.9: Schematic of AFM. The base of the cantilever is controlled by a piezoelectric scanner. The laser beam is shone on the back of the cantilever and reflected to a four-quadrant photo detector. The lateral force on the tip twists the cantilever, which is read as the lateral signal on the photo detector. The normal force (*i.e.* the applied load) will cause normal bending of the cantilever which is read as the normal signal on the photo detector. From Li, Tullis, Goldsby and Carpick [49].

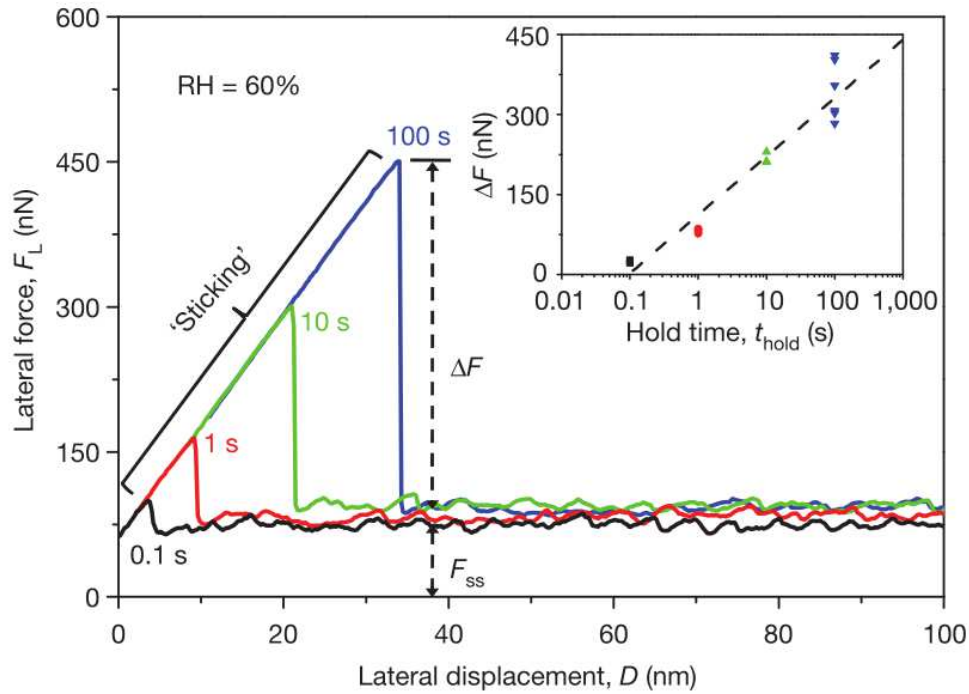


Fig. 1.10: Lateral force vs. lateral displacement (of the loading point) for four different hold times, ranging from 0.1 s to 100 s. The inset shows the logarithmic dependence of the friction drop on hold time. The hold time is varied randomly to exclude systematic errors. From Li, Tullis, Goldsby and Carpick [49].

Li, Tullis, Goldsby and Carpick also demonstrated that there is no plastic deformation in their AFM experiments. This was supported by two experiments. The first experiment is shown in Fig. 1.11 where a SHS test was first performed and the ageing (*i.e.*, the friction drop) was measured. The tip was then

lifted out of contact for 30 mins and the measured ageing was found to be much smaller than before. Then run-in scans were performed and the relatively high magnitude of ageing was recovered. If plastic deformation really occurs and the ageing is mainly caused by plastic deformation, then the ageing amplitude should not decrease after the tip is lifted out of contact for some time. The suppression of ageing after the tip is lifted implies that the ageing is probably due to interfacial chemical bond formation, which could be inhibited by contaminants adsorbed onto the tip from the environment while out of contact.

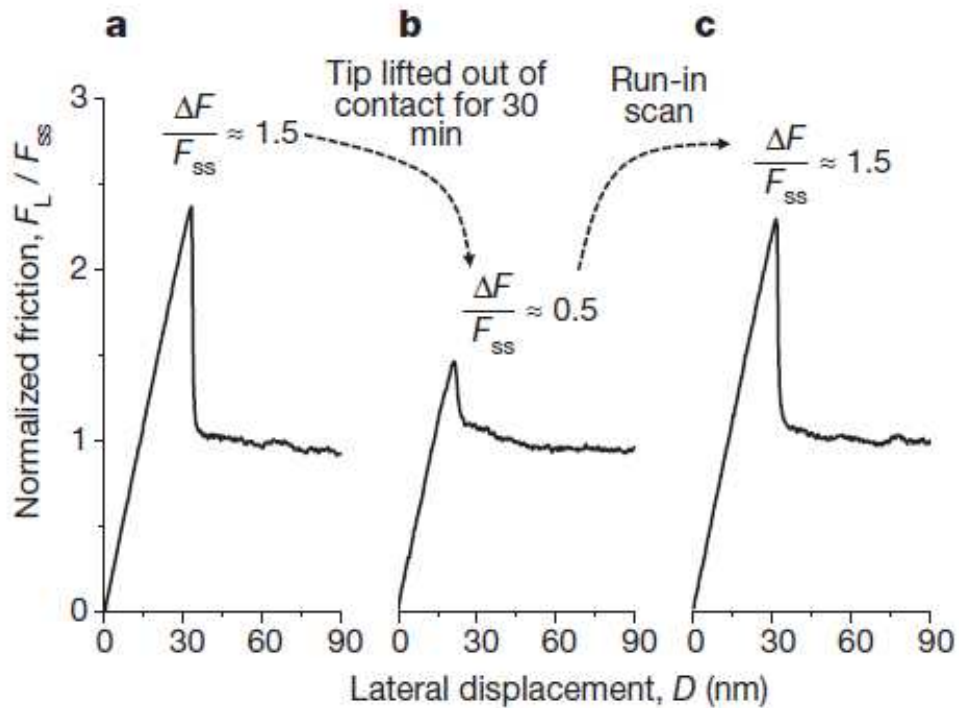


Fig. 1.11: Normalized friction vs. lateral displacement from three sequential SHS tests. Hold time = 100 s, RH = 40 %. Ageing is largely suppressed after the tip is lifted out of contact for a while. The magnitude of ageing recovers after run-in scans are performed. From Li, Tullis, Goldsby and Carpick [49].

The second experiment is shown in Fig. 1.12. Here SHS tests are performed to measure ageing of a silica-silica contact, a silica-diamond contact, and a silica-graphite contact. The results show that only the silica-silica contact exhibits significant ageing. Since the contact stresses are estimated to be 0.2 GPa, 1.5 GPa and 0.4 GPa respectively for the three cases, which are all much smaller than the indentation hardness

of amorphous silica (12 GPa), there should be no plastic deformation for the silica tip in all three tests. Also, since the diamond and graphite are both chemically inert with respect to silica, no interfacial chemical bonds are expected to form for the silica-diamond and silica-graphite contacts. Therefore, the results in this experiment imply that it is chemical bond formation and breaking, rather than plastic deformation, that dominates ageing.

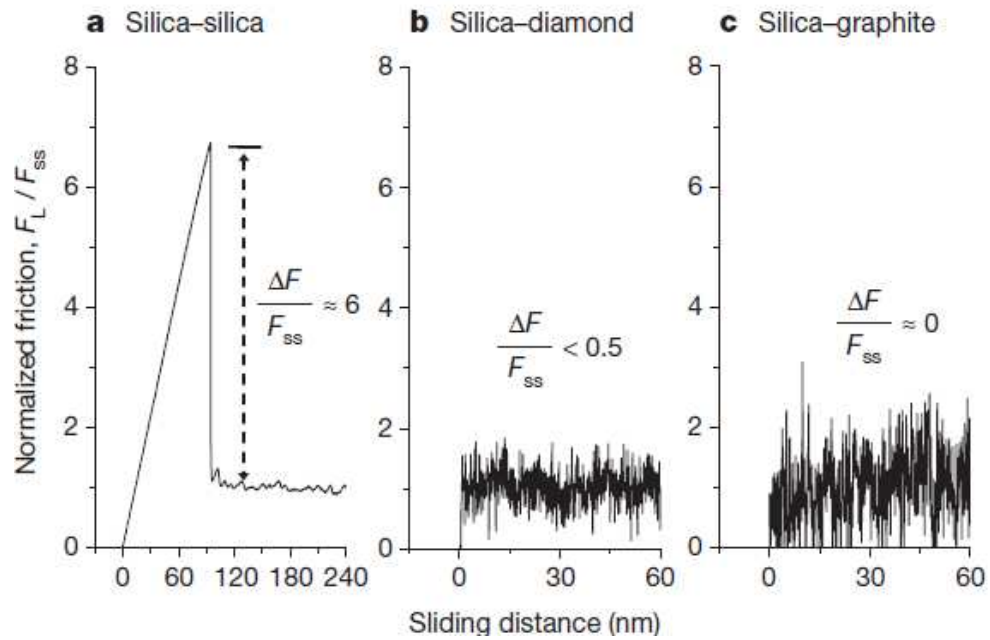


Fig. 1.12: SHS tests between silica tips and three different surfaces. Hold time = 100 s, RH = 60 %. Only the silica-silica contact exhibits significant ageing. From Li, Tullis, Goldsby and Carpick [49].

1.3: Theoretical studies of nanoscale interfacial chemical bond-induced ageing

Liu, Li, and Szlufarska's subsequent first-principles calculations showed covalent interfacial siloxane (Si-O-Si) bridges indeed form at silica-silica interfaces under similar conditions as in previous AFM experiments [41, 50].

Although covalent bonds can form between silica surfaces in multiple ways [51], these studies proposed interfacial siloxane bond formation. This assumes that the silica surfaces are highly hydroxylated and thus hydrophilic. Indeed, in the experiments, the samples were treated with piranha solution [49] and the experiments were conducted in a significant partial pressure of water which will quickly hydroxylate any dangling bonds. The tip surface is expected to have hydroxyl groups present as well after or while sliding [52]. For the simulations, the silica surfaces were deliberately hydroxylated. In this situation two silanol (Si-OH) groups from opposing surfaces react to form a siloxane bond through the following condensation reaction: $\text{Si-OH} + \text{Si-OH} \rightarrow \text{Si-O-Si} + \text{H}_2\text{O}$, the schematic of which is shown in Fig. 1.13.

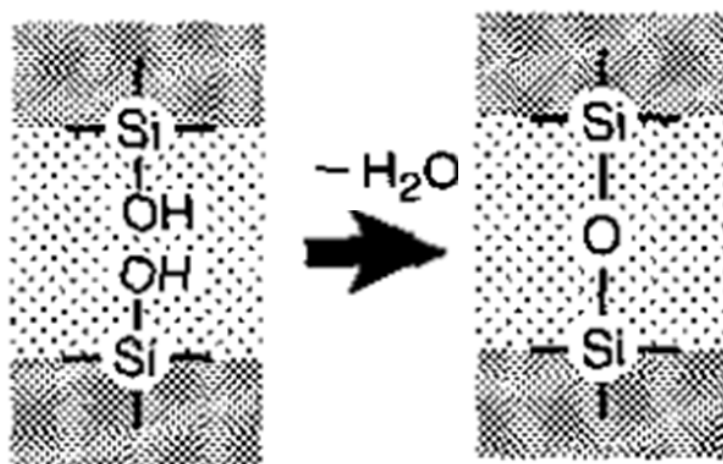


Fig. 1.13: Schematic of interfacial siloxane bond formation. From Vigil *et al.* [51].

Using molecular dynamics (MD) and density functional theory (DFT) simulations, Liu and Szlufarska also showed that there exists interaction energy between neighboring reaction sites. The interaction energy is defined for a given reaction site as the difference between the reaction energy barrier in the presence of siloxane bridge on a neighboring site and the reaction energy barrier in the absence of a siloxane bridge on a neighboring site. On average the interaction energy is positive. This is illustrated in Fig. 1.14. The positive interaction energy indicates that the formation of a siloxane bond at one site will inhibit the formation of siloxane bonds at neighboring sites. Liu and Szlufarska also found that this

interaction results from the change of elastic stress field near a reaction site after a siloxane bond forms, which increases the reaction energy barrier at neighboring sites.

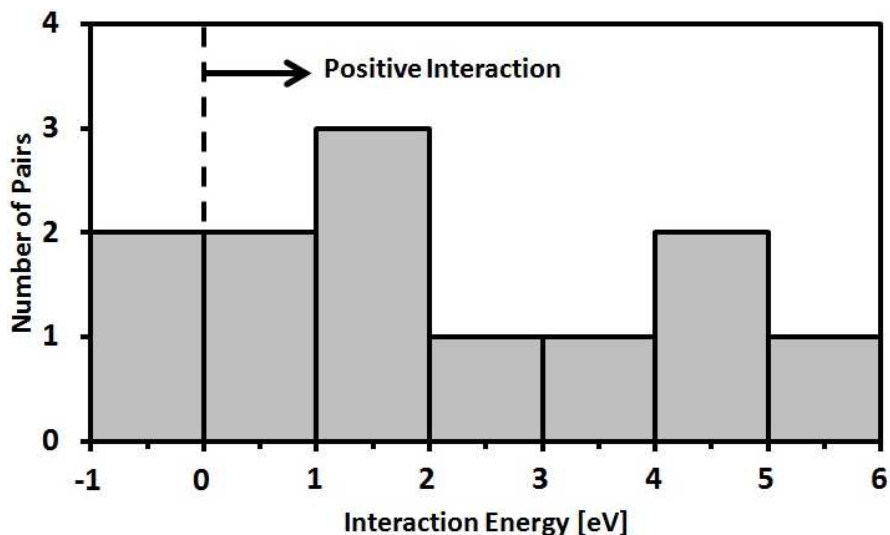


Fig. 1.14: Histogram of interaction energy in the simulation. From Liu and Szlufarska [41].

Using kinetic Monte Carlo (kMC) simulations, Liu and Szlufarska also showed that the number of bonds, and thus the static friction force, varied with time in a nearly logarithmic fashion over a time scale comparable to the experiments, namely ~ 0.1 - 100 s [41, 50]. This occurred for different initial reaction energy barrier distributions when interactions between neighboring sites are included in the simulations. The results are shown in Fig. 1.15. In the simulation three different initial barrier distributions are used: pressure-induced (*i.e.*, due to the distribution of pressure on the surfaces), geometry-induced (*i.e.*, due to the distribution of distances between neighboring silanol groups on opposite surfaces), and from MD simulations.

Since this interaction inhibits the formation of siloxane bonds, it results in slowing down the ageing process. As seen in Fig. 1.15 (d, e, f), for all three initial barrier distributions it was observed that the interactions extend the logarithmic regime of static friction vs. time from 0.1 to 100 s. This time span is consistent with the results of AFM experiments [49]. Therefore, it supports the hypothesis that there are inhibiting interactions between neighboring reaction sites in the experiments.

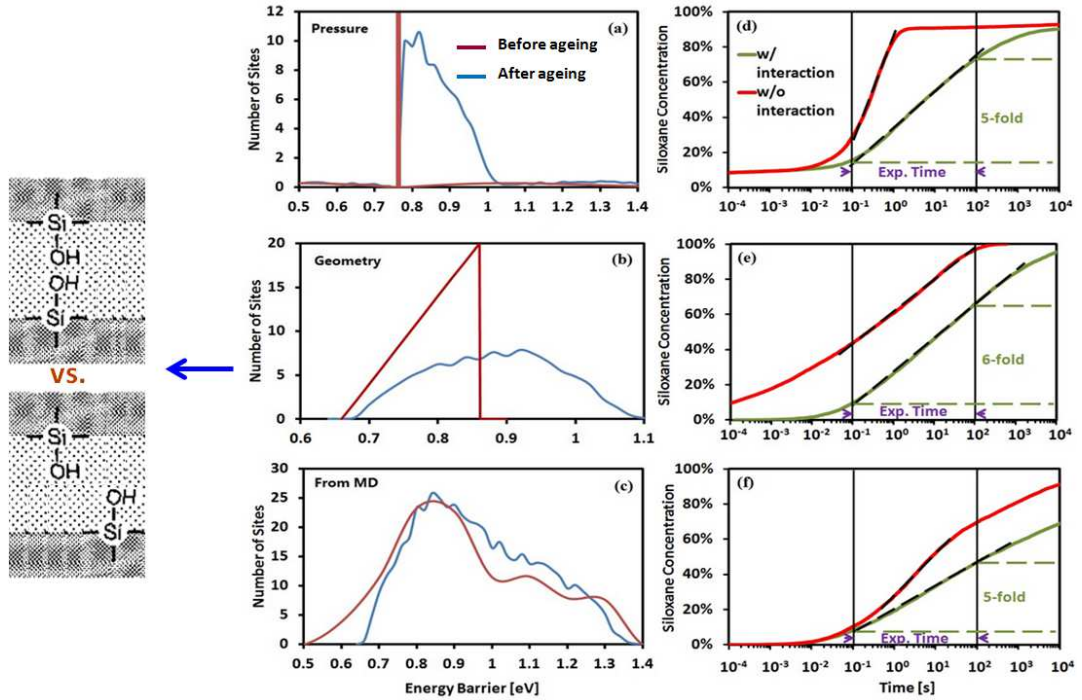


Fig. 1.15: Siloxane concentration vs. time for different initial barrier distribution. (a) - (c) show three different initial barrier distributions (blue curves): pressure-induced (*i.e.*, due to the distribution of pressure on the surfaces), geometry-induced (*i.e.*, due to the distribution of distances between neighboring silanol groups on opposing surfaces), and from MD simulations. The dark red curves are the distributions before ageing. (d), (e) and (f) correspond to (a), (b) and (c) respectively. The green curves are with interactions, while the bright red curves are without interactions. With interactions, all three initial barrier distributions result in logarithmic ageing with time from 0.1 s to 100 s, which is consistent with AFM experiments. From Liu and Szlufarska [41].

These results (AFM experiments and simulations) provide the first asperity-level understandings of interfacial chemical bond-induced (ICBI) friction for silica-silica interfaces at the nanoscale.

1.4: Motivations and overall review of the work in this project

In chemical kinetics involving mechanical forces, the load and stress dependence of the chemical reaction rate is a very important issue, and chemical bond formation is the mechanism of ageing in our case. Also, load dependence of rock friction is an important issue in geophysics. We are thus motivated to study the load and time dependence of ageing in our experiments.

The previous work on nanoscale ICBI friction (including experiments [49], simulations and analytical work [41]) made significant progress towards understanding single-asperity RSF behavior. However, those studies only focused on ageing (*i.e.*, the evolution effect). The direct effect and the combination of the direct and evolution effects, which are also important aspects of RSF laws, have not been investigated deeply at the nanoscale. In this thesis, I will elucidate these effects by studying the dependence of kinetic friction on sliding velocity, and establishing physically-based RSF relations and insights into the underlying physical mechanisms for single-asperity contacts.

In addition, questions concerning whether there is a memory distance at the nanoscale, as there is at the macroscale, and whether and why stick-slip instabilities occur for nanoscale contacts exhibiting ICBI friction, will be addressed in this thesis.

Current modeling of earthquakes is reasonably good at predicting where an earthquake will (eventually) occur, but not when. This may in part be because of the lack of physics in the models. This work will establish a physically-based RSF law and uncover new aspects of RSF behavior for nanoscale contacts. In doing so, it may contribute to developing future macroscopic relations for RSF behavior, such as for geological materials, which could be used predictively in the studies of earthquakes.

1.5: List of papers and manuscripts in this project

Here is the list of papers and manuscripts I produced in this project, which have been published, are currently under review, or in preparation.

- *Load and time dependence of interfacial chemical bond-Induced friction at the nanoscale*, **Kaiwen Tian**, Nitya N. Gosvami, David L. Goldsby, Yun Liu, Izabela Szlufarska, and Robert W. Carpick, **Phys. Rev. Lett.**118, 076103 (2017) [1].
- *Memory distance for interfacial chemical bond-induced friction at the nanoscale*, **Kaiwen Tian**, Nitya N. Gosvami, David L. Goldsby, and Robert W. Carpick, in review.
- *Rate and state friction laws for nanoscale contacts: The Prandtl-Tomlinson model with temperature and evolution effect*, **Kaiwen Tian**, David L. Goldsby, and Robert W. Carpick, in review.
- *Stick-Slip Instabilities for Interfacial Chemical Bond-Induced Friction at the Nanoscale*, **Kaiwen Tian**, Nitya N. Gosvami, David L. Goldsby, and Robert W. Carpick, in review.
- *Non-logarithmic ageing behavior at small timescales in nanoscale contacts*, Kaiwen Tian, Yun Liu, Nitya N. Gosvami, David L. Goldsby, Izabela Szlufarska, and Robert W. Carpick, in preparation.

Chapter 2: Experimental Methods and Sample Preparation

Since this project is multidisciplinary in nature, multiple instruments and methods are involved for relevant nanotribological testing and characterization. The main instruments used include AFM, transmission electron microscope (TEM), and furnaces to oxidize AFM tips and substrates. AFM force calibrations details are also provided in this chapter.

2.1: Preparation of tips and substrates, and experimental setups

The silicon probes (CSC37 Mikromasch and PPP-FM-50 Nanosensor) and Si(100) substrates used in our experiments were oxidized in a box furnace in ambient air by heating them to 1100 °C for 1 hour. The heater was then switched off and the furnace was allowed to cool to room temperature (taking about 15 hours) while the probes remained in the furnace. This procedure produces an oxide layer thickness of approximately 200 nm. The RMS roughness of the oxidized substrate's surface, measured using AFM, was 0.17 nm for a $0.5 \mu\text{m} \times 0.5 \mu\text{m}$ area.

Si(100) substrates were cut from single crystal wafers (Entegris) using a diamond scribe and then cleaned with isopropyl alcohol (IPA) in a sonicator. The static water contact angle of the substrate was measured using a home-built contact angle measurement instrument in the laboratory of Prof. Russell J. Composto (3 microliters of Milli-Q water was used for each measurement; the snapshot was taken in less than 30 seconds once the droplet was placed; images were analyzed using Image J; under the help from Prathima Nalam) to be $53^\circ \pm 1^\circ$ at this point. The substrates were then cleaned using piranha solution (the volume ratio of the concentrated sulfuric acid and the 30 % hydrogen peroxide solution is 3:1) at 100 °C for 10 mins. The water contact angle was measured to be $16^\circ \pm 1^\circ$ after piranha treatment, indicating a strongly hydrophilic surface which is consistent with the silica surface containing a high density of hydroxyl groups [53, 54].

An RHK UHV350 AFM system was used for all friction measurements, which were conducted under controlled relative humidity at 1 atm. in nitrogen gas. Humidity was controlled by purging a mixture of dry nitrogen gas (highly pure, dry nitrogen vapor from a liquid nitrogen dewar) and nitrogen gas from the same source, but bubbled through a container filled with deionized water. Mixing these two streams at different flow rates allowed the humidity to be varied.

We comment that we have never observed ageing or other evidence of the evolution effect for IPA-cleaned silica substrates (*i.e.*, no piranha treatment), which contain far fewer silanol groups on the surfaces. This is well-established in literature [53] and is demonstrated by such surfaces having a larger contact angle with water (measured to be $53^\circ \pm 1^\circ$ in our case). This further supports our interfacial siloxane bond mechanism for ageing at the nanoscale, as previously established by Li *et al.* [49].

2.2: Characterizing the atomic force microscope tips used for the experiments

Fig. 2.1 shows a TEM (made by JEOL 2010F; acceleration voltage: 200 kV; magnification: $\times 10000$; courtesy of Zac Milne.) image of a typical AFM tip used for probing nanoscale friction before any imaging is performed. The magnification chosen in the TEM measurement was not too large ($\times 10000$) so that the electron beam intensity is small enough to avoid significant beam damage. Also, the shape of the tip was found to not change within the resolution of the TEM (approximately 100 nm) after taking several images, indicating that there was little beam damage. For this specific example, the tip radius is measured to be approximately 130 nm. This was extracted using custom-written Matlab image-analysis codes (courtesy of Joel Lefever; the code could be found on the group server at V:_DataExchange\Kaiwen Tian PUBLIC\matlab_AFM tip profile in TEM).

In addition to the TEM imaging we performed for one tip shown in Fig. 2.1, we also scanned most tips on an ultrananocrystalline diamond (UNCD) substrate and used the blind tip reconstruction method [55]

to measure the tip shape and size before any experiments, and monitored changes of the tip shape and size for some of the tips.

Topographic scan images of one typical tip on a UNCD substrate is shown in Fig. 2.2 (a) and (b). Between the two measurements in (a) and (b), the tip was scanned on a piranha-cleaned silica substrate for about 6.8 mm sliding distance, and the conditions are: $T = 24\text{ }^{\circ}\text{C}$, $\text{RH} < 1\%$, applied loads used smaller than 187 nN and adhesion = 434 nN. The time interval between (a) and (b) is approximately 2 hours. The images are analyzed in the SPIP 6.0.4 software. Global leveling is performed for plane correction, then the image is filtered to remove high frequency noise with a low pass filter (a lower cutoff wavelength of 1 nm is used). In the following tip characterization window, the setting “Ignore Lower Values” is chosen to be 33%, the iterations chosen to be 3, and the detection counts is chosen to correspond to an abrupt change in height profile. We use the tip radius in the fast scan direction as the tip radius to report since it is more accurate than the tip radius in slow scan direction (since there is more drift in slow scan direction). The tip radius measured in this way in Fig. 2.2(a) and (b) are $105 \pm 15\text{ nm}$ and $166 \pm 14\text{ nm}$ respectively. Fig. 2.2 (c) and (d) show the cross-sectional profiles in the fast scan direction of the tip as determined by the SPIP software, corresponding to Fig. 2.2 (a) and (b) respectively. It can be seen from Fig 2.2 (d) that while the tip radius is larger after sliding for 6.8 mm, it can still be well fit by a parabola.

This analysis shows that in this case the tip radius increases by 58% after sliding 6.8 mm on the sample. Since the sliding distance in one set of tests in this project is at most about $120\text{ }\mu\text{m}$, we could estimate that the tip radius change in one typical set of tests is generally smaller than 1%. Therefore, in this project, we assume that the tip radius can be treated as constant during each set of tests (this is consistent with the reasonably smooth trends in most of our experimental results). Since the radius of the tips we used frequently fell in the range of $100\text{ nm} \sim 150\text{ nm}$, for the data analysis in this thesis, we assume that the tip radius is 125 nm. Future studies should instead avoid such a strong assumption, and instead should involve frequently measuring the tip radius and shape after each set of measurements.

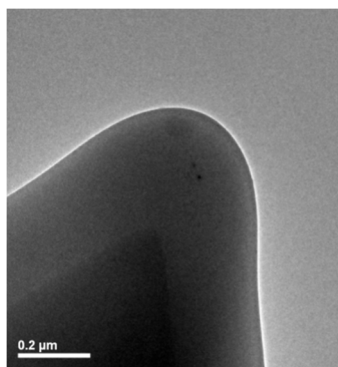


Fig. 2.1: TEM image of a typical AFM tip used before experiments. The tip radius is about 130 nm. We do not have TEM images of tips after each experiment in this thesis.

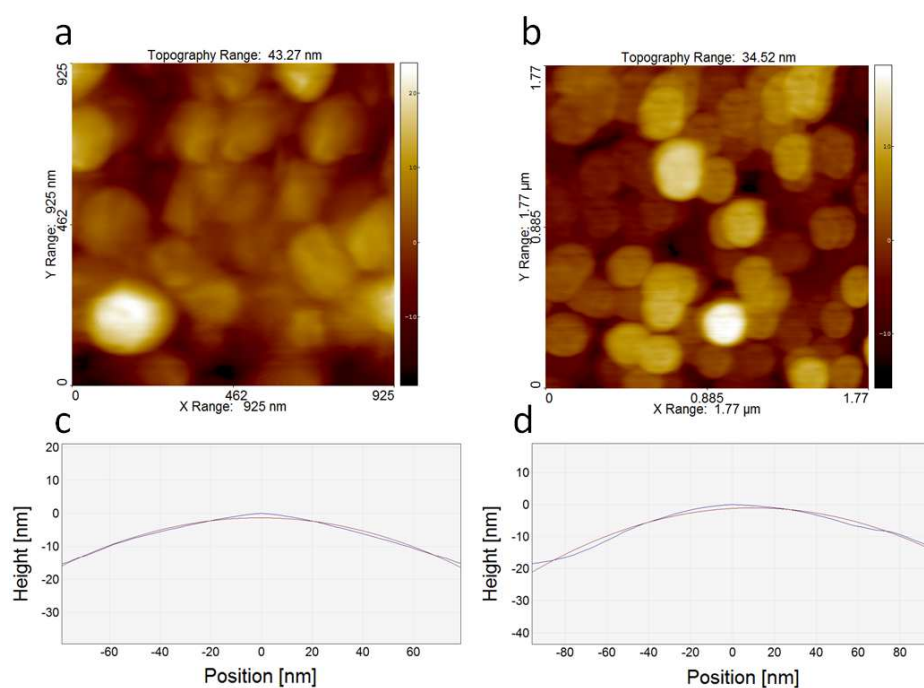


Fig. 2.2: The topographic scan images (a) and (b) of a typical tip on a UNCD substrate and the tip profiles (c) and (d). The tip was scanning on a piranha-cleaned silica substrate for approximately 6.8 mm between the measurement in (a) and the measurement in (b). Plots (c) and (d) are cross-sectional profiles of

the tip in fast scan direction as determined by the SPIP software, corresponding to (a) and (b) respectively. The blue curves are the tip profile and the red curves are parabolic fit. The tip radius is measured to be 105 ± 15 nm and 166 ± 14 nm respectively in (a)/(c) and (b)/(d). It could be seen from (d) that after sliding for 6.8 mm, the tip surface is still not flat, and could be fitted by a parabola well.

2.3: Calibration procedure

The goal of calibration in this work is to obtain calibration factors which convert voltage signals (measured on the photo diode) to forces in both normal and lateral direction.

First, normal cantilever spring constants were calibrated using Sader's method [56]:

$$k_N = 0.191\rho w^2 L Q \Gamma_i(f_0) f_0^2 \dots\dots\dots(2.1)$$

where ρ is the density of air, w is the cantilever width, L is cantilever length, Γ_i is the imaginary part of the hydrodynamic function, f_0 is the fundamental resonant frequency of the cantilever in normal direction, and Q is the quality factor. f_0 and Q are measured by obtaining the thermal noise spectrum of the normal deflection of cantilever and analyzing the fundamental resonance peak.

According to Euler beam theory [57, 58], $k_N = \frac{E w m^3}{4L^3}$, where E is Young's modulus and m is the thickness of the cantilever, and the torsional stiffness of the cantilever $k_t = \frac{G w m^3}{3L}$, where G is the shear modulus. Since $G = \frac{E}{2(1+\nu)}$, where ν is the Poisson's ratio, we have

$$k_t = k_N \frac{2L^2}{3(1+\nu)} \dots\dots\dots(2.2)$$

by which the torsional stiffness can be calculated from normal stiffness.

We then could calculate the lateral stiffness of the cantilever k_L :

$$k_L = \frac{k_t}{h^2} \dots \dots \dots (2.3)$$

where h is the height of the tip.

The values of L and w are measured using an interferometer (Zygo), and the value of h is from the vendor. Young's modulus E and Poisson ratio ν of silica was taken to be 68.0 GPa and 0.19 respectively [59].

Then the normal and lateral calibration factors (which convert the photodiode signals from voltage units to force units) was obtained according to the equations in [60]:

$$S_N = \frac{k_N}{o}, S_L = \frac{3}{2} \frac{k_L h}{o L} \dots \dots \dots (2.4)$$

where o is the normal optical lever sensitivity (unit: V/nm), which is the slope of the force-distance curve in contact. This method assumes that the normal and lateral photodiode sensitivities (the sensitivities of the change of normal and lateral signals on the photodiode due to the change of the angles of normal bending and twisting of the cantilever respectively) are the same. This assumption is found to be reasonable by determining that the calibration factors calculated in this way is found to be within 15 % of those determined using the diamagnetic lateral force calibration method [61, 62]; courtesy of Xin-Zhou Liu.

Chapter 3: Load and Time Dependence of Interfacial Chemical Bond-Induced Ageing at the Nanoscale

Interfacial chemical bonding dominates the ageing behavior of nanoscale silica-silica contacts [41, 49]. The role of normal load (and thus, normal stress) on ageing is predicted to be significant (as in mechanochemistry) [50], but has not been examined experimentally. Also, how load affects the frictional behavior of rock materials is an important issue in geophysics, since stresses can vary widely on faults in the earth's crust [63-65].

Previous measurements of ageing with time at the nanoscale were performed under only one given load. A natural extension of that previous work is therefore to further vary the load to study how the dependence of ageing on time changes with load. Here, we show using AFM that for nanoscale ICBI friction of silica-silica interfaces, the magnitude of ageing increases approximately linearly with the product of the normal load and the log of the hold time for a given loading point velocity (comparing data for a given velocity ensures that the magnitude of the direct effect is constant in each set of tests, as shown in Chapter 4). We attribute this behavior to the approximately linear dependence of contact area on load in the positive load regime before significant wear occurs, as inferred from sliding friction measurements. This implies that the average pressure, and thus the average bond formation rate, is load-independent within the accessible load range in our AFM. We also consider a more accurate nonlinear model for the dependence of contact area on load, from which we extract the activation volume and the average stress-free energy barrier to the ageing process. Our work further demonstrates the existence of the friction evolution effect for nanoscale silica-silica contacts, and illustrates the role of load in the process.

3.1: Experimental results for the load and time dependence of ageing

Si AFM tips and Si(001) wafers were thermally oxidized, and the wafers hydroxylated using piranha solution prior to experiments. Experiments were conducted under controlled relative humidity at 1 atm in nitrogen gas.

Slide hold slide (SHS) tests were performed in an RHK AFM with environmental control. The friction drop ΔF , equal to the difference between the peak friction and the subsequent sliding friction, was measured and plotted vs. $\log t_{\text{hold}}$ (where t_{hold} is the hold time in the SHS tests). We applied normal loads ranging from the lowest load at which stable measurements could be conducted to the highest load that could be attained in our instrument. From the same data, ΔF vs. normal load for each of the hold times t_{hold} was plotted (Fig. 3.1). The approximately linear relation between ΔF and $\log t_{\text{hold}}$ exists for loads from 20 to 400 nN (Fig. 3.1(a)), with a slope that increases approximately linearly with load (Fig. 3.1(b)) (small deviations from linearity are observed at the shortest hold time of 0.1 s, in agreement with Liu and Szlufarska [41]; experimental results clearly showing this deviation are shown, for example, in Fig. 5.3 in Chapter 5). Correspondingly, for each value of t_{hold} , ΔF increases approximately linearly with load (Fig. 3.1(c)), with a slope that increases approximately linearly with $\log t_{\text{hold}}$ (Fig. 3.1(d)). For simplicity, henceforth we replace t_{hold} with t . The slopes from Figs. 3.1(b) and 3.1(d) are comparable; their values are 0.530 and 0.425, respectively. We demonstrate in Section 3.2 that the linear relationship in Figs. 3.1(b) and 3.1(d) and the slopes of the linear fits in those two figures being comparable are both expected results, due to the simultaneous linearity of the friction drop vs. load (Fig. 3.1(a)) and friction vs $\log t$ (Fig. 3.1(c)).

In Fig. 3.1, the hold times t_{hold} are large enough and the sticking times small enough (due to sufficiently large loading point velocity) that t_{hold} is approximately equal to the effective contact time (the sum of the hold time and the sticking time), *i.e.*, the sticking time is typically negligible with respect to t_{hold} . As an example, when t_{hold} is about 100 s, the sticking time is around 0.2 s.

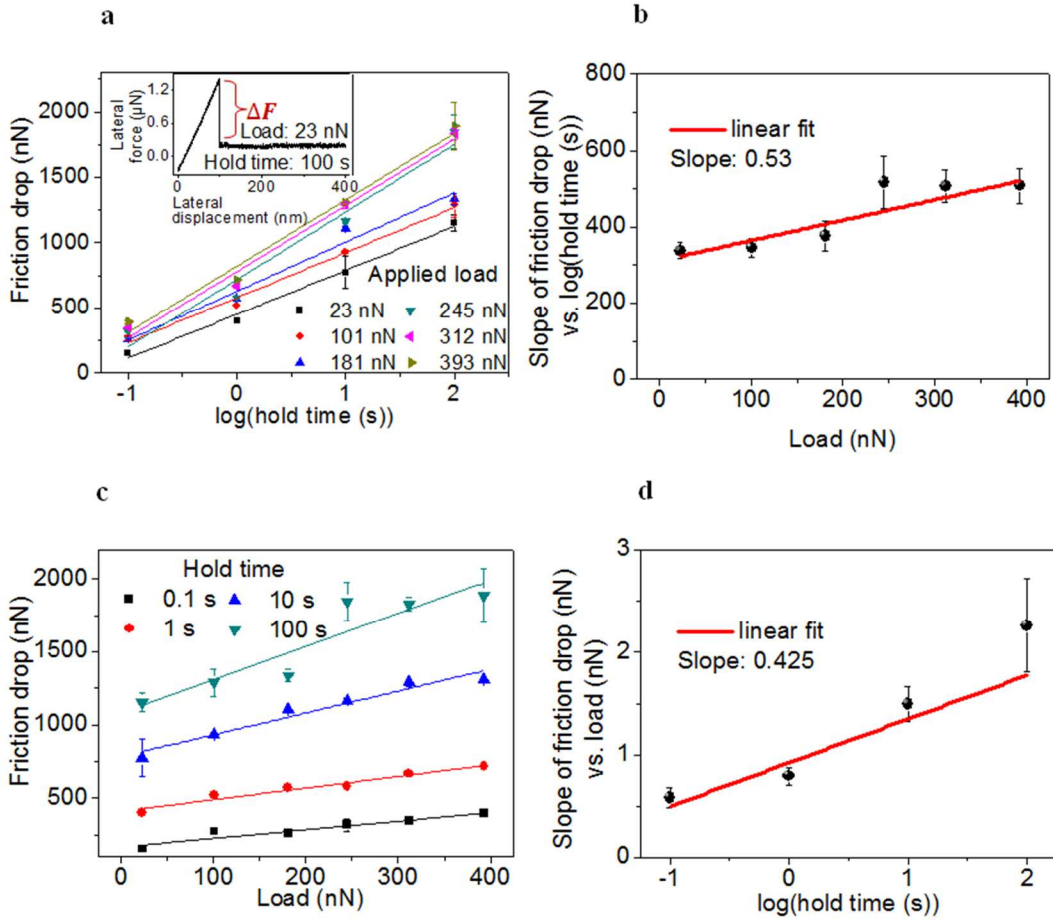


Fig. 3.1: Effect of hold time and applied normal load on static ageing. Relative humidity (RH) = 53%, temperature $T = 24$ °C and loading point velocity is 500 nm/s. **(a)** Friction drop vs. log of hold time for different normal loads. The inset shows the lateral force vs. lateral displacement curve from the test for a 100-s hold time and 23 nN applied load, and indicates how we measure friction drop. The linearity of the friction drop vs. log of hold time is seen for all normal loads. **(b)** The slope of each linear fit in **(a)** vs. load. The slope varies linearly with load. **(c)** Friction drop vs. load for different hold times. For a given hold time, friction drop increases linearly with load. **(d)** The slope of the linear fits from **c** vs. log of hold time. The slope increases linearly with the log of hold time. Loads and hold times are varied randomly to exclude systematic errors. Reproduced from Tian *et al.* [1].

3.2: Derivation of the load and time dependence of ageing

Here we demonstrate that the simultaneous linearity of the data in Figs. 3.1(a) and (c) necessarily also predicts that the trends shown in Figs. 3.1(b) and (d) will also be linear. The linearity in Figs. 3.1(a) and 3.1(c) implies that the functional dependence of ΔF on $\log(t)$ and on load L should be

$$\Delta F(L, \log(t)) = h \cdot (L + k) \cdot (\log(t) + m) + q \dots\dots\dots (3.1)$$

Here we describe how Eq. (3.1) is derived. In Fig. 3.1, the linearity of ΔF vs. $\log(t)$ and ΔF vs. L indicates that:

$$\Delta F(L, \log(t)) = f_1(L) \cdot \log(t) + f_2(L) = f_3(\log(t)) \cdot L + f_4(\log(t)) \dots (3.2)$$

where $f_1(L)$ and $f_2(L)$ are both functions of L , and $f_1(L)$ is the slope of friction drop vs. $\log(t)$ under a given load L ; $f_3(\log(t))$ and $f_4(\log(t))$ are both functions of $\log(t)$, and $f_3(\log(t))$ is the slope of friction drop vs. L under a given hold time t .

Taking the partial derivative first with respect to L , and then with respect to $\log(t)$ on both sides of the right equation, we obtain:

$$\frac{df_1(L)}{dL} = \frac{df_3(\log(t))}{d(\log(t))}$$

In the above equation, L and t are independent variables, so both sides of this equation must be equal to a constant. We set

$$\frac{df_1(L)}{dL} = \frac{df_3(\log(t))}{d(\log(t))} = a \dots\dots\dots (3.3)$$

where a is a constant.

The above analysis demonstrates that the linearity in Fig. 3.1 (b) (*i.e.*, $f_1(L) \propto L$) and in Fig. 3.1 (d) (*i.e.*, $f_3(\log(t)) \propto \log(t)$), and the fact that the slopes of the linear fits in Fig. 3.1 (b) and Fig. 3.1 (d) are the same, result from the linearity in Fig. 3.1 (a) and Fig. 3.1 (c).

Now we will derive the relationship that describes the dependence of ΔF on $\log(t)$ and on load L , where L and t are independent variables. Based on Eq. (3.3), we have

$$f_1(L) = aL + b \quad \text{and} \quad f_3(\log(t)) = a \cdot \log(t) + c$$

where b and c are both constants.

Substituting the above expressions into Eq. (3.2) produces

$$b \cdot \log(t) - f_4(\log(t)) = c \cdot L - f_2(L)$$

Again, since L and t are independent variables, both sides of the above equation must be equal to a constant. Therefore, we set $b \cdot \log(t) - f_4(\log(t)) = c \cdot L - f_2(L) = d$, where d is a constant.

We can then write

$$f_4(\log(t)) = b \cdot \log(t) - d \quad \text{and} \quad f_2(L) = c \cdot L - d.$$

Finally, we arrive at the following expression for ΔF

$$\Delta F(L, \log(t)) = (aL + b) \cdot \log(t) + f_2(L) = a \cdot L \cdot \log(t) + b \cdot \log(t) + c \cdot L - d \quad ..(3.4)$$

Note that Eq. (3.4) could be equivalently written as Eq. (3.1):

$$\Delta F(L, \log(t)) = h \cdot (L + k) \cdot (\log(t) + m) + q$$

where h, k, m, q are all constants, and the sets of constants a, b, c, d and h, k, m, q can be simply related by the following equations: $a = h, b = hk, c = hm, d = -hkm - q$. Thus we derive Eq. (3.1) from the linearity in Fig. 3.1 (a) and (c).

3.3: Building models for the load and time dependence of ageing

3.3.1: The nonlinear model

The rate of siloxane bond formation at a nanoscale contact can be modeled using Arrhenius kinetics. According to the supplementary material of [41], the distribution of the number of reaction sites follows the relationship:

$$\frac{dP(E_b, t)}{dt} = \frac{A(E_b, t)}{\tau_0} e^{-\frac{E_b}{k_B T}} \dots\dots\dots(3.5)$$

where $P(E_b, t)$ is the distribution density of the number of reaction sites with reaction energy barrier E_b where siloxane bonds have formed at time t , k_B is Boltzmann's constant, T is the temperature, $A(E_b, t)$ is the distribution density of the total number of available reaction sites with reaction energy barrier E_b at the time t , and τ_0 is the time constant for siloxane bond formation.

To develop the physical basis underlying the empirical relationship in Eq. (3.1), we start by assuming that the reaction energy barriers for the ageing process are uniformly distributed over the range $[0, G]$, where 0 corresponds to a barrierless reaction and G is the uppermost energy barrier. We also assume that there are no interactions between neighboring sites, as done in other related studies [41, 50]. The limitations of these assumptions are discussed further below. This allows us to derive an analytical formula that describes the reaction kinetics of siloxane bond formation (derivations can be found in section S5 of [41]), based on Eq. (3.5):

$$P(t) = \frac{N}{G} \cdot k_B T (2.3 \log(t) - 2.3 \log(\tau_0) + 0.58) \dots\dots\dots(3.6)$$

where $P(t)$ is the number of reaction sites where siloxane bonds have formed, and N is the number of available reaction sites at the beginning.

Liu and Szlufarska considered $P(t)$ to be proportional to the static friction force, consistent with previous experiments [66] and supported by simulations [50, 67]. We further assume that the maximum force that can be sustained by each interfacial bond is equal to the breaking force of a siloxane bond f_0 . Thus, $\Delta F = f_0 \cdot P(t)$. According to [68], $f_0 \approx 1.5 \text{ nN}$.

We also assume that $N = \rho S$, where ρ is the number density of initial available reaction sites and S is the contact area. To apply Eq. (3.6) to the experimental data (Fig. 3.1), we need to establish a relationship between contact area S and load L , and determine how the uppermost energy barrier G depends on L .

According to the Derjaguin-Müller-Toporov (DMT) model (the validity of using the DMT model will be discussed in Section 3.8), the contact area $S = \pi \left(\frac{3R(L+L_0)}{4E_C} \right)^{\frac{2}{3}}$, where the effective Young's modulus $E_C = (2 \frac{1-\nu^2}{E})^{-1}$, and E and ν are, respectively, the Young's modulus and Poisson's ratio of silica, and L_0 is the pull-off force (due to adhesion) before ageing begins. The average pressure $\sigma = \frac{L+L_0}{S} = \frac{1}{\pi} \left(\frac{4E_C}{3R} \right)^{\frac{2}{3}} (L+L_0)^{\frac{1}{3}}$. Following stress-activated kinetics from transition state theory, we take the uppermost energy barrier when stress is applied to be $G = G_0 - \sigma V_0$ [69-71], where G_0 is the uppermost energy barrier when the contact is stress-free, and V_0 is the activation volume. Thus, Eq. (3.6) becomes:

$$\Delta F = f_0 k_B T \rho \pi \left(\frac{3R}{4E_C} \right)^{\frac{2}{3}} \frac{(L+L_0)^{\frac{2}{3}}}{G_0 - \frac{V_0}{\pi} \left(\frac{4E_C}{3R} \right)^{\frac{2}{3}} (L+L_0)^{\frac{1}{3}}} (2.3 \log(t) - 2.3 \log(\tau_0) + 0.58) \dots (3.7)$$

3.3.2: The first stage of the linear approximation

To obtain a simpler expression and extract the desired parameters, we apply two different linear approximations. For the first stage of linearization, we assume that the effect of stress on the uppermost activation barrier G is small, which is consistent with the small activation volume determined below. Assuming G is constant, Eq. (3.7) becomes

$$\Delta F = \frac{f_0 k_B T \rho \pi}{G} \left(\frac{3R}{4E_c} \right)^{\frac{2}{3}} (L+L_0)^{2/3} \cdot (2.3 \log(t) - 2.3 \log(\tau_0) + 0.58) \dots\dots\dots (3.8)$$

We now extract the values of L_0 and τ_0 using the experimental results in Fig. 3.1 and our model (Eq. (3.8)). Our method of extracting L_0 is shown in Fig. 3.2 (a) and (b). The idea is that the friction drop is assumed to depend on load according to Eq. (3.8), whose only normal force dependence comes through the term $(L+L_0)^{\frac{2}{3}}$. Thus, if correct, then normalizing all the friction drop data points in Fig. 3.1 (a) by dividing each value by $(L+L_0)^{\frac{2}{3}}$ should, in theory, yield a single master curve assuming the correct value of L_0 is used. In practice, noise, error, and inaccuracy in the model will produce deviations from such a master curve. We thus vary L_0 and find the value that gives the smallest deviation (Fig. 3.2(b)). To determine a meaningful deviation, for a given L_0 and hold time, we first calculate the mean value and standard deviation of $\Delta F / (L+L_0)^{\frac{2}{3}}$ for the data from all six applied loads L . We then divide the standard deviation by the mean value to obtain the relative standard deviation. We then calculate the average value of this relative standard deviation over all four hold times and plot this average relative standard deviation vs. L_0 . Fig. 3.2(a) shows that this curve has a global minimum. The $L_0 = 253$ nN corresponding to this minimum is the adhesion force, which we want to extract.

Similarly, our method of extracting τ_0 is shown in Fig. 3.2 (c) and (d). Similar to the procedure for determining L_0 , we divide all data points in Fig. 3.1 (c) by the common factor in Eq. (3.8) that depends on t , *i.e.* $[2.3 \log(t) - 2.3 \log(\tau_0) + 0.58]$. We then tune τ_0 to make all the data points converge with minimal deviation into one master curve, in the same manner as for L_0 . This curve has a global minimum (Fig. 3.2(c)), resulting in $\tau_0 = 0.033$ s.

Using the DMT model, the value of $L_0 = 253$ nN corresponds to the adhesion force of the contact before ageing occurs. Using the tip radius $R = 130$ nm, the work of adhesion can be estimated as 0.306 N/m, which is reasonable for a partially hydroxylated silica-silica interface [51, 72]. L_0 could not be directly measured from typical force-distance (FD) tests because under typical loading speeds (about 100 nm/s), the

tip and substrate will be in contact for approximately 1 s. During this contact time, ageing occurs, and adhesion will be larger than L_0 . Furthermore, we were unable to pull the tip off the substrate in FD tests due to the finite normal displacement range of our AFM, which limited us to a maximum tensile force of approximately 300 nN. Thus, we can conclude that ageing of ~ 1 s or more yields a pull-off force larger than $L_0 = 253$ nN.

Our model was derived under the assumption that τ_0 corresponds to a typical atomic vibration period ($\sim 10^{-13}$ s; $\log(10^{-13}) = -13$). However, our results indicate that $\tau_0 = 0.033$ s ($\log(0.033) = -1.5$). The value of τ_0 is orders of magnitude larger than expected. Some of this discrepancy may derive from the fact that τ_0 is in the logarithmic function, which hugely magnifies the relatively smaller error in $\log(\tau_0)$ (which is directly extracted from experimental data) to a much larger error in τ_0 . An additional cause of this discrepancy is the limitation of our model, which will be discussed further in Section 3.4.

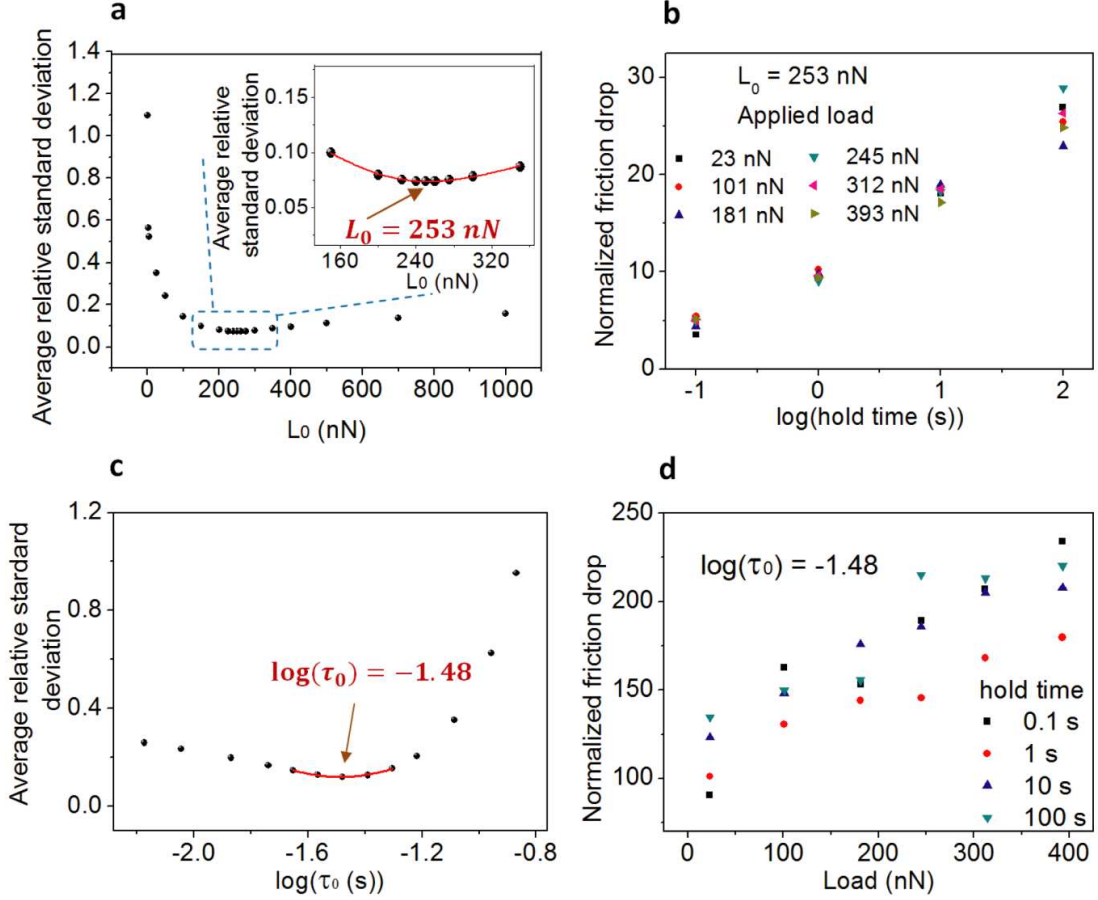


Fig. 3.2: Extracting L_0 and τ_0 from Fig. 3.1. To obtain L_0 , all the data points in Fig. 3.1 (a) are divided (normalized) by $(L+L_0)^{\frac{2}{3}}$, and then L_0 is varied so that all the data points converge as closely as possible into one master curve. To do this, for a given L_0 and hold time, we calculate the mean value and standard deviation of $\Delta F/(L+L_0)^{\frac{2}{3}}$ for the data from all six applied loads L . We then divide the standard deviation by the mean value to obtain the relative standard deviation. Finally, we calculate the average value of this relative standard deviation over all four hold times. (a) shows the dependence of this average relative standard deviation on L_0 , with the global minimum point $L_0 = 253 (\pm 4)$ nN, which is the extracted value of L_0 . (b) shows the normalized friction drop vs. \log of hold time when $L_0 = 253$ nN. For τ_0 , similar to the procedure for determining L_0 , we divide all the data points in Fig. 3.1 (c) by $[2.3\log(t) - 2.3\log(\tau_0) + 0.58]$. We then tune τ_0 to make all the data points converge with minimal deviation onto one master curve

in the same manner as for L_0 . (c) shows the dependence of the average relative standard deviation on τ_0 , with the global minimum point seen to be $\tau_0 = 0.033 (\pm 0.001)$ s, *i.e.*, $\log(\tau_0) = -1.48 (\pm 0.03)$, which is the extracted value of τ_0 . (d) shows the normalized friction drop vs. load when $\tau_0 = 0.033$ s. From Tian *et al.* [1].

Having established values of L_0 and τ_0 , we then use Eq. (3.7) to fit the data in Fig. 3.1(c) to obtain values of G_0 and V_0 . We already have $f_0 = 1.5$ nN [68], $k_B T = 4.1 \times 10^{-21}$ J, $R = 130$ nm, $E_c = 35.3$ GPa, $\rho = 4/\text{nm}^2$ [41], $\tau_0 = 0.033$ s, and $L_0 = 253$ nN. For a given value of hold time t , ΔF is thus a function of L , with only two unknown parameters, G_0 and V_0 . We fit the friction drop vs. load data for different hold times in Fig. 3.1(c) using Eq. (3.7). For $t = 0.1$ s, we obtain $G_0 = (0.75 \pm 0.11)$ eV, $V_0 = (52 \pm 12)$ Å³, both of which are physically reasonable values for a chemical bonding mechanism [41, 69]. For comparison, Liu and Szlufarska found from density functional theory (DFT) simulation that the typical energy barrier values for siloxane bridging range between 0.5 eV and 1.4 eV [41]. The fitting for all four hold times are shown in Fig. 3.3.

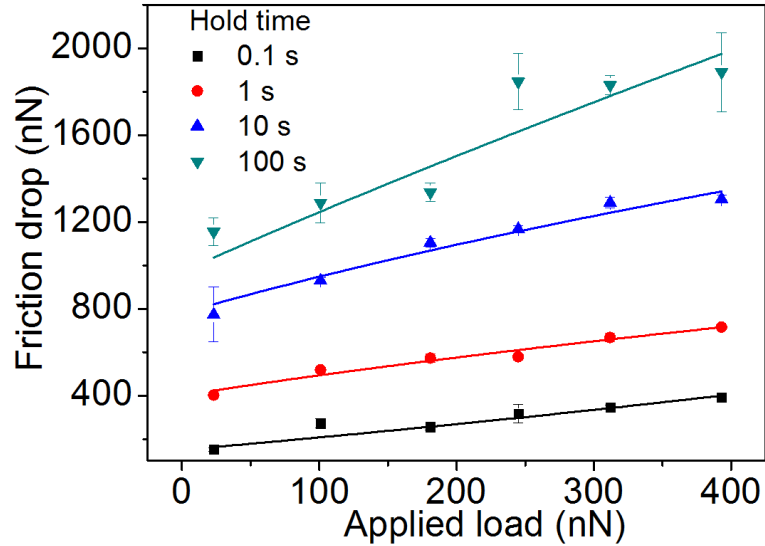


Fig. 3.3: Fitting of friction drop vs. load data for all 4 hold times – Fitting the data with Eq. (3.7) for a 0.1 s hold time yields values of $G_0 = (0.75 \pm 0.11)$ eV and $V_0 = (52 \pm 12)$ Å³; for 1 s hold time, $G_0 = (0.32 \pm 0.05)$ eV, $V_0 = (-8.5 \pm 5.4)$ Å³; for 10 s hold time, $G_0 = (0.23 \pm 0.05)$ eV, $V_0 = (-11.9 \pm 5.4)$ Å³; for 100 s hold time, $G_0 = (0.41 \pm 0.14)$ eV, $V_0 = (11 \pm 15)$ Å³. From Tian *et al.* [1].

The values of G_0 extracted from the data for all four hold times are all reasonable. For example, in previous simulation work [41], the reaction energy barrier ranges from 0.5 eV to 1.4 eV. Considering the assumptions in our model and experimental error, and also for simplicity, we consider the range of reasonable values of G_0 to be 0.1 eV to 10 eV. However, for a hold time of 100 s, the error in the activation volume is larger than the activation volume itself, a consequence of the significant fluctuations of the friction drop data for the 100 s hold time. Also, the activation volume extracted from the data representing hold times of 1 s and 10 s are negative. Though it seems counterintuitive, a negative activation volume has been reported before [73], which for molecular reactions can imply a volume reduction from the reactant to the transition state; as a consequence, the energy barrier to the reaction goes *up* as stress is applied. At this stage, we just treat these negative values as the result of the uncertainty in fitting our data. This is because the co-dependency of the two fitting parameters V_0 and G_0 in our fitting is high, which indicates that the fitting function is overparameterized. This is likely due to the limited number of data points in our time-consuming experiments (which require precise alignment, drift minimization, and surface preparation). This also arises from the fact that the nonlinearity in the variation of the contact area over the studied load range is relatively small.

To examine the uncertainty in V_0 , we tuned its value for hold times of 0.1 s, 1 s, and 10 s. With each fixed V_0 , we fit Eq. (3.7) using the software Origin, and obtain a value of G_0 and the R-squared value (coefficient of determination) of the fit. We calculate the uncertainty in V_0 by finding the range of values where R-squared is larger than 0.9. These values are 15~86 Å³ (*i.e.*, 51 ± 36 Å³),

$-36 \sim 25 \text{ \AA}^3$ (*i. e.*, $-5.5 \pm 31 \text{ \AA}^3$), and $-30 \sim 5 \text{ \AA}^3$ (*i. e.*, $-13 \pm 18 \text{ \AA}^3$) for 0.1 s, 1 s, and 10 s hold times, respectively. In all cases, the extracted G_0 values are reasonable. It can be seen that for 1 s and 10 s, the range of V_0 covers both negative and positive regimes. Therefore, we can only conclude that, in the framework of the analytical result of reference [41]:

- For the 0.1 s hold time, V_0 has a modest magnitude of $(78 \pm 28) \text{ \AA}^3$ which corresponds to $(0.49 \pm 0.18) \text{ eV/GPa}$. Thus, it requires $(2.04 \pm 0.75) \text{ eV/GPa}$ of normal pressure to reduce the highest energy barrier by 1 eV.
- For all other hold times, the magnitude of V_0 is small enough, and the uncertainty in V_0 is large enough that we cannot definitively claim it is non-zero. In other words, there may be no pressure dependence of the energy barriers, or at best, the dependence is weak.

We then used Origin 8.0 to perform nonlinear surface fitting (two independent variables: applied load and hold time) for all friction drop vs. load and hold time data simultaneously using Eq. (3.7). The initial values of the parameters for the fitting routine are chosen to be the ones obtained above (for G_0 , the mean value of G_0 from all four hold times is used, which is 0.43 eV; for V_0 , the value for the 0.1 s hold time is used since it is the only reasonable one, which is 52 \AA^3). The extracted four parameters are listed below.

$$G_0 = (0.40 \pm 0.03) \text{ eV}, V_0 = (55.0 \pm 0.8) \text{ \AA}^3, L_0 = (191 \pm 48) \text{ nN}, \tau_0 = (1.92 \pm 0.29) \text{ s}$$

The values of G_0 , V_0 and L_0 extracted in this manner are close to the values extracted previously when fitting to each hold time separately. However, τ_0 is significantly larger than the 0.033 s extracted previously. This is likely due to the fact that τ_0 is in the argument of a logarithmic function (so that a change in τ_0 by several orders of magnitude corresponds to a much smaller change in $\log(\tau_0)$). Thus, a small amount of error or fluctuations in the friction drop data could lead to large errors in τ_0 .

Since there are interactions between neighbouring reaction sites during ageing, the energy barrier and activation volumes may change at those sites [41]. Thus, different hold times, and thus different degrees of ageing and interactions, would actually correspond to different G_0 and V_0 . Therefore, the fitting approach first used, whereby we extract G_0 and V_0 for each hold time, may be more accurate than extracting one value of G_0 and one value of V_0 from the global data set. A further source of uncertainty is that, as specified above, this analysis assumes a uniform distribution of energy barriers, which may not be true in experiments. Obtaining a denser set of data at more hold times and loads would help to determine more accurate values of G_0 and V_0 , and might allow an assessment of their variation with hold time and with a non-uniform energy barrier distribution.

We also comment that in the procedure of extracting parameters above (G_0, V_0, L_0, τ_0), when we obtained the errors of those parameters, we did not take into account the errors in tip radius R (due to wear, which may change the tip shape also; more details are in Chapter 2), the density of surface silanol groups ρ , and the strength of single siloxane bond f_0 . Taking those errors into account when extracting parameters could be one direction of future studies.

3.3.3: The second stage of the linear approximation

For the second stage of linearization, we perform a Taylor expansion of Eq. (3.8) around $L = 0$. This is equivalent to assuming that the contact area varies linearly with load L . Such an approximation of kinetic friction (and thus contact area) vs. load has been found to be reasonably accurate in several nanoscale friction studies [74, 75]. This gives:

$$\Delta F = \frac{f_0 k_B T \rho \pi}{G} \left(\frac{3R}{4E_C} \right)^{\frac{2}{3}} L_0^{-1/3} \left(\frac{2}{3} L + L_0 \right) \cdot (2.3 \log(t) - 2.3 \log(\tau_0) + 0.58) \dots (3.9)$$

Comparing Eq. (3.8) and Eq. (3.9), the relative error of this linear approximation at $L = 393 \text{ nN}$ is $\left[L_0^{-1/3} \left(\frac{2}{3}L + L_0 \right) - (L+L_0)^{\frac{2}{3}} \right] / (L+L_0)^{\frac{2}{3}} \approx 9.1 \%$, which is small. Therefore, our linear approximation is a reasonable approach initially.

Note that Eq. (3.9) is a special case of Eq. (3.1), with $q = 0$. Therefore, we obtain an equation that explains the experimental finding of an approximately linear dependence of friction drop on load times log of hold time in Fig. 3.1.

Note that we do not directly use Eq. (3.9) to extract L_0 and τ_0 in order to reduce error, since Eq. (3.8) maintains the nonlinear expression of load according to DMT model and thus is more accurate than Eq. (3.9).

To show that this linear approximation is reasonably accurate, we measured the kinetic friction vs. load in the positive load regime using another oxidized Si tip on piranha-cleaned silica (Fig. 3.4), revealing a nearly linear dependence of kinetic friction on load, with an offset along the load axis due to adhesion. The velocity was large enough to avoid any significant evolution effect. Additional details on the decrease of the magnitude of the evolution effect with loading point velocity in smooth sliding tests will be presented in Chapter 5. For a non-ageing single-asperity contact, kinetic friction is often observed to be proportional to the contact area S [76], including for silicon and silica contacts [77, 78]. This, and our results in Fig. 3.4, demonstrate that the linear approximation of the load dependence of S on L is reasonable.

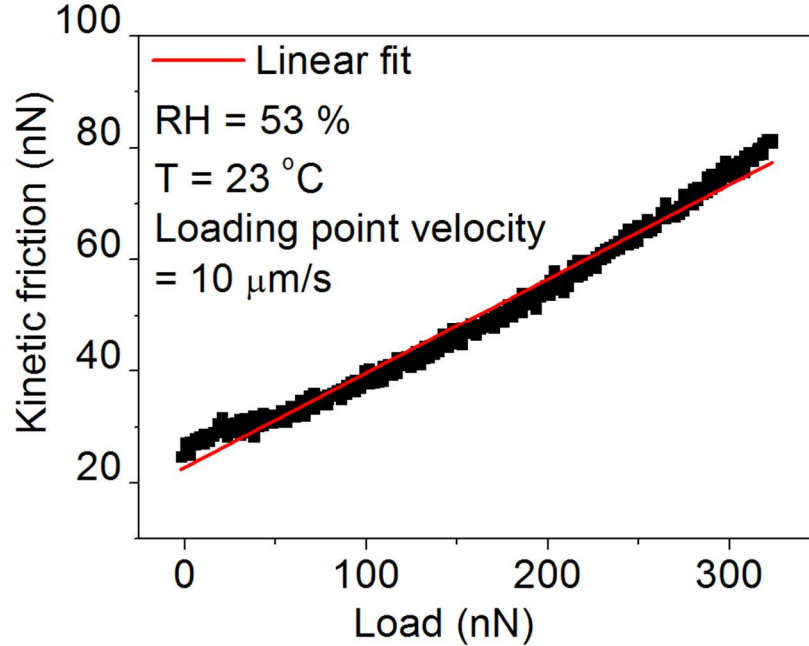


Fig. 3.4: Kinetic friction vs. normal load. The silica substrate was cleaned with piranha solution before experiment. The load is systematically varied from 0 to 325 nN. From Tian *et al.* [1].

The physical picture represented by the linearized Eq. (3.9), which describes the load and time dependence of ageing, can be understood as follows: the load dependence, $(\frac{2}{3}L + L_0)$, approximately determines the number of initial available reaction sites, which is proportional to the contact area, setting the stage for the ensuing ageing process; the time dependence, $(2.3\log(t) - 2.3\log(\tau_0) + 0.58)$, describes how the interfacial chemical bonds per unit contact area form with time. Increasing the load increases the contact area, which creates a larger number of sites for ageing to occur (*i.e.*, where siloxane bonds can form), while on average, it does not affect the formation kinetics of individual chemical bonds.

Although the area-load dependence is explicitly nonlinear in the DMT model and this is also likely the case in our actual experiment, the nonlinearity resulting from Eq. (3.7) is rather small over the load regime we can access. This indicates that the potentially complex effects of load on both contact area and

the energy barrier (*i.e.*, the term N/G in Eq. (3.6)) actually vary nearly linearly with load. In other words, while the number of available reaction sites and the energy barrier distribution have different dependences on load (and the energy barrier distribution varies with hold time), they combine in a way that leads to an approximately linear variation with load, independent of the hold time. While simple, our approaches (Eqs. (3.8) and (3.9) for the linear approximation, and Eq. (3.7) for the more accurate nonlinear version) provide a first approximate method to analyze the load dependence of friction for an ageing contact. From the analysis, we extract the energy barrier and the activation volume (*i.e.*, the stress sensitivity of the energy barrier) for the nanoscale silica-silica ageing process.

3.4: Discussion regarding the value of τ_0

In Section 3.3.2, we discussed how τ_0 was many orders of magnitude greater than the value assumed by theory, which was the period of a typical atomic vibration. In order to explain why the experimentally-determined value of τ_0 is so large, we incorporate the dependence of the breaking force for a single bond on the energy barrier for bond formation [50] into the derivation of the logarithmic dependence of the total number of bonds formed with time in [41], as explained in the following text.

According to Ref. [50], the maximum pulling force (f_0) one siloxane bond can withstand is proportional to the bond formation reaction energy barrier:

$$f_0(E_b) = \alpha(E_b + \beta)$$

Here α is a different parameter than the α in Ref. [50]. $\alpha < 0$, and β is also a parameter.

Incorporating this relationship into the derivation of the logarithmic dependence of the total number of bonds formed on time in Ref. [41], and with similar derivation procedures used in Ref. [41], we can finally obtain (here, we use the same symbols as those used in [41]):

$$\Delta F = A\alpha kT \left\{ \beta \ln(t) - \beta \ln(\tau_0) + 0.58\beta + \frac{1}{2}kT[\ln(t)]^2 + \frac{1}{2}kT[\ln(\tau_0)]^2 + \frac{1.98}{2}kT - kT \ln(t) \cdot \ln(\tau_0) - 0.58 kT \ln(\tau_0) + 0.58kT \ln(t) \right\}$$

The linear dependence of ΔF on $\ln(t)$ observed in AFM experiments implies that the second order term $\frac{1}{2}kT[\ln(t)]^2$ is negligible. This approximation is reasonable only if $kT \ll \beta$. Note that since $\tau_0 \approx 10^{-13}$ s, t varies from 0.1 s to 100 s, thus $\ln(t)$ varies from -2.3 to 4.6, $kT \approx 4.1 \times 10^{-21}$ J. Therefore, if $kT \ll \beta$, then all the terms containing kT in the above expression of ΔF are negligible. So $\Delta F \approx A\alpha kT[\beta \ln(t) - \beta \ln(\tau_0) + 0.58\beta] = A\alpha kT\beta[2.3\log(t) - 2.3\log(\tau_0) + 0.58]$. Since now the time-dependent term $[\ln(t) - \ln(\tau_0) + 0.58]$ is the same as that in Eq. (3.8) in the main text, where the breaking forces of all the bonds are assumed to be the same, the τ_0 extracted (using the same procedure as described in Section 3.3.2) would be the same as the one in Section 3.3.2. Therefore, the above formalism, wherein we consider the dependence of bond breaking force on the bond formation energy barrier, does not explain the large value of τ_0 extracted from the experimental data, as presented in the main text.

One possible reason for this failure is that the derivation of the logarithmic dependence of ΔF (in order to be analytically tractable) assumed that the initial reaction energy barrier distribution is uniform and there is no interaction between neighboring sites. These assumptions may be so strict that applying the derived logarithmic dependence to our experimental results could cause large errors when extracting certain parameters. Applying more realistic energy barriers precludes us from solving the problem analytically and requires numerical models such as the one introduced in Ref. [41]. The results from and discussions of our collaborators' numerical simulations, which assume more realistic energy barrier distributions, are presented below.

As demonstrated by Liu and Szlufarska [41], both the initial distribution of energy barriers and the interaction between reaction sites influence the reaction kinetics of siloxane bond formation. It was further shown by Li *et. al.* [50] that the strength of the interfacial siloxane bonds also decreases with the increasing density of interfacial bonds. Here, our collaborators Y. Liu and I. Szlufarska calculate the kinetics of ageing

using kinetic Monte Carlo (kMC) simulations with both effects taken into consideration. The three types of initial energy barrier distributions they consider are the same as the ones considered in [41]. Interactions between neighboring reaction sites now account for both the increase of reaction energy barrier and decrease of siloxane bond strength after formation of a neighboring siloxane bond. The magnitude of the static friction force induced by each newly formed siloxane bridge decreases linearly with the number of siloxane bonds already formed at surrounding sites. The minimum value of the contribution of a bond to the static friction force is set to be equal to half the maximum strength of the bond, which in turn corresponds to the case when the bond is fully surrounded by other interfacial siloxane bridges. They tested the effect of the above choice and found that a faster decay of the strength of a siloxane bond will decrease the maximum strength of the interface, but it will not change the general trend of the reaction kinetics (such as the logarithmic increase of ageing amplitude with time). As mentioned before, τ_0 is selected to be 10^{-13} s for these kMC simulations.

A summary of the results from kMC simulations is shown in Fig. 3.5, where panels a1, b1, and c1 show the initial distributions of reaction energy barriers and panels a2, b2, and c2 show the corresponding amount of ageing as a function of time. One can see that the presence of interactions between neighboring siloxane bridges leads to a longer period of time during which static friction increases logarithmically with time. With interaction, the logarithmic increase of static friction between 0.1s and 100s agree quantitatively with experimental observations [49].

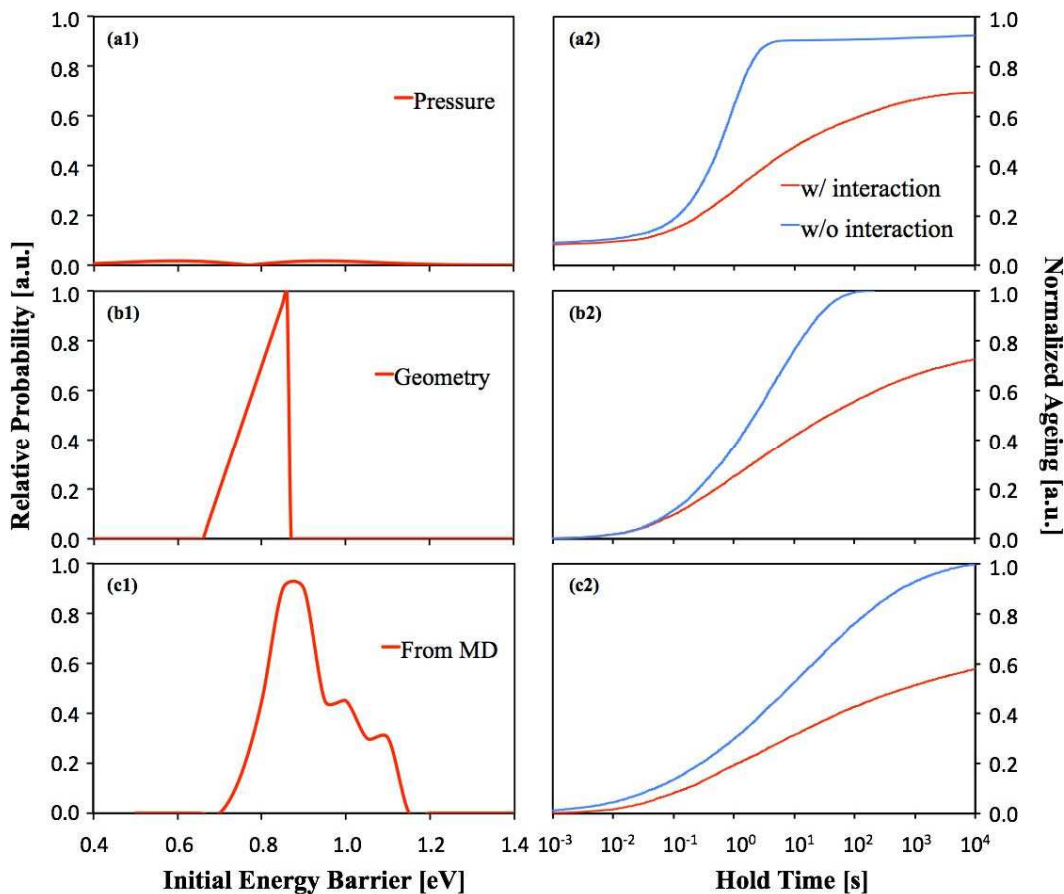


Fig. 3.5: Distributions of reaction barriers (left column) and the corresponding time evolutions of normalized ageing (right column). Reaction barrier distributions are (a1) the pressure-induced distribution, where the reaction energy barrier is controlled by atomic pressure; (b1) geometry-controlled distribution, where the orientation of hydroxyl groups on the surface determines the barrier (similarly as in [41]); and (c1) distribution directly calculated from MD simulations. In (a2)-(c2), red lines and blue lines represent time evolutions of ageing amplitude with and without considering interactions between neighboring siloxane bridges, respectively. Static friction of 1.0 corresponds to the strength of the interface when all siloxane bonds are formed and are independent of each other (*i.e.*, there is no decay of strength). From Tian *et al.* [1].

In short, the above simulation work suggests that when τ_0 is chosen to be 10^{-13} s, with a more realistic distribution of reaction energy barrier used and interactions between neighboring sites considered, the simulation results match the experimental results. Therefore, the uniform distribution of reaction energy barrier and the lack of consideration of interactions assumed in the current analytical analysis of the load and time dependence of ageing may be the cause of the unphysically large value of τ_0 . Nevertheless, this assumption allows for qualitative explanation of the trends in Fig. 3.1.

3.5: Possible relationship between nanoscale interfacial chemical bond-induced friction, macroscale friction, and the macroscopic rate and state friction laws

For materials like polymer glasses, it has been shown experimentally that the real contact area, as measured optically with a resolution of micrometers, increases logarithmically with time [79]. In this case, chemical bonds may not play an important role at the macroscale. This can be explained as follows. For a logarithmic increase of the number of chemical bonds with time for a given real contact area, the *rate* of bond formation *decreases* with time. Therefore, within any time interval, the bonds in the newly formed contact area (*i.e.*, those formed in that time interval) have a higher growth rate than the bonds in the previously formed area (*i.e.*, that formed before this time interval). Thus, the total number of chemical bonds formed should increase in a way that is faster than the logarithmic increase with time. As long as the rate of increase of real contact area is comparable to or greater than the rate of chemical bond formation, chemical bonding cannot be the main reason for macroscale ageing.

On the other hand, for materials like rocks, an increase in real area of contact during holding experiments has not been demonstrated, due to the high yield strength of silicate minerals and the resulting microscopic to submicroscopic asperity sizes, which cannot be measured precisely using optical techniques [80]. Indirect methods, using measurements of acoustic impedance normal to the frictional interface during hold experiments, indicate an increase in real contact area with hold time [81]. The difficulty of

determining the increase in contact area during ageing for rocks is compounded by the usual presence of wear debris, or "gouge", at the frictional interface, which contains myriad microscopic to submicroscopic frictional contacts. For these reasons, the relative contributions of asperity creep and chemical bond formation on macroscopic rock friction remain unknown.

It is important to discuss the likelihood that interfacial chemical bonds form at macroscale contacts based on our results. In our nanoscale experiments, the ageing phenomenon is sensitive to surface cleanliness. As shown in [49], if the tip is taken out of contact from the surface for some time, ageing is suppressed due to contamination. However, if the tip is scanned first, the contact is refreshed and shows ageing. This effect may be due to removal of hydrocarbon groups or other contaminants from the interface that came from the atmosphere, and/or from freshly exposing bonds on the tip due to bond breaking induced by scanning. We propose such refreshment could happen for macroscale contacts, since a macroscale sliding interface is constantly refreshing its asperity population [17].

3.6: Discussions of the novelty and physical importance of this work

It is evident that the increase of load will increase the contact area and thus the number of reaction sites N . However, prior to our work, no model or experiments had tested whether this contact area change for this system was linear or not. Moreover, increased load could also change the pressure, and thus affect the bond formation rate, since energy barriers can be pressure dependent. It is not at all obvious how the combined and potentially non-linear effect of load on contact area *and* energy barriers would change the number of bonds. The novelty of our work is to show that, for the experimentally-accessible range of loads and times we surveyed, the dependence is nearly linear.

To explain this in more detail, consider that according to a prior theoretical study [41] (also see Eq. (3.6)), the friction drop should be proportional to N/G , where G is the upper bound of the reaction energy barrier distribution, and could depend on pressure. Thus, how load will affect N/G is not evident *a*

priori. To reiterate the point of novelty expressed above, our experimental results show that N/G is approximately linear with load, a new finding. It is not at all evident that the number of sites should be simply multiplied with the log of the hold time, which is the analytically-derived result in our previous theoretical work for the particular case of a uniform distribution of energy barriers [41]. Note that those sites are likely not independent, as there are interactions between neighboring sites that affect the reactions, according to first principles calculations [41]); thus, it is not possible to know in advance how the number of sites and the time dependence will combine. In our nonlinear model for the contact area (Eq. (3.7)), the load will affect pressure and thus the bond formation rate. Thus, again, how the load and hold time terms combine is not evident *a priori*; no theoretical prediction of this existed previously, and no measurements had previously been published.

Therefore, one of the main points of novelty of our work is not only to show the load dependence of nanoscale frictional ageing for the first time for any material, but also to show *how* the load and time dependence of ageing combine for friction ageing at the nanoscale. By using the analytically-derived result from [41] to build one possible model, our experimental study is the first to show consistency with this previous theoretical work [41]. Our work proposes the first description of the load dependence of friction for an ageing contact, including extracting parameters like L_0 , the reaction energy barrier and the activation volume, for which conventional contact mechanics models like the DMT [82], JKR [83] and COS [84] models cannot be used.

3.7: Discussions of the "step" in the data in Fig. 3.1(b)

Notice that the trend (including the step at 245 nN load) of the six data points for a hold time of 100 s in Fig. 3.1(c) is quite similar to the trend in Fig. 3.1(b), suggesting they are related.

This "step" may indicate that the contact has a sudden change when the load reaches 245 nN, or there is some kind of saturation after the load reaches 245 nN. The linear fit used in Fig. 3.1(b) would thus

miss such important physical information. This concern implies that the "stepping" reflects some properties of the contact related to load.

To determine whether the step in the data in Fig. 3.1(b) is a physical effect or an artifact, we plot the load dependence of the slope of friction drop vs. $\log(t)$ (that is, a new Fig. 3.1(b)) after removing all six data points for the 100 s hold time in Fig. 3.1(a). The results show no "step" (Fig. 3.6). Therefore, we can confidently conclude that the "step" in Fig. 3.1(b) is just due to the anomalously large fluctuation of the friction drop data at long hold time (100 s), which is a reasonable outcome due to the larger variations in applied forces that occur at longer times. These fluctuations are not surprising, because according our experience, for long hold times, instrumental drift can lead to variations in the applied forces during the hold. In this case, drift of the laser signal could lead to higher applied loads than desired, thus leading to larger friction drops.

Therefore, though there is a step in Fig. 3.1(b), it is still reasonable to apply a linear fit.

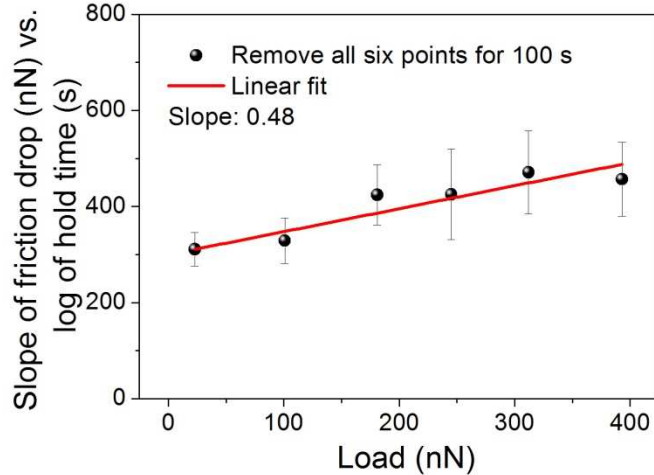


Fig. 3.6: Dependence of the slope of the friction drop vs. log hold time on load data after omitting the 100 s hold time in Fig. 3.1(a). From Tian *et al.* [1].

3.8: The validity of using Derjagin-Muller-Toropov model to establish the relationship of contact area and load

As discussed above, we were not able to accurately measure the adhesion force in FD tests for these experiments, because the adhesion is larger than the largest negative force that can be applied in the beyond the range of the deformation of the piezoelectric scanner of the AFM in the normal direction. However, by tuning L_0 to make all the data points in Fig. 3.1(a) converge as closely as possible into one master curve, we obtain $L_0 = 253$ nN. This L_0 is the adhesion of the contact of a silica tip on a piranha-cleaned silica substrate, before ageing occurs. Transmission electron microscopy shows that $R = 130$ nm. Under the DMT model, the work of adhesion $W = \frac{L_0}{2\pi R} = 0.306$ N/m; and under the JKR model, $W = \frac{L_0}{1.5\pi R} = 0.408$ N/m [3, 85].

Tabor's parameter $\mu = \left(\frac{16RW^2}{9E_C^2 z_0^3}\right)^{1/3}$ [84, 86], where z_0 is the equilibrium distance of silica surfaces.

If we choose a lower bound of $z_0 = 0.15$ nm, using $E_C = 35.3$ GPa, and using the upper bound value $W = 0.408$ N/m, corresponding to the JKR model, we can obtain the upper bound of $\mu = 2.09$, which indicates that our contact can be approximately described by the DMT model [84, 85].

3.9: Summary

In conclusion, we show that the friction drop for aged silica-silica contacts is approximately proportional to the product of the normal load and the log of the hold time above ~ 0.1 s contact time in the positive load regime. With respect to the load and time dependence of ageing in macroscale contacts, we propose that for those contact regions where the deformation is elastic [87], our model of the nanoscale ageing might be applied as a potential mechanism.

More generally, our work connects chemical kinetics and contact mechanics, provides further evidence that nanoscale RSF behavior originates from interfacial chemical bond formation, and establishes the applicability of RSF laws for nanoscale single-asperity contacts.

CHAPTER 4: A Physically-Based Rate and State Friction Law for Nanoscale Contacts

In this chapter, we establish a physically-based RSF law for nanoscale silica-silica contacts by combining the Prandtl-Tomlinson with temperature (PTT) model [88, 89] with an evolution effect, which is one of the main goals of our project. This Prandtl-Tomlinson with temperature and evolution effect (PTTE) model, like the PTT model, is a simple but physically-based model for describing the direct effect for single asperity contacts; it has been shown experimentally and with atomistic simulations that PTT model describes atomic-scale friction well [88-90]. However, unlike conventional RSF laws, PTTE model uses the loading point velocity for describing the direct effect, not the tip velocity. Also, in the PTTE model, the combination of the evolution and direct effects ends up being nonlinear. We present AFM data consistent with the PTTE model whereby in ageing tests, for a given hold time, static friction increases with the logarithm of the loading point velocity. Note that for the static ageing experiments in Chapter 3, any influence of the variation of the direct effect was avoided by using the same loading point velocity for each set of tests. Here, we show that the loading point velocity has an influence on the static friction force even though the hold time (*i.e.*, the amount of ageing) is kept constant. Also, note that knowledge of the direct effect can be used to understand stick-slip behavior, which is discussed in Chapter 6. Another manifestation of the direct effect seen in our experiments is that the kinetic friction increases with the logarithm of the loading point velocity at higher velocities reported in Chapter 5. According to the PTTE model, the rate of increase of friction with the log of velocity depends on the shape of the interfacial potential energy surface along the sliding direction. This discrepancy between static and kinetic friction arises from the fact that appreciable ageing during static contact changes the energy landscape. This helps establish how the conventional RSF laws can be modified for nanoscale single-asperity contacts to provide a physically-based friction law for nanoscale contacts that exhibit ageing.

4.1: Prandtl-Tomlinson with temperature model for atomic stick-slip

In the PTT model, the system is composed of the contact, the tip, and the cantilever, and the energy barrier is determined by the combination of the interaction energy between the tip and the substrate which is assumed to be a periodic function (due to the spatial periodicity of the substrate's crystal structure) and the elastic spring potential energy (including the potential energy stored in the deformation of the contact, the deformation of the tip, and the bending and twisting of the cantilever) (Fig. 4.1(a)). The loading point velocity, which is the loading velocity of the piezoelectric scanner controlling the relative position of the sample and the base of the cantilever, stays constant during stick-slip. The atomic stick-slip behavior of the tip on a substrate with periodic atomic structure naturally emerges as a series of repeating jumps of the system over potential energy barriers. Sticking corresponds to times when the system stays in a local energy valley, and slip occurs when the system jumps over an energy barrier. A master equation describing the change of the probability of the system staying in an energy well (*i.e.*, during stick) with time is used. The external applied lateral force F_L reduces the energy barrier ΔE according to $\Delta E = \frac{1}{\beta}(F_L^* - F'_L)^{3/2}$ [89], where β is a parameter depending on the shape of the potential energy landscape, F'_L is the applied lateral force, and F_L^* is the applied lateral force needed to make the energy barrier vanish at zero temperature. A theoretical derivation gives

$$\frac{1}{\beta k_B T} (F_L^* - F_L)^{3/2} = 2.3 \log\left(\frac{v_0}{v}\right) - 1.15 \log\left(1 - \frac{F_L}{F_L^*}\right) \dots \dots \dots (4.1)$$

where $v_0 = \frac{2f_0\beta k_B T}{3k_{eff}F_L^{*3/2}}$. Here, F_L represents the maximum applied lateral force in each stick-slip event (the static friction force), k_{eff} is the effective lateral stiffness of the system, f_0 is the characteristic vibration frequency in the potential, and v is the loading point velocity. At low v , F_L first increases with $\log(v)$ almost linearly, and then reaches a plateau (*i.e.*, F_L^*). The logarithmic, transition, and plateau regimes have been observed in experiments [88-90], one typical result of which is shown in Fig. 4.1(b).

An intuitive explanation of these velocity dependences of friction is as follows: at non-zero temperatures, due to thermal fluctuations the system has a finite probability of jumping over the energy barrier before the barrier is reduced to zero by the applied lateral force (the black curved arrow in Fig. 4.1(a) shows the jump). The greater the loading point velocity, the fewer the chances for the thermal energy to assist the system to jump over the barrier. With less assistance from the thermal fluctuations, the maximum applied lateral force needed to overcome the energy barrier will be larger, leading to larger friction. When the loading point velocity is large enough, thermal fluctuations have no effect on the jumping of the system, resulting in an athermal regime where friction is independent of velocity, as seen in Fig. 4.1(b).

When v is much smaller than the transition velocity, and thus F_L is much smaller than F_L^* , a linear approximation of the relationship between F_L and ΔE can be made: $\Delta E = \lambda(F_L^* - F_L)$ [88], where λ is a parameter that depends on the shape of the potential energy landscape. We define $\Delta E^* = \Delta E(F_L = 0) = \lambda F_L^*$, which is the energy barrier when there is no applied lateral force.

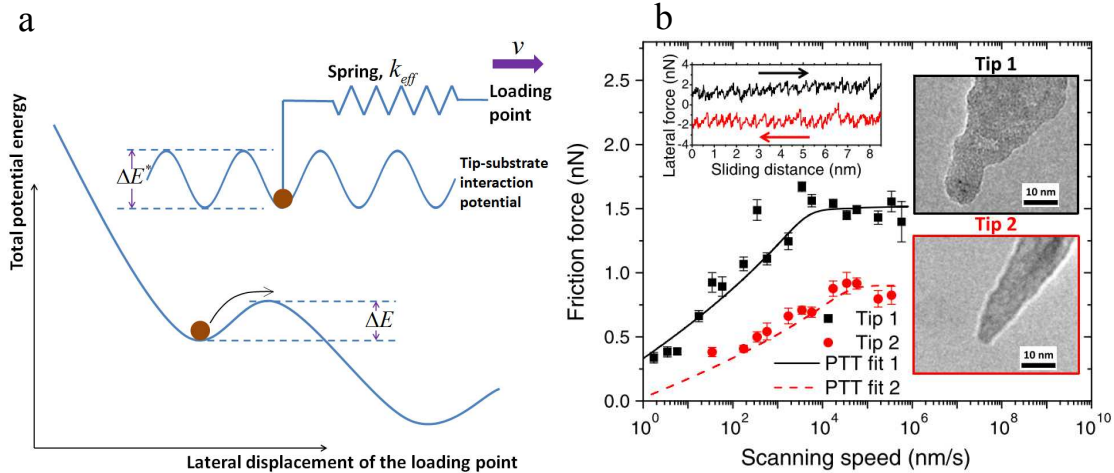


Fig. 4.1: PTT model. (a) Schematic of PTT model. The total potential energy is the sum of the tip-substrate interaction potential and the spring potential. In the inset on the top, the tip/block-spring model is

shown with spring stiffness k_{eff} and loading point velocity v . The tip-substrate interaction potential is modelled as sinusoidal with the barrier height being ΔE^* . For the total potential energy, the energy barrier under an applied lateral force is ΔE . For nonzero temperatures, thermal fluctuations assist the system in jumping over the energy barrier even when $\Delta E > 0$. (b) Typical friction vs. velocity data from atomic stick-slip experiments. The logarithmic increase, transition and plateau regimes could be seen. (b) is adapted from [90].

This linear approximation leads to the approximate friction equation:

$$F_L(v) = F_L^* + 2.3 \frac{k_B T}{\lambda} \log\left(\frac{v k_{eff} \lambda}{f_0 k_B T}\right) \propto \log(v) \dots \dots \dots (4.2)$$

Eq. (4.2) can also be obtained by performing a Taylor expansion of the term $(F_L^* - F_L)^{3/2}$ and ignoring the term $\log(1 - \frac{F_L}{F_L^*})$ in Eq. (4.1) under the assumption that $F_L \ll F_L^*$.

The connection between β and λ is as follows. Performing a Taylor expansion on $\Delta E(F_L) = \frac{1}{\beta} (F_L^* - F_L)^{3/2}$ for small F_L gives:

$$\Delta E = \frac{1}{\beta} (F_L^* - F_L)^{3/2} = \frac{1}{\beta} F_L^{*3/2} (1 - F_L/F_L^*)^{3/2} \approx \frac{1}{\beta} F_L^{*3/2} \left(1 - \frac{3 F_L}{2 F_L^*}\right) = \frac{3}{2\beta} F_L^{*1/2} \left(\frac{2 F_L^*}{3} - F_L\right)$$

Comparing this to $\Delta E = \lambda(F_L^* - F_L)$, we obtain that $\lambda = \frac{3 F_L^{*1/2}}{2\beta}$.

Although in the PTT model (and in the original Prandtl-Tomlinson (PT) model) the interaction potential between the tip and the substrate is assumed to be periodic (*i.e.*, the substrate is a crystal), the derivations of Eq. (4.1) and Eq. (4.2) do not actually require periodicity of the interaction potential (see the derivations in [88, 89]). Therefore, we extend the PTT model to amorphous substrates in this work. Additionally, since in this work we do not reach plateau regime, from now on when we discuss the velocity

dependence of friction, we will use the linear approximation of Eq. (4.2) rather than Eq. (4.1) for simplicity.

4.2: Prandtl-Tomlinson with temperature and evolution effect model for nanoscale interfacial chemical bond-induced friction

The key new ingredient we now add is to allow the intrinsic energy barrier of the tip-sample potential ΔE^* to increase with time due to ageing. In static ageing tests (*i.e.*, SHS tests) for silica-silica single asperity contacts (like those in [1, 49]), if the loading point velocity or the hold time is large enough, then the hold time is much larger than the time during which the lateral force is increasing, before the tip slips. In this case, most of the ageing occurs before lateral loading starts, so we can approximate that ΔE^* during lateral loading is constant. Thus, we can directly use the PTT model for our contacts (note that one condition of the PTT model is that ΔE^* and thus F_L^* are independent on time during the lateral loading process).

Since F_L^* is the applied lateral force needed to make the energy barrier vanish at zero temperature, it is reasonable to assume that F_L^* is proportional to the total number of interfacial chemical bonds formed. According to previous studies on the ICBI ageing at the nanoscale, the number of interfacial chemical bonds increases logarithmically over a wide range of hold times [1, 41, 49]. Therefore, $F_L^*(t) = F_{L,0}^* + B \log(t)$, where both $F_{L,0}^*$ and B are constants. At the end of the hold, $F_L^*(\tau) = F_{L,0}^* + B \log(\tau)$, where τ is the hold time. Since λ depends on the shape of the potential energy landscape, it should be a function of τ , thus giving

$$F_L(v, \tau) = F_{L,0}^* + B \log(\tau) + 2.3 \frac{k_B T}{\lambda(\tau)} \log\left(\frac{v k_{eff} \lambda(\tau)}{f_0 k_B T}\right) \dots \dots \dots (4.3)$$

Eq. (4.3) could be considered as a physically-based RSF law for nanoscale single asperity contacts, where an evolution effect (*i.e.*, the terms depending on time) is incorporated into the PTT model. We call this the Prandtl-Tomlinson with temperature and evolution effect (PTTE) model.

4.3: Experimental evidence for and discussions of the Prandtl-Tomlinson with temperature and evolution effect model

We comment that our Eq. (4.3) are similar to Eq. (8) in Ref. [91] by Mazo *et al.*, which is another recent model for time-strengthening (*i.e.*, ageing) of nanocontacts. Both our work and Mazo *et al.*'s work incorporate the ageing effect into the PTT model. There are several differences between our work and theirs. First, their model is specifically formulated to describe atomic stick-slip behavior (*i.e.*, for a crystalline sample) although, like our model, it can readily be extended to non-periodic systems. Second, Mazo *et al.*'s model is inspired by observations supporting atomic attrition or creep of the contact, *i.e.*, a change in "contact quantity", whereas our model aims to incorporate ageing due to interfacial chemical bond formation, *i.e.*, change of "contact quality". Third, our model considers static ageing during a hold period that occurs before lateral loading occurs, while Mazo *et al.* describe the ageing that occurs during the periodic lateral loading of atomic stick-slip behaviour. In our model, the evolution of the contact for the stick phase during lateral loading is ignored, making the application of the PTT model during lateral loading feasible (note that the derivation of PTT model requires no evolution of the contact during stick). In contrast, Mazo *et al.* assume that the first time derivatives of certain parameters (such as the interaction potential) are slowly varying, thus allowing for ageing during the stick phase of lateral loading. Fourth, in our model, the ageing is assumed to be logarithmic with time (based on our prior results), while in Mazo *et al.*'s work, the ageing is assumed to be exponential with time. Thus, while both models integrate ageing with thermally-assisted slip, they are designed for different physical mechanisms of ageing and accordingly use different assumptions and produce different predictions.

The PTTE model then requires that the conventional RSF laws must be modified in at least two respects if they are to be applied at the nanoscale. The first modification is the physical meaning of the velocity in the RSF laws. In conventional RSF laws, the velocity refers to the velocity of the block, while for the PTTE model, it refers to the loading point velocity. This difference is due to the fact that macroscale and microscale contacts are made of many single asperities, and there is no true static state (*i.e.*, zero velocity) for the block (since the block is always connected to other materials, *e.g.*, the springs in laboratory rock friction experiments or other rocks at natural faults, there is always some non-zero external lateral force applied on the block, causing the interfacial asperities to break and resulting in slow motion of the block). Therefore, the block velocity v_{block} in Eq. (1.1) will never be zero, and there is no problem with using v to determine the direct effect (*i.e.*, $\log(v)$ will not diverge). However, for ICBI friction for nanoscale single asperity contacts, the AFM tip can stick on the substrate in a true static state, even if there is large external lateral force applied (see the linearity of the stick regime in Fig. 4.2 and Fig. 3.1, indicating no partial slip or appreciable tip motion during stick, and multiple molecular dynamics simulations of contacts, wherein the interface is completely stable during sticking [50, 90, 92]). Therefore, the velocity of the tip can be zero, and the logarithm of the velocity will diverge. In contrast, since v is the loading point velocity rather than the tip velocity, and is always non-zero, we thus avoid this problem.

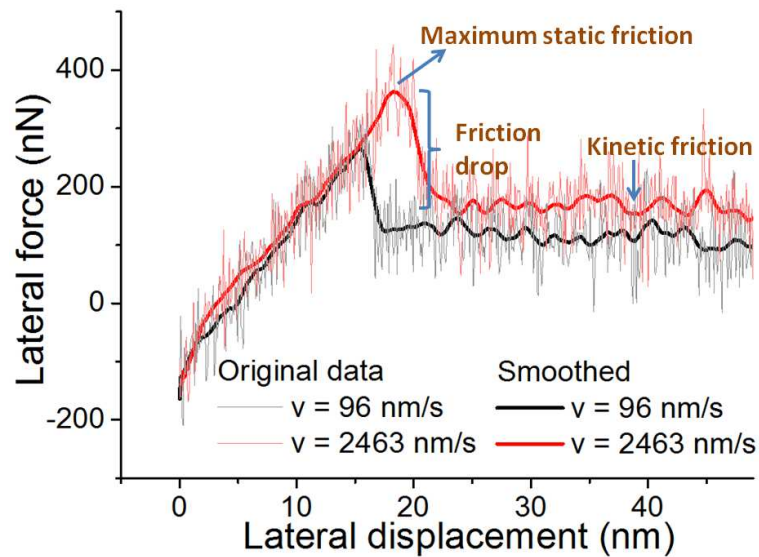


Fig. 4.2: Lateral force vs. lateral displacement for two loading point velocities. Both original data and the smoothed curves (to reduce noise) are shown. The measurement of the maximum static friction, the kinetic friction and the friction drop are also shown. At the larger loading point velocity, the maximum static friction and the kinetic friction are both larger. RH = 45 %, temperature = 24 °C, applied normal load = 149 nN, adhesion = 682 nN, hold time = 4.64 s.

The second modification is in the way the direct and evolution effects combine. In conventional RSF laws (Eq. (1.1)), since both parameters a and b are constants, the direct and evolution effects are linearly combined. However, in the PTTE model (Eq. (4.3)), since the pre-factor of the direct effect term— $2.3 \frac{k_B T}{\lambda(\tau)}$ —is a function of time, the direct and evolution effects are convoluted in a nonlinear manner.

We now show experimental evidence of the logarithmic increase of friction with the loading point velocity, and the nonlinear combination of the direct and evolution effects. Fig. 4.2 shows how we measure the maximum static friction, the kinetic friction, and the friction drop. Measurements at two different loading point velocities are shown and, despite having the same hold time, the static friction is clearly higher for the higher loading point velocity. Fig. 4.3 shows, for two different hold times, how these three forces vary with a range of loading point velocities. For a 1.28 s hold time, the maximum static friction and the kinetic friction both increase with log of velocity linearly, with almost the same increasing rate (Fig 4.3(a)). The logarithmic increase of the maximum static friction with loading point velocity corroborates the direct effect term in Eq. (4.3). For this hold time, the friction drop (the difference between the maximum static friction and the kinetic friction), happens to be nearly independent on velocity. For the hold time is 4.64 s (Fig. 4.3(b)), the slopes of the maximum static friction and the kinetic friction vs. log of velocity happen to differ more, leading to a non-zero slope of the friction drop vs. velocity. The different increase rates of the maximum static friction and the kinetic friction versus the velocity are interesting as

they indicate that the combination of the direct effect and the evolution effect are nonlinear. This is discussed in more detail below.

In Fig. 4.3 (b), during smooth sliding, since the velocities are large (greater than *ca.* 100 nm/s), the evolution effect is largely suppressed and there will be few interfacial chemical bonds formed during sliding (more discussions on the dependence of the kinetic friction on the velocity and the suppression of the evolution effect during sliding are in Chapter 5). If we assume that the seemingly smooth sliding we observe at large velocities is actually irregular stick-slip, which results from the amorphous atomic structure of the substrate and tip and is thus "blurred" due to the large tip radius (*ca.* 125 nm) in our experiments, then we can use the PTT and PTTE model to describe the kinetic friction at large velocities. If the direct effect and the evolution effect were linearly combined the pre-factor of the direct effect (which is the rate of increase of friction with the log of velocity) would be constant and independent of the magnitude of the evolution effect. Thus, the rate of increase of the maximum static friction and the kinetic friction with log of velocity would be the same. This contradicts our observations of the different slopes of the maximum static friction and the kinetic friction vs. log of velocity in Fig. 4.3(b), indicating that our assumption that the direct effect and the evolution effect are linearly combined is false. Therefore, in Fig. 4.3(b) the combination of the direct effect and the evolution effect is nonlinear, consistent with the PTTE model (Eq. (4.3)) we established.

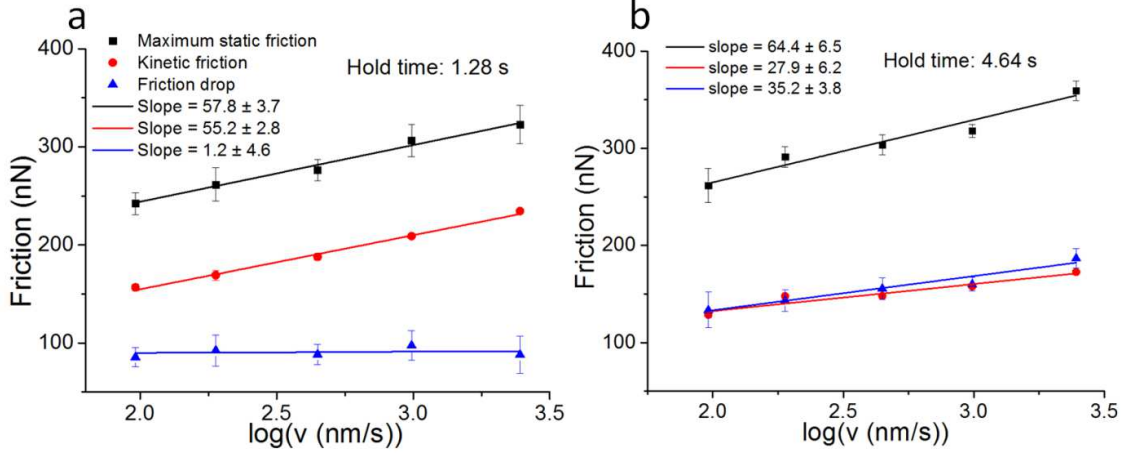


Fig. 4.3: Friction vs. log of velocity for different hold times. (a) Results showing the maximum static friction, kinetic friction, and friction drop vs. loading point velocity for a 1.28 s hold time. Both show a logarithmic increase with v . The friction drop happens to be almost independent of velocity since the slope of the maximum static friction and kinetic friction with log of velocity are the same. (b) Results showing the maximum static friction, kinetic friction, and friction drop depend on loading point velocity for a 4.64 s hold time. The maximum static friction, kinetic friction, and friction drop all increase with velocity logarithmically (the slope of the maximum static friction with log of velocity is rather different than that of the kinetic friction, resulting in a clear dependence of the friction drop on v). For both (a) and (b), the loading point velocity is varied randomly to exclude systematic error. The conditions are the same as those in Fig. 4.2, and the same tip is used.

We comment that in Eq. (4.3), the dependence of friction on hold time τ varies as $B\log(\tau)$ (the second term in Eq. (4.3)) but, due to the third term, it also has a hold time dependence given by $2.3\frac{k_B T}{\lambda(\tau)}\log\left(\frac{v k_{eff}\lambda(\tau)}{f_0 k_B T}\right)$. However, our studies on ICBI ageing (Chapter 3 and [49]), and simulations [41] all show a $\log(\tau)$ dependence of friction for a given loading point velocity. Yet we do see that the velocity dependence of friction is significant. Therefore, the third term in Eq. (4.3) is not negligible. This suggests

that the third term in Eq. (4.3) $2.3 \frac{k_B T}{\lambda(\tau)} \log\left(\frac{v k_{eff} \lambda(\tau)}{f_0 k_B T}\right)$ is approximately linear with $\log(\tau)$. Additional studies are needed to explore this further and to identify the functional dependence of λ on hold time τ .

We also comment that in our experimental studies on ICBI ageing at the nanoscale [1, 49] (see Chapter 3), the friction drop is measured to represent the ageing amplitude. However, the independence of friction drop on loading point velocity in Fig. 4.3(a) indicates that friction drop is not a good measure for ageing if the loading point velocity varies; in such a case, a more comprehensive analysis is required to separate state (ageing) effects from rate effects. The PTTE model presented here allows such analysis to be conducted.

4.4: Summary

In conclusion, we establish the PTTE model which is a physically-based RSF law for nanoscale single asperity contacts that combines a physically-based direct effect with the evolution effect validated from prior and current experiments, and modelling of those experiments. In the PTTE model, the velocity for the direct effect is not the velocity of the tip, but the loading point velocity. Also, the direct effect and the evolution effect do not necessarily combine linearly. The PTTE model is consistent with our experimental observations that in ageing tests, for a given hold time, the maximum static friction increases logarithmically with the loading point velocity. Also, the nonlinear combination of the direct and the evolution effects are consistent with our experimental findings that the rate of increase of the maximum static friction and the kinetic friction with \log of the loading point velocity could be different. These results show how conventional RSF laws should be modified for nanoscale single asperity contacts exhibiting ageing and establish a new, physically-based frictional law for nanoscale contacts. Additionally, the observations of the logarithmic dependence of friction on velocity for amorphous silica-silica contacts extends the PTT model to amorphous substrates.

Chapter 5: Kinetic Friction and Memory Distance for Interfacial Chemical Bond-Induced Friction at the Nanoscale

In friction experiments on rocks and other materials, such as paper and polymer glasses [6, 21, 30], a memory effect is observed and is incorporated into the phenomenological rate and state friction (RSF) model. As discussed in Chapter 1, Section 1.1, in the RSF model, the memory distance D_c is defined as the sliding distance required for the population of contacts at a given sliding velocity to renew itself, or in other words, for changes due to the evolution effect to no longer be apparent [6]. This critical sliding distance D_c provides a conceptual link between static ageing and kinetic friction, and is crucial for understanding the often-observed logarithmic decrease of kinetic friction with sliding velocity [43]. However, like memory effects in many other fields, the memory distance is empirically-based, and equations or physical models to derive it are lacking. In this study, we use atomic force microscope (AFM) to study interfacial chemical bond-induced (ICBI) kinetic friction for nanoscale single-asperity silica-silica contacts. We find that, at lower velocities, kinetic friction decreases logarithmically with sliding velocity (due to the existence of a memory effect), and then increases logarithmically with velocity at higher sliding velocities. At higher velocities, the evolution effect is small, and overwhelmed by the direct effect, whereby friction increases with velocity due to there being less time available for thermal energy to assist sliding (as discussed in the PTTE model in Chapter 4). We propose that the observed logarithmic decreasing trend of friction with velocity, and the memory effect, could be explained by: (1) conservation of the number of interfacial bonds present during steady sliding; (2) the assumption that during low-velocity sliding, immediately after an interfacial chemical bond breaks, the resulting dangling bond can easily bond with other dangling bonds on the opposing surface until it becomes passivated by another chemical species. Thus, the memory distance represents the average sliding distance before this passivation event occurs. This assumption is consistent with the observation of the partial drop of the lateral force in some slip events in the transition regime between quasi-periodic stick-slip (which is further shown and studied in Chapter 6) and stable sliding.

5.1: Velocity dependence of kinetic friction

Sliding rock surfaces are comprised of multiple asperities with sizes as small as nanometers. To better understand the physical basis of the memory distance, we measure the dependence of kinetic friction on sliding velocity for single-asperity, silica-silica nanocontacts using AFM. We find that at lower velocities, kinetic friction first decreases with velocity logarithmically, and then increases with velocity logarithmically at higher velocities, as can be seen in Fig. 5.1(a). Fig. 5.1(b) and (c) show the logarithmic decrease and increase of kinetic friction with velocity, respectively, from additional experiments.

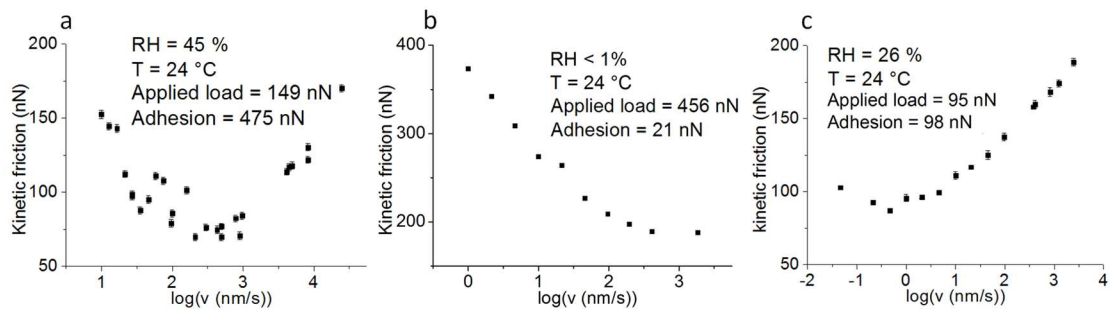


Fig. 5.1: The dependence of kinetic friction on sliding velocity in the steady sliding regime. Kinetic friction first decreases linearly, then increases linearly, with log velocity. (a) Results showing a logarithmic decrease in friction with velocity at lower velocities, and a logarithmic increase in friction with velocity at higher velocities. (b) Results from another experiment showing the logarithmic decrease in friction with velocity which levels off prior to the increase with velocity that would occur at higher velocities. (c) Another result showing the tail end of the logarithmic decrease of friction with velocity, followed by a logarithmic increase with velocity. The AFM tips and the experimental conditions given in the insets are different in (a), (b), and (c). For each test, the velocity is varied randomly to exclude systematic errors.

It is important to note that the AFM tips and experimental conditions (humidity, applied load, and adhesion force) in the experiments that yield the data in Fig 5.1(a), (b) and (c) are all different. Also, even for the same tip under the same conditions, frictional properties may vary might be different at different times and different locations on the substrate due to the variation of surface chemistry with time and space caused by contaminants, which is further discussed in Section 5.5.

Therefore, the transition velocities at which the logarithmic decrease in friction with velocity terminates are different in the three tests in Fig. 5.1. We note that a logarithmic decrease of friction with velocity – so-called velocity weakening behaviour – is often observed in experiments on rocks and other materials [30, 42, 93, 94].

The transition from decreasing to increasing friction with increasing velocity can be explained as follows: As velocity increases, contact lifetimes decrease such that there is less time available for contact ageing, resulting in lower friction at higher sliding velocities. Above a critical velocity there is insufficient time for contact ageing such that the direct effect dominates. This leads to the logarithmic increase of friction with velocity. In most of the experiments we performed, the transition velocity where the decrease of kinetic friction with velocity deviates from logarithmic (*i.e.*, where friction begins to level off) ranges from 5 to 68 nm/s, as shown in Fig. 5.2.

The method used for estimating the transition velocity is also shown in Fig. 5.2. Fig. 5.2(a) and (b) contain the same sets of data as in Fig. 5.1(a) and (b), respectively. Fig. 5.2(c) to (e) are three additional sets of data. In Fig. 5.1(c), since there are only two data points in the decreasing friction regime, it is not possible to determine the transition velocity. However, we can at least conclude that the transition velocity in Fig. 5.1(c) is smaller than 1 nm/s. From all six sets of data we see that, in most cases, the range of values of the transition velocity is found to be somewhere between 5 nm/s to 68 nm/s (with the only outlier to the lower bound in Fig. 5.1(c) and the only outlier to the upper bound in Fig. 5.2(e)). This range of values is

reasonable considering that the tests are conducted for a range of loads, tips, humidities, and at different locations on the sample, where there may be varying areal densities of contaminant molecules and hydroxyl groups bound to the silica surface.

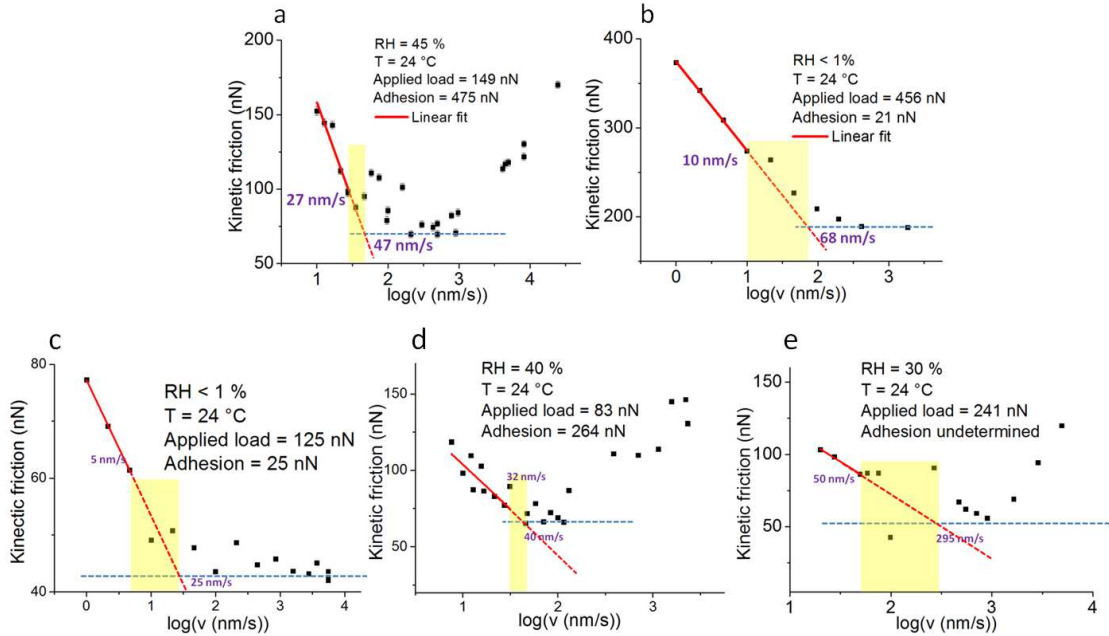


Fig. 5.2: Measurement of the transition velocity where the dependence of the kinetic friction on velocity deviates from logarithmic. (a) corresponds to Fig. 5.1(a) and (b) corresponds to Fig. 5.1(b). (c), (d) and (e) are from additional tests. In (a), the left-most five points are fit linearly and extended with a dashed red line, with a velocity of the fifth point of 27 nm/s. The y-value of the horizontal dashed blue line is the mean value of the kinetic friction of the lowest three points. The dashed blue line and dashed red line intersect at 47 nm/s. Thus, we estimate that the transition velocity in (a) is between 27 and 47 nm/s, as indicated in the light yellow colored region. In (b), the leftmost four points are fit linearly, and extended with a dashed red line, with a velocity of the fourth point of 10 nm/s. The y-value of the horizontal dashed blue line is the mean value of the kinetic friction of the two rightmost points. The dashed blue line and dashed red line intersect at 68 nm/s. Therefore, we estimate a transition velocity in (b) between 10 nm/s and 68 nm/s. In (c), the leftmost three points are fit linearly, and extended with a dashed red line, with a

velocity of the third point of 5 nm/s. The y-offset of the horizontal dashed blue line is the mean value of the kinetic friction of the rightmost two points. The dashed blue line and dashed red line intersect at 25 nm/s. Thus, we estimate that a transition velocity in (c) between 5 nm/s and 25 nm/s. In (d), the leftmost nine points are fit linearly, and extended with a dashed red line, with a velocity of the ninth point of 32 nm/s. The y-offset of the horizontal dashed blue line is the mean value of the kinetic friction of the lowest three points. The dashed blue line and dashed red line intersect at 40 nm/s. Thus, we estimate a transition velocity in (d) between 32 nm/s and 40 nm/s. In (e), the leftmost three points are fit linearly, and extended with a dashed red line, with a velocity of the fifth point of 50 nm/s. The y-offset of the horizontal dashed blue line is the mean value of the kinetic friction of the lowest three points. The dashed blue line and dashed red line intersect at 295 nm/s. Thus, we estimate that the transition velocity in (e) is between 50 nm/s and 295 nm/s.

We note that, in ageing tests for a single-asperity silica-silica contact, the transition time at which the regime of logarithmically increasing static friction vs. contact time begins is between 0.1 and 1 s. Below this transition time, the dependence of static friction on contact time levels off with decreasing contact time, as can be seen in Fig. 5.3 (our experimental results) and [41] (simulation results). Therefore, we can estimate the memory distance by multiplying the transition velocity by the transition time, yielding a memory distance for our single asperity silica-silica contacts of between 0.5 and 68 nm. For comparison, the contact size in our experiments, twice the contact radius, is estimated from the DMT model to fall between 10 and 30 nm for all tips and loads used. The large range of memory distances falls well outside the range of calculated contact diameters in our experiments, demonstrating that refreshing the contact is not simply a matter of sliding a distance equal to the contact size. One clear example to support this is shown in Fig. 5.1(c), where the transition velocity is at most 1 nm/s; since the transition time in Fig. 5.3, where the same tip and conditions are used as in Fig. 5.1(c) is at most 1 s, the memory distance is then at most 1 nm, which is much smaller than the contact diameter. Note that the static friction for a 1 s hold in Fig. 5.3 (which is measured at the beginning of the test, and is 253.5 ± 8.3 nN) is only 6.5% different than

the static friction for a 1 s hold measured immediately after the test in Fig. 5.1 (c) (which is 271.2 ± 7.4 nN), indicating that there were no significant surface chemistry changes between the test yielding the data in Fig. 5.3 and the test yielding the data in Fig. 5.1 (c). This large range of values of memory distance likely also reflects large variations in surface chemistry, such as the density of surface -OH groups, and surface-bound contaminants.

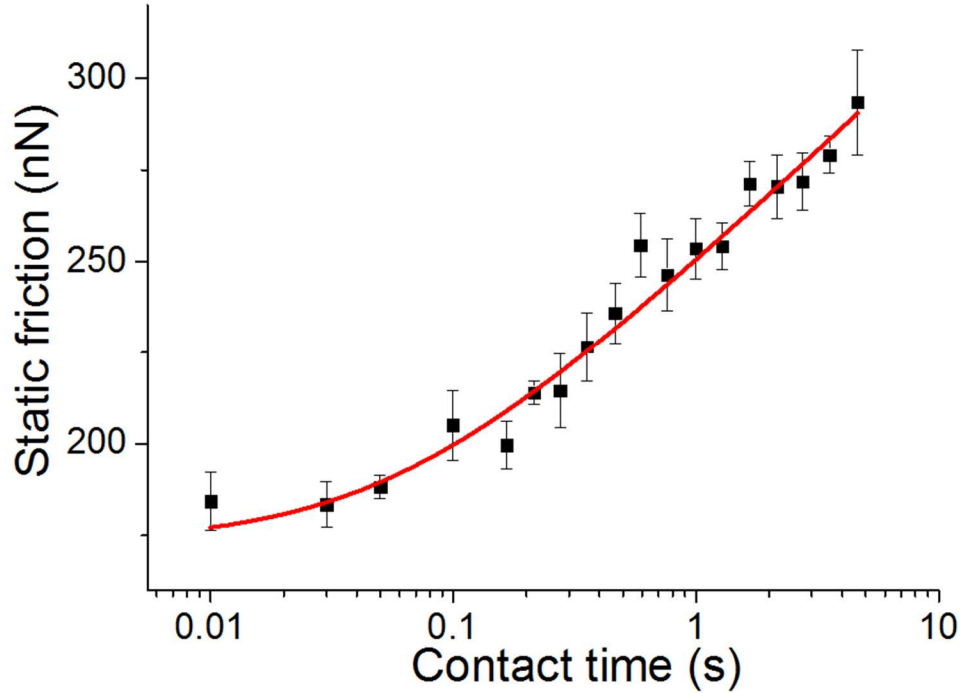


Fig. 5.3: Results of a static ageing test. The contact time is the sum of hold time and stick time. The hold time is varied randomly to exclude systematic errors. The tip and conditions are the same as those in Fig. 5.1 (c), and the test was conducted just before the test in Fig. 5.1 (c). The static friction for the 1 s hold time (which is measured at the beginning of the test, and is 253.5 ± 8.3 nN) is only 6.5% different than the static friction for 1 s hold time (271.2 ± 7.4 nN) measured immediately after the test done in Fig. 5.1 (c) indicating that there were no significant surface chemistry changes between these two tests. The dependence of ageing on time deviates from logarithmic between 0.1 s and 1 s. The red curve is a fit to the function $F = F_0 + g \cdot \log(1 + \frac{t}{\tau})$, where F is the static friction, F_0 is the offset of static friction, g is a

constant, and τ is some characteristic transition time. As discussed in Section 1.1, this form of the RSF law avoids the singularity when t approaches zero. The value of τ extracted in this way is 0.058 ± 0.025 s. We comment that the transition time extracted in this way is expected to be smaller than the time where the ageing vs. time begins to deviate from the logarithmic trend.

5.2: A fundamental explanation of the logarithmic decrease of kinetic friction with velocity and the memory distance

We now provide a physically-based model for the origin of the memory distance and the resultant logarithmic decrease of kinetic friction with velocity for ICBI friction at the nanoscale.

As illustrated in Fig. 5.4, we focus on one reaction site "X" on the upper surface of the contact. Before the tip contacts the substrate, X is terminated by an -OH group, so we refer to it as being "passivated". During sliding, say at time t_0 (corresponding to Fig. 5.4(b)), site X undergoes a condensation reaction by forming a siloxane bond (Si-O-Si) with another silanol group on the substrate surface. Site X is now referred to as being in an "activated, bonded" state. The presence of this bond contributes to the friction force, as shown by Li *et al* [50]. This siloxane bond will break after the tip slides a distance Δl , which is the average length one siloxane bond can be stretched before breaking and thus will be of the order of a fraction of an atomic bond length. The stretched bond state is shown in Fig. 5.4(c). Immediately after the bond breaks, site X is now a dangling bond (either Si- or Si-O-). In this reactive, high energy state, it can easily form an interfacial covalent bond (such as Si-O-Si, Si-Si, *etc.*) with other dangling bonds on the substrate, as shown in Fig. 5.4(d) and (e). We refer to this state as an "activated, dangling bond". After it forms an interfacial bond in this manner, the bond will eventually break as sliding continues, and site X will enter into the high energy dangling bond state again. This process of bond formation and bond rupture (Fig. 5.4(b) through (e)) will occur repeatedly during sliding. Along with sliding, site X can interact with other surface atoms and functional groups anchored to the substrate (these could be -OH groups, or

water/hydrocarbon molecules physisorbed to the substrate), and thus eventually re-hydrolyze or otherwise become inactive (become attached to a H atom), as shown in Fig. 5.4(f). The sliding distance in which this lower-probability passivation event occurs is, on average, D_c . Thus, D_c is determined by the density of the surface groups which successfully saturate dangling bonds on the opposing surface. The activated state of site X ends when it becomes hydrolyzed again to form a silanol group, or becomes terminated by an H atom. The lifetime of the activated state τ (be it bonded, or dangling) will, on average, be given by $\tau = D_c / v$. We set the ratio of the average amount of time X is in the activated, bonded state to its average total time in the activated state (bonded plus dangling bond) to be β , which is assumed to be a constant. A justification for assuming β to be a constant is provided below.

We assume the process of bond breaking and reformation repeats a total of m times before an active site X becomes passivated. The total time when X is part of an interfacial bond is $T_{bond} = m \cdot \bar{\Delta}l / v$, where $\bar{\Delta}l$ is the average maximum length that interfacial bonds can be sheared before they fail, leaving dangling bonds. So $\beta = T_{bond} / T = \frac{m \cdot \bar{\Delta}l / v}{D_c / v} = m \cdot \bar{\Delta}l / D_c$. Note that m is determined by the density of reaction sites and the density of anchored molecules on the substrate, so it is a constant and $\bar{\Delta}l$ and D_c are also constants. Therefore, β is a constant.

We now consider the steady-state behavior during sliding, where the total number of activated, bonded sites N , and the total number of activated sites (bonded plus dangling bonds), N/β , both remain constant, including at the initial time t_0 . In other words, at time t_0 there are N/β activated sites. On average, from t_0 to $t_0 + \tau$, all of these N/β sites will become passivated. Over the same time interval, if we assume the ageing law can be applied during sliding, then the number of newly formed siloxane bonds, *i.e.*, the number of sites which become activated, is proportional to $\log(\tau) = \log(D_c / v)$. Since the number of activated sites is a constant, during τ , the number of sites that become passivated must be equal to the number of sites which are activated. Therefore, $N/\beta \propto \log(D_c / v)$. Thus $N \propto \log(D_c / v)$. Assuming that the

kinetic friction f is proportional to N , we obtain $f \propto \log(D_c/v)$, which explains the logarithmic decrease of kinetic friction with velocity and the physical meaning of the memory distance D_c .

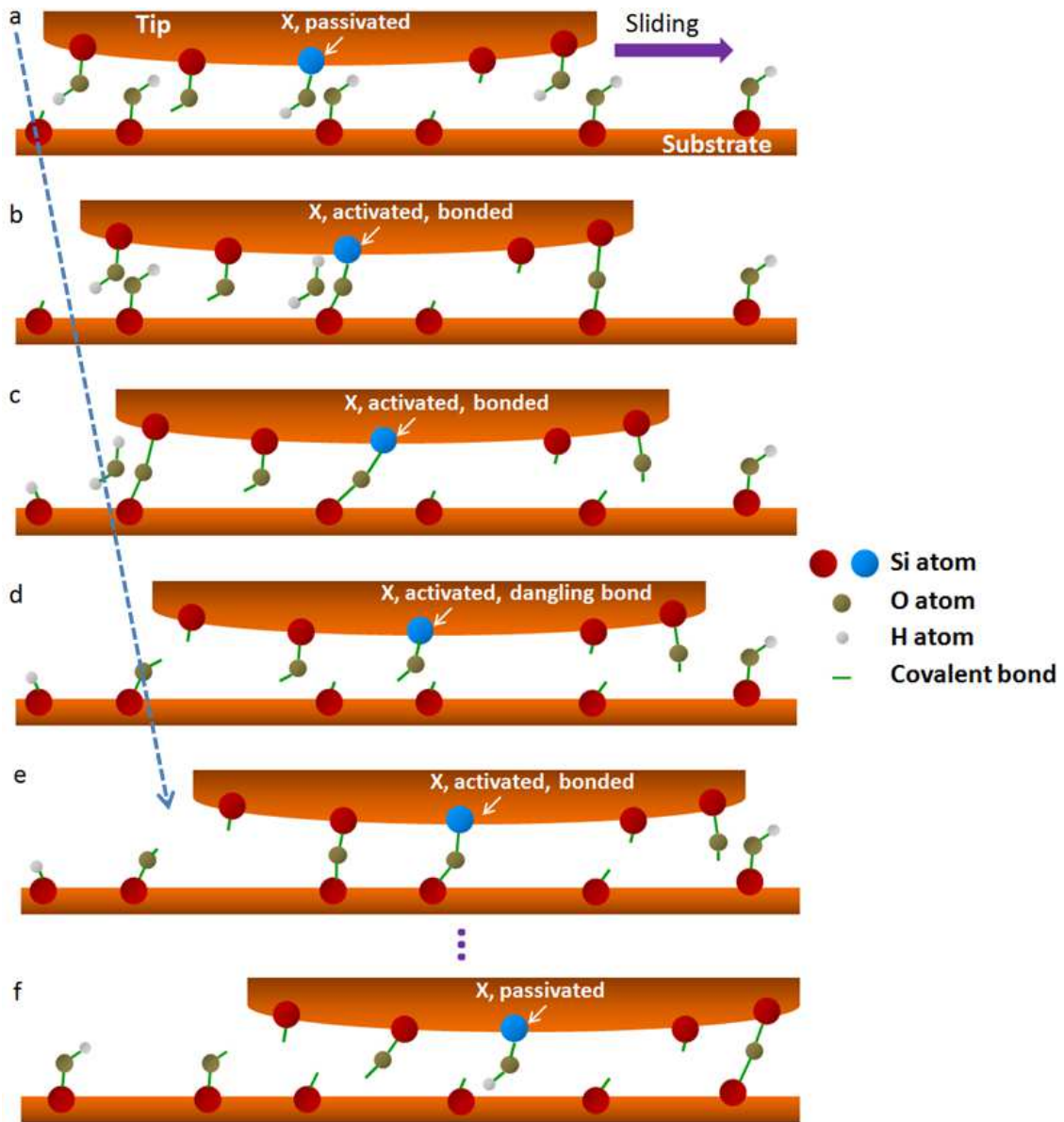


Fig. 5.4: Schematic of the life cycle of reaction sites. The silicon atom of reaction site X is colored blue. From (a) to (e), the tip continuously moves to the right with equal displacement between each successive figure, followed by a larger displacement between (e) and (f). The dashed blue line is to guide the eye. In

(a) to (e) the same region of the substrate is shown. (f) corresponds to the configuration wherein the tip has moved a distance D_C and site X becomes passivated, and represents a different region of the substrate than the one shown in (a) through (e).

5.3: Experimental results corroborating our explanation

Our experimental findings are consistent with the picture described above. In the experiments, when the loading point velocity (the velocity of the piezoelectric scanner controlling the relative position of the sample and the base of the cantilever) is small enough, we typically observe quasi-periodic stick-slip behavior, as shown in Fig. 5.5(a). As velocity increases, the peak-to-trough amplitude of the stick-slips decreases, and stick-slip behavior finally transitions into steady sliding (further details of these stick-slip phenomena will be presented Chapter 6). This behavior is consistent with stick-slip behavior observed in many larger-scale systems [95-97] (we note that this behavior is distinct from atomic lattice stick-slip behavior, which results from the periodic interfacial potential due to the crystallinity of the substrate [88, 89, 98]). In the transition regime, for velocities between those that yield quasi-periodic stick-slip and those that yield steady sliding, some slip events show only a partial force drop, as seen in Fig. 5.5(b). This novel and interesting phenomenon can be explained as follows. In each slip event, as soon as slip commences, we assume that all interfacial siloxane bonds break simultaneously [50], and become dangling bonds. When the loading point velocity is small and thus the stick-slip amplitude is large, the peak lateral force at the beginning of each slip event is large, due to ageing that occurs during the stick portion of the cycle. Thus, as the tip slips, the applied force on the interface, including the force from the cantilever's torsional deformation and forces due to the deformation of the tip and the contact, is large enough to overcome any resistive force due to reforming of siloxane bonds between dangling bonds on the tip and the substrate during slip. As slip begins, the tip initially accelerates, and inertia further assists in overcoming any resistive force due to interfacial bond formation. Eventually, as the cantilever relaxes during slip, the force

it applies to the interface decreases until the motion eventually stops, with the lateral force now at a lower, relaxed value.

However, at higher velocities in the transition regime, the stick-slip amplitude is smaller so the force applied to the interface is smaller at the beginning of each slip event. For some slip events, the resistive force due to stochastic formation of interfacial siloxane bonds may be sufficient to terminate tip motion earlier than for other slip events. Thus, the lateral force relaxes only partially and the slip distance differs from one slip event to another; a reflection of the stochastic nature of reactions between dangling bonds that occur during slip. This partial slip phenomenon corroborates the physical picture of dangling bonds forming siloxane bonds described above.

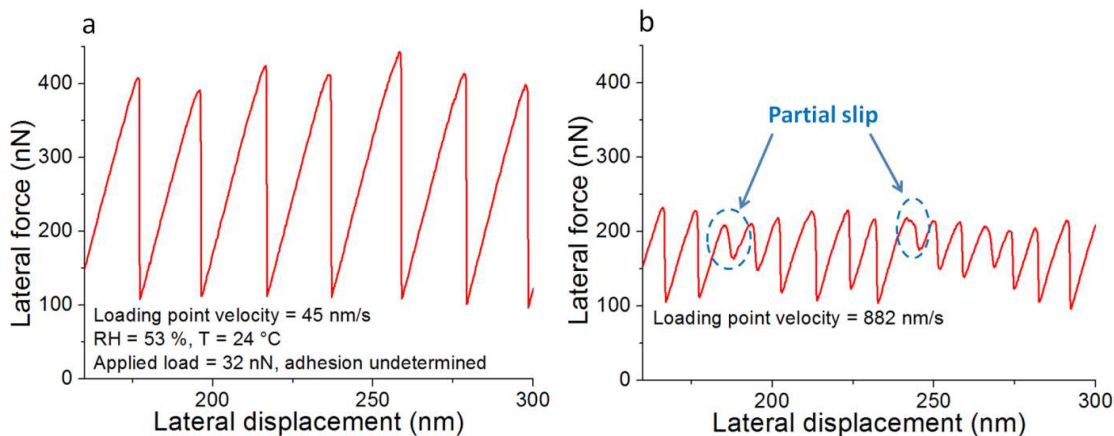


Fig. 5.5: Stick-slip in the quasi-periodic regime and the transition regime. (a) A representative lateral force vs. lateral displacement curve in the quasi-periodic stick-slip regime, well below the velocity at which the transition from stick-slip to steady sliding occurs. The stick-slip period and amplitude are highly regular. (b) A representative force vs. lateral displacement curve for the same tip under the same conditions, for which the sliding velocity is in the transition regime between stick-slip and steady sliding. The stick-slip events are less periodic than those in (a). Additionally, for some slip events, the lateral force only drops partially. Two representative partial-slip events are labeled in dashed blue ellipses.

5.4: Discussion of the dependence of single bond strength on loading point velocity

When we explained the logarithmic decrease of kinetic friction with velocity for ICBI friction at the nanoscale above, we assumed that the kinetic friction $f = f_0 N$, where N is the number of interfacial chemical bonds during sliding, and f_0 is the average bond strength for a single bond, which is independent of the loading point velocity v . However, this assumption of the independence of f_0 on v may not hold under some conditions. According to previous studies on the dependence of the breaking force on the loading point velocity for a single chemical bond or single asperity, the bond strength f_0 first increases with v logarithmically (more accurately speaking, the dependence is $(\log(v))^{2/3}$) and then reaches a plateau [89, 99, 100]. This logarithmic dependence for a single bond has also been incorporated into the multi-bond model of Urbakh, Schirmeisen and co-workers [101, 102], which describes friction due to the dynamics of interfacial bond formation and breaking. Therefore, if the dependence of the single bond strength on the velocity has already reached a plateau in our experiments, then there is no problem in assuming f_0 to be a constant. However, if the dependence of bond strength on velocity is still in the logarithmically increasing regime, then the kinetic friction f will be a quadratic function of $\log(v)$ since N is linear with $-\log(v)$. We comment that the resolution (*i.e.*, the number of data points) of our current experimental data in the regime of decreasing kinetic friction vs. velocity are not sufficient to distinguish whether the kinetic friction is decreasing with the log of velocity linearly, in a quadratic manner, or in some other fashion. The logarithmic dependence of friction on velocity is the simplest form to consider and agrees with the data well within experimental uncertainty and within the scatter of the data, so we report that kinetic friction decreases with the velocity logarithmically in the main text. The approximation of a logarithmic dependence in this manner has been made in prior studies [88-90].

5.5: Variations of surface chemistry with time and location

We find that frictional properties such as the ageing amplitude and the value of D_c can be different at different times and with the AFM tip in contact at different locations on the silica surface, even for the same tip under the same experimental conditions (such as RH, load, and adhesion force). We attribute this variation in behavior to the fact that piranha-cleaned silica is very chemically reactive and can readily adsorb contaminants and water [53, 54]. Such adsorbates will change the surface chemistry either by physisorbing on top of surface silanol groups, or possibly by reducing the number of surface silanol groups. Adsorbed water can also enable the adsorption of ions which will then be hydrated on the surface by the water. All of these processes will affect the frictional and adhesive properties of the contact. In our experience, if the time window in the experiments is too long (*i.e.*, longer than 10-20 mins) or if the tip is moved more than approximately 100 nm when seeking a new location for measurements, we frequently observe changes in certain frictional properties by factors of 3-4, such as the static friction for a given hold time. This effect contributes to some of the scatter and variation in the data presented in this thesis.

To further illustrate this, we show evidence of a change of surface chemistry with time in Fig. 5.6, where the static friction decreased by approximately 28% within 30 mins at the same nominal position.

We also show evidence of the spatial heterogeneity of surface chemistry on the substrate in Fig. 5.7, where the stick-slip amplitude and spatial period vary in the scan area in both fast and slow scan directions.

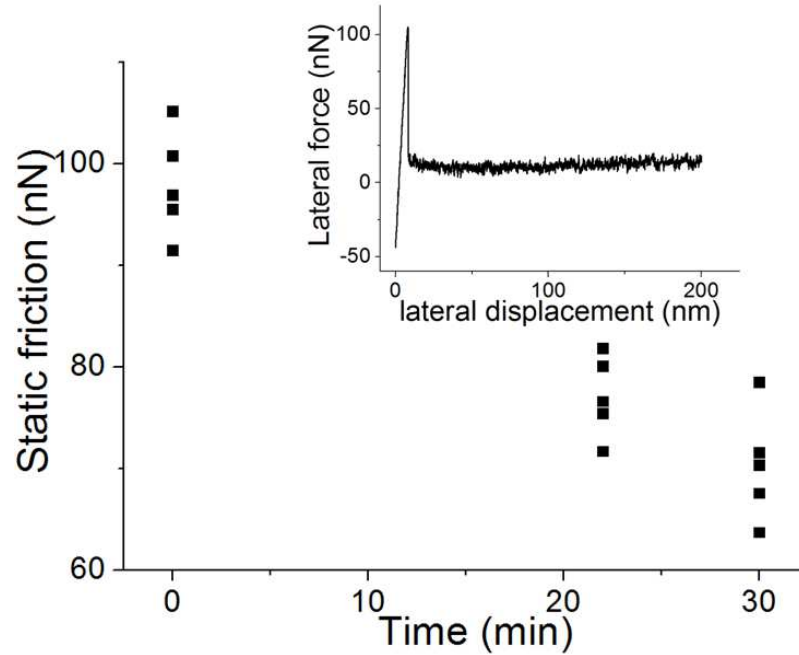


Fig. 5.6: Static friction vs. the time when static friction measurements are performed, measured for the same tip at the same nominal location on the sample. The hold time is 4.6 s for each static ageing test. $T = 24\text{ }^{\circ}\text{C}$, $\text{RH} = 52\%$, applied load = 26 nN, adhesion = 497 nN. The mean static friction forces are $98.0 \pm 5.2\text{ nN}$, $77.1 \pm 4.0\text{ nN}$, and $70.4 \pm 5.5\text{ nN}$ for times of 0 min, 22 min, and 30 min respectively. The static friction decreases about 28 % with 30 mins, attributed to the adsorption of contaminants on the substrate. Other SHS tests were performed between these three static ageing tests, so the tip was scanning on the substrate during a portion of the time intervals during these 30 mins. The substantial decay of static friction indicates that these scans are not sufficient to remove contaminants and prevent static friction from dropping significantly. The inset shows a typical lateral force vs. lateral displacement curve at time 0 min.

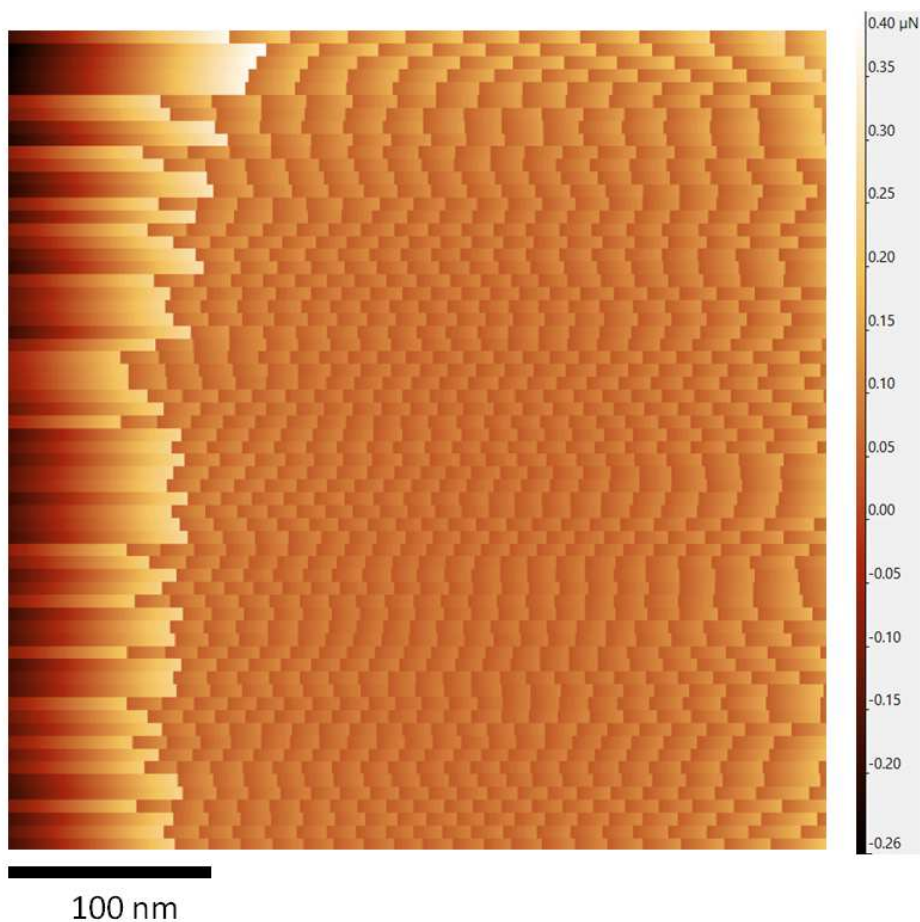


Fig. 5.7: Lateral force scan map showing stick-slip events. RH = 40 %, T = 24 °C, load = 130 nN, adhesion = 88 nN. The fast scan direction is from left to right, and the slow scan direction is from top to bottom. The scan size is 400 nm × 400 nm. The scan speed is 1000 nm/s. The heterogeneity of stick-slip amplitude and spatial period can easily be seen in both fast and slow scan directions.

Due to the above effects, we did not systematically study how the experimental conditions (such as RH and load) would affect D_c , since such experiments would usually require much longer times than the time window during which the surface chemistry does not change substantially. Instead, we choose a range of experimental conditions, and measured how kinetic friction depends on velocity. Our results (in Fig. 5.1

and 5.2) show that the logarithmically decreasing trend of friction with velocity, followed by a logarithmic increase with velocity, is consistent across this wide range of conditions. What varies are the absolute values of friction, the slopes of the friction vs. velocity trends in both regimes, and the transition velocity. The kinetic friction, the slope of the kinetic friction vs. log of velocity in the decreasing and increasing regimes, and the transition velocities range between 40 to 400 nN, 30 to 100 nN/decade, 50 to 100 nN/decade, and 1 to 100 nm/s, respectively, under the conditions tested. Therefore, although the conditions in our experiments spanned a wide range due to the time- and location-dependent chemistry of the sample, the logarithmic trends and the order of magnitude of values of kinetic friction, slopes, and the transition velocity (10-1000 nN for kinetic friction; 10-100 nN/decade for slopes; 1-100 nm/s for transition velocity) are reproducible.

5.6: Summary

In conclusion, for nanoscale silica-silica single asperity contacts, kinetic friction first decreases with sliding velocity logarithmically, and then increases with velocity logarithmically. We provide a physically-based model for the velocity-weakening regime observed in our experiments by assuming the conservation of the number of interfacial bonds during sliding and the formation of siloxane bonds from dangling bonds. This helps further establish a physically-based RSF friction law (uncovering the aspect of memory distance and further demonstrating the direct effect) for nanoscale contacts with reactive bonding mechanisms, and suggests a mechanism that may be active in "macroscale" frictional sliding of multi-asperity interfaces. Such contacts are far more complex than the single-asperity contacts studied here, but they nonetheless necessarily include nanoscale asperity contacts along with microscopic ones. Models of such interfaces may benefit from considering the frictional behavior and the corresponding model presented here.

Chapter 6: Stick-Slip Instabilities for Interfacial Chemical Bond-Induced Friction at the Nanoscale

Earthquakes are generally thought to be caused by the unstable stick-slip motion of rocks at faults. This stick-slip phenomenon, along with other frictional properties of materials (including rocks) at the macroscale, can be described well by the empirical rate and state friction (RSF) laws. Here we show stick-slip behavior for nanoscale single-asperity amorphous silica-silica contacts. The stick-slip behavior is quasi-periodic, and both the amplitude and spatial period of stick-slip increase with the normal load and decrease with the loading-point velocity. The peak force for each slip increases with the temporal period logarithmically, which results from a combination of the evolution effect, the direct effect, and the effect of non-zero, varying shear forces, and can be better understood using PTTE model discussed in Chapter 4. We also find that the peak force decreases with velocity logarithmically, consistent with macroscale contacts. We find that the minimum force for each slip is independent of the velocity. The temporal period scales with the velocity in a nearly power law fashion, with the exponent always between -1 and -2, similar to macroscale behavior. In addition, with increasing velocity, the stick-slip behavior eventually transitions into steady sliding (the partial slip phenomenon in the transition regime is demonstrated and discussed in Chapter 6, corroborating our explanations of the memory distance). These results contribute to a physical picture of the ICBI stick-slip, and further established RSF laws at the nanoscale.

6.1: Experimental results of interfacial chemical bond-induced stick-slip friction at the nanoscale

In Fig. 6.1 and Fig. 6.2, quasi-periodic stick-slip behavior is shown. Note that the slip distance ranges from *ca.* 10-100 nm, demonstrating that this is clearly not an atomic lattice stick-slip effect, as reported in previous AFM experiments on crystals [90, 103]. The peak force, the peak-to-trough amplitude, and the spatial period (in distance) of stick-slip increase with normal load and decrease with the loading point velocity. However, while the lowest force in each slip event increases with load, it is nearly independent of the loading point velocity, as most clearly seen in the topmost plot in Fig. 6.2. In addition, from Fig. 6.2, the stick-slip behavior transitions into steady sliding at higher velocities. As well, the slope

of the lateral force vs. lateral displacement curve during the stick phase (*i.e.*, the total lateral stiffness of the system, also called the "effective stiffness") is almost independent of load or velocity, most clearly seen in Fig. 6.1 and in the topmost plot in Fig. 6.2.

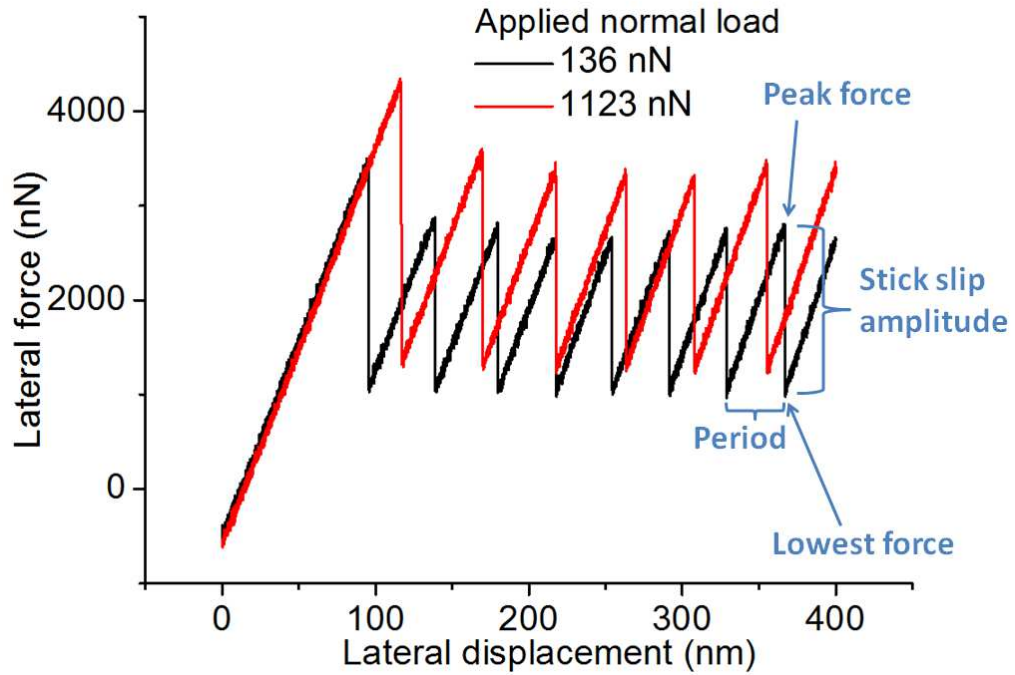


Fig. 6.1: Lateral force vs. lateral displacement under two loads. The loading point velocity is 95 nm/s, $T = 24\text{ }^{\circ}\text{C}$, $\text{RH} = 80\text{ }%$, hold time = 0.1 s, the adhesion is undetermined (at least 976 nN). The measurements of the peak force, lowest force and stick-slip amplitude are shown. It could be seen that the stick-slip is quasi-periodic, and the stick-slip amplitude and spatial period increase with load.

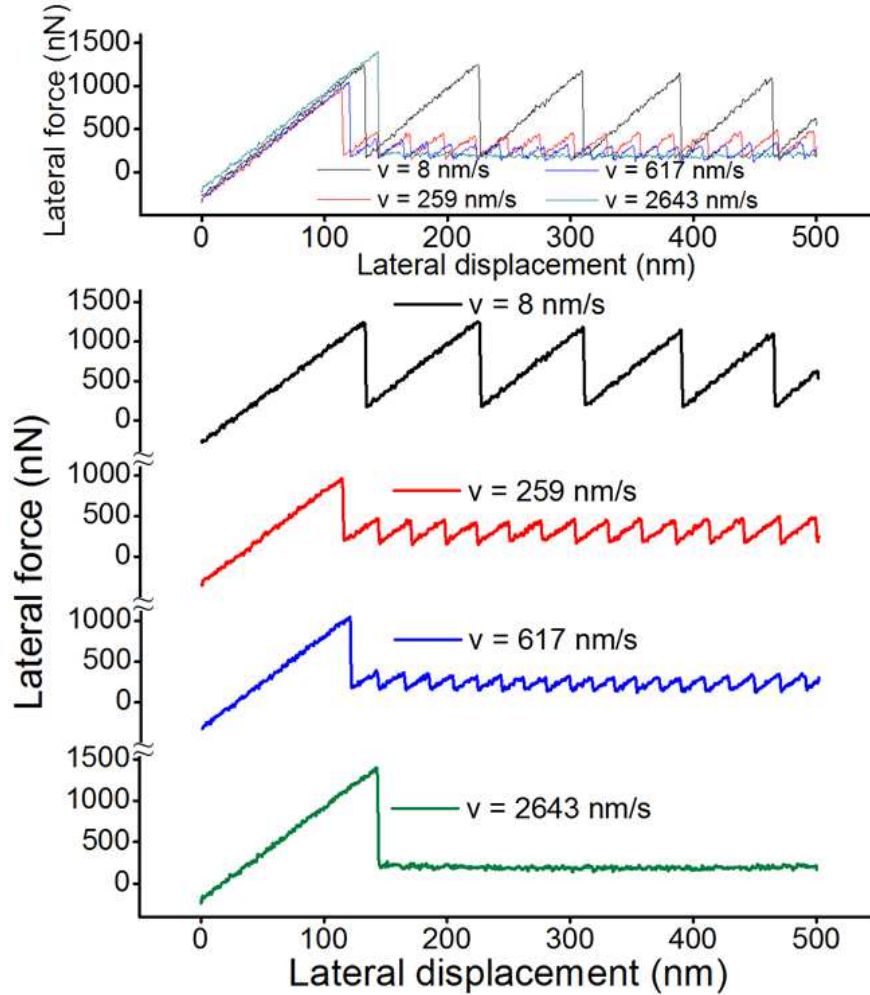


Fig. 6.2: Lateral force vs. lateral displacement for different loading point velocity. $T = 24\text{ }^{\circ}\text{C}$, $\text{RH} = 42\%$, hold time = 0.1 s, applied normal load = 65 nN, the adhesion is undetermined. The stick-slip amplitude and spatial period decreases with the loading point velocity, and the stick-slip transitions to smooth sliding when the velocity is large enough. The velocity is varied randomly to exclude systematic errors.

In Fig. 6.3(a), the peak force in each stick-slip event increases with the temporal period (in time). In Fig. 6.3(b), the peak force first decreases with velocity logarithmically, and then levels off, before the

stick-slip transitions into steady sliding. In Fig. 6.3(c), the temporal period and velocity follow power law scaling. The exponent of the power law scaling is -1.41 ± 0.02 .

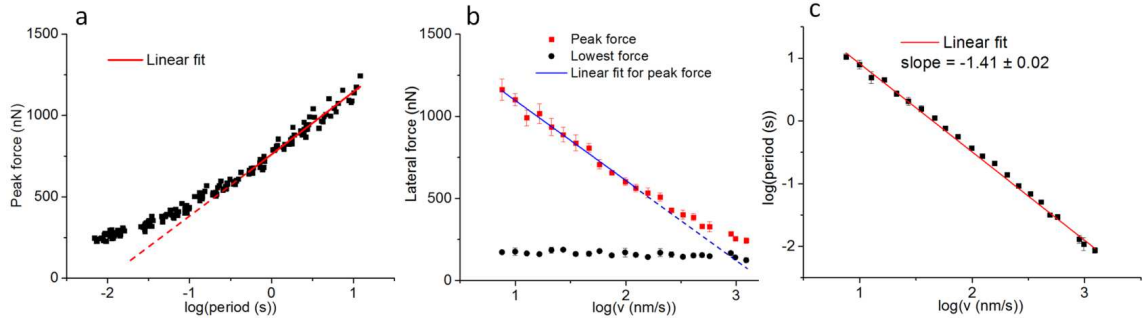


Fig. 6.3: stick-slip behavior under varying loading point velocities. The tip and conditions are the same as that in Fig. 6.2. (a) Peak force vs. log of temporal period. With decreasing period, the peak force decreases with log of period linearly, and deviates from this dependence below a period between 0.1 s and 1 s. (b) Dependence of peak force and lowest force on loading point velocity. The peak force first decreases with velocity logarithmically, and then levels off, while the lowest force is nearly independent of velocity. (c) Power law scaling of the temporal period with velocity, with an exponent of -1.41 ± 0.02 . The velocities are varied randomly to exclude systematic errors.

Another set of stick-slip results from another tip under different conditions than that in Fig. 6.3 is shown in Fig. 6.4. The results are very similar to the data shown in Fig. 6.3, demonstrating the reproducibility of the findings.

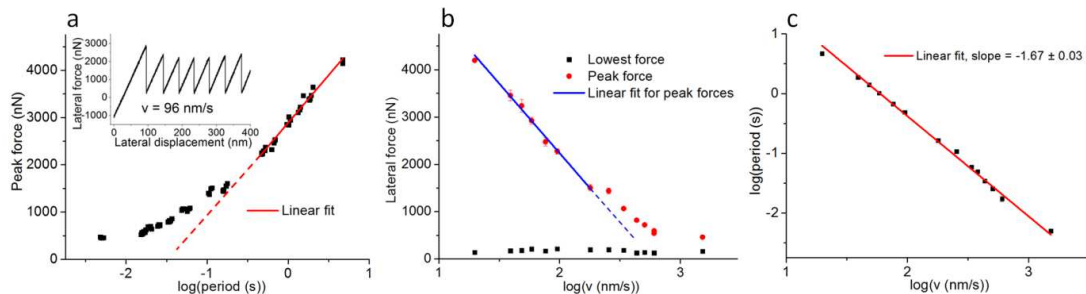


Fig. 6.4: Another set of data on stick-slip behavior under varying loading point velocities. $T = 24\text{ }^{\circ}\text{C}$, $\text{RH} = 80\%$, applied load = 819 nN, and the adhesion is undetermined (due to being too large to measure; it was at least 834 nN). (a) Peak force vs. log of period (in time). With decreasing period, the peak force decreases with log of period linearly, and begins to deviate below a period between 0.1 s and 1 s, consistent with the data in Fig. 6.3. The inset shows a typical quasi-periodic stick-slip result. (b) Dependence of peak force and lowest force on loading point velocity. The peak force first decreases with velocity logarithmically, and then begins to level off, while the lowest force is nearly independent of velocity. This is consistent with the data in Fig 6.3. (c) Power law scaling of the period and velocity, with an exponent of -1.67 ± 0.03 . The velocities are varied randomly to exclude systematic errors.

Four additional sets of results showing the power law scaling of the stick-slip period with loading point velocity are shown in Fig. 6.5. The relative humidity (RH), temperature, applied load, and adhesion force (if determined) are provided in the legend of each plot. Adhesion was undetermined in certain cases as it was too large to be measured. The value was at least 194 nN and 578 nN for b and c respectively.

The power law exponents are -1.49, -1.45, -1.13, and -1.56 for a, b, c, and d respectively. In sum, the power law exponents from all six tests (four from Fig. 6.5, one from Fig 6.3, and one from Fig. 6.4) are between -1 to -2.

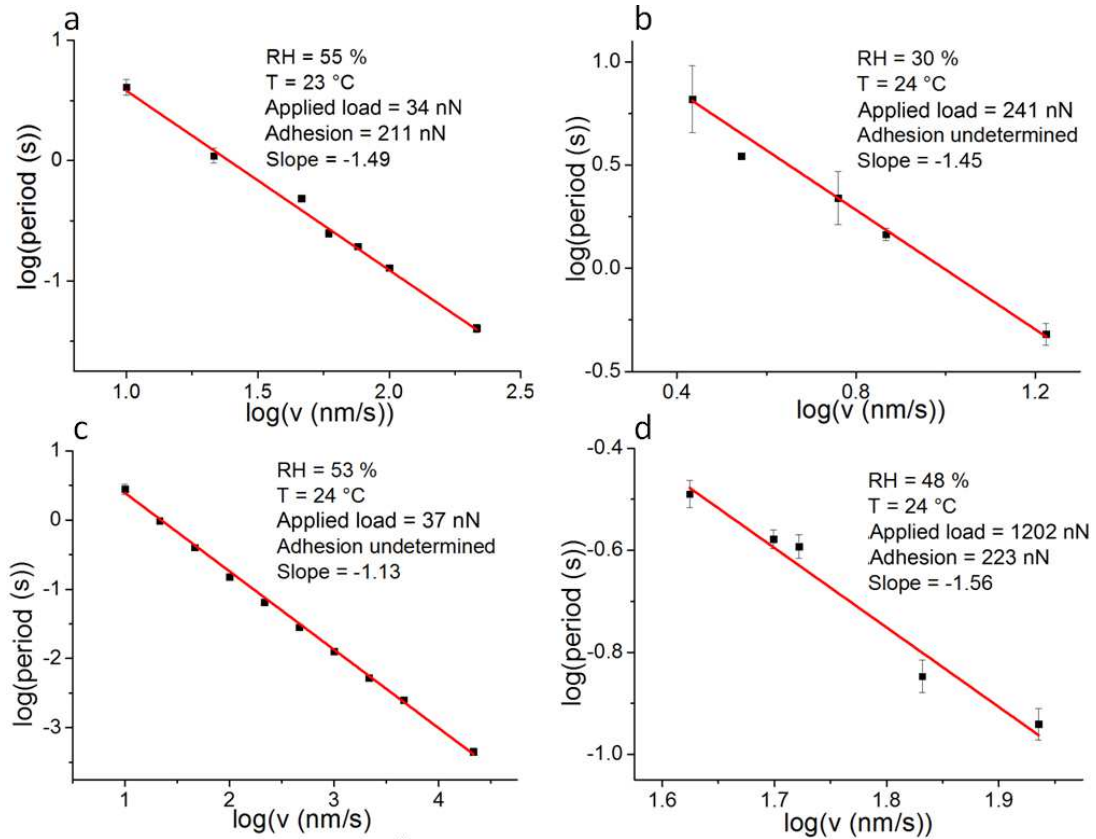


Fig. 6.5: Power law scaling of stick-slip period and velocity.

6.2: Discussions on the experimental results

We now provide a heuristic model in Fig. 6.6 to describe and explain the stick-slip behavior we observe, modified from the schematic in Fig. 4.12 of [3] (which is based on Fig. 3 of [104]), which describes stick-slip behavior for macroscopic contacts for the case where static friction increases with time. The time dependence of the static friction force and the spring force (*i.e.*, the restoring force due to the deformation of the system) for different velocities and loads are shown and compared in Fig. 6.6(a) and (b) respectively. According to several studies of silica-silica nanoscale friction [1, 41, 49], static friction increases logarithmically with time above *ca.* 0.1 s, so it is represented as a logarithmic function of time on

this plot. The spring force increases with time linearly since the loading point velocity is constant. The slope of the spring force vs. time is the total stiffness of the system divided by the loading point velocity. The tip sticks as long as the spring force is less than the static friction force, and slips when the spring force reaches the static friction force. This is the point where the peak lateral force is reached. In this schematic, the force at which the tip comes to rest when slipping ends is set at an arbitrary value, and it is arbitrarily set to be independent of sliding velocity, which is consistent with our experimental results. Once slip stops, the spring reloads and the cycle repeats, producing repeating stick-slip events. Note that when slip stops, this plot is constructed such that the time axis is reset back to zero for the beginning of the second and subsequent stick phases. This heuristic model does not attempt to explain what determines the magnitude of the force when slip stops, since as specified above, its value is simply assumed to be constant. However, independent of this characteristic, the model demonstrates how a logarithmic dependence of static friction on sticking time in concert with finite system stiffness leads to quasi-periodic stick slip. It also shows why the peak force, the force at which slip occurs, decreases with velocity – there is less time for static friction to increase during the sticking phase. It also shows why the very first slip event initiates at a somewhat higher force than subsequent slips, as seen in Fig. 6.1 and 6.2. Additional details are given in the caption to Fig. 6.6.

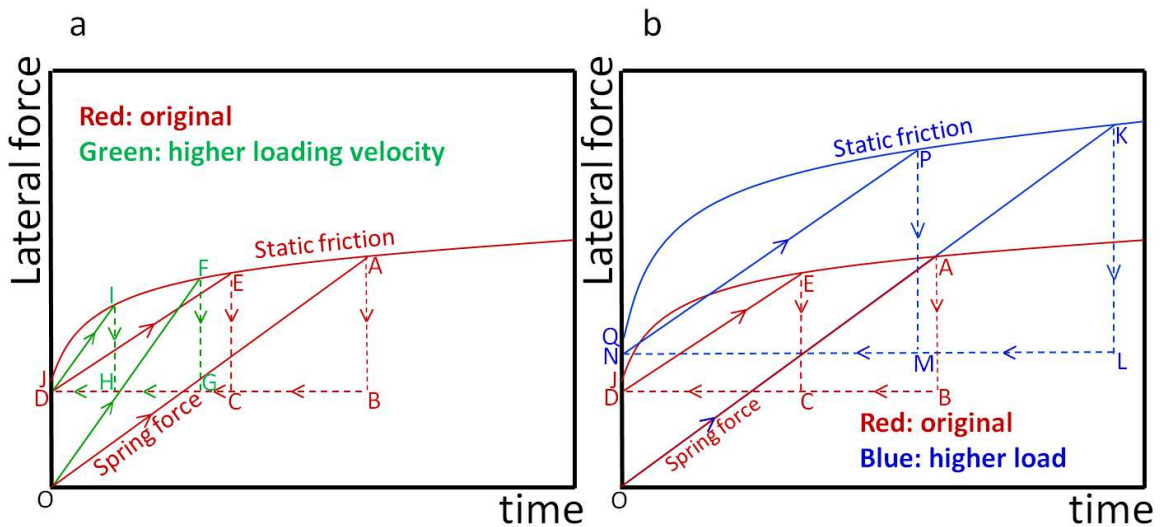


Fig. 6.6: Schematic of the velocity (a) and load (b) dependence of stick-slip. The vertical axis is lateral force, *i.e.*, either the static friction at the interface (the force required to initiate slip), or the force in the spring (due to its elongation). The horizontal axis is time. For both (a) and (b), the labeled solid red curves show how the static friction and the spring force evolve with time, for a given loading point velocity, under a given load. For simplicity, the initial spring force is set to 0. The curve along points JEA represents how static friction increases with time. The line segment OA shows how the spring force increases with time, with the slope proportional to the effective stiffness. At point A, the spring force reaches the static friction force, the tip slips and the spring force drops, following the dashed red line from A to B. Since slips are usually extremely fast in AFM, segment AB is drawn as a vertical line. The horizontal segment BD represents the resetting of the time axis so that the system starts the next cycle at point D, with the spring force maintained at the value at the end of the last slip event (point B). Segment DE represents the second stick. When the spring force reaches the static friction force this time (point E), slip again occurs and the spring force drops from E to C. Point C is chosen to lie on segment BD, since the lowest forces in each slip event are assumed to be the same, based on our experimental results (Figs. 6.2 and 6.3(b)). The starting spring force of the third stick is the same as the second stick (*i.e.*, also at point D). Therefore, subsequent stick-slips will repeat regularly, producing the regular periodicity observed in experiments. The length of AB is larger than EC, thus, the observation that the peak force of the first stick is larger than the peak forces of the subsequent sticks is explained by this model. (a) The green curves show the spring force for a higher loading point velocity than that for the red curves (the static friction force vs. time remains the same, *i.e.* the curve lying along points JEA). Since the velocity is higher than in the case of the red curves, the slope of the spring force vs. time (segment OF) is greater, but the evolution of static friction with time is unaffected. Therefore, the system reaches the point of slip at an earlier time and a lower static friction force. This explains the experimental observation that the greater the loading point velocity, the smaller the static friction force. Since the effective stiffness is independent of velocity (Fig. 6.2), the spatial period of stick-slip is thus smaller at higher velocity (*i.e.* the time elapsed for segment OF is smaller than for OA, and likewise is smaller for DI than for DE). Slip then occurs at point F, and the cycle repeats as described for

the red curve (segments DIH). (b) The labeled blue curves show the evolution of the static friction (lying along points QPK) and spring force (segments OK and NP) under a higher load. Here we assume that increasing the load magnifies the static friction values by a multiplicative factor, consistent with experimental observations [1]. Since the effective stiffness is independent of load (Fig. 6.1), the segment representing the spring force during the sticking phase for both loads, OK and OA, must overlap. Since the stick-slip amplitude and spatial period are larger for higher load according to Fig. 6.1, the length of PM is larger than EC, and MN larger than CD. Slip then occurs, and the cycle repeats as described for the red curve.

For the load dependence of stick-slip (Fig. 6.1), higher load should result in larger contact area [1], thus increase the lateral contact stiffness k_{con} [105]. The effective stiffness k_{eff} (*i.e.*, the slope of lateral force vs. lateral displacement) satisfies $\frac{1}{k_{eff}} = \frac{1}{k_{con}} + \frac{1}{k_{cant}} + \frac{1}{k_{apex}}$, where k_{cant} is the stiffness due to the lateral bending and torsion of the cantilever, and k_{apex} is the stiffness due to the deformation of the tip apex. However, in our experimental results, k_{eff} does not change with load. Since k_{cant} and k_{apex} should be independent of load, we conclude that $\frac{1}{k_{cant}} + \frac{1}{k_{apex}} \gg \frac{1}{k_{con}}$ for our system. In other words, the cantilever and the apex together are much more compliant than the contact.

For the dependence of the peak force on temporal period (Fig. 6.3 (a)), we find that the increasing trend (*i.e.*, the logarithmic dependence of peak force on time in the longer time regime, and the deviation from logarithmic below a transition time which is somewhere between 0.1 and 1 s) is identical to the behavior observed in static ageing tests where instead of period, the horizontal axis is the hold time; in both cases, time represents the time of static contact [1, 41, 49]. However, unlike in stick-slip tests, for static ageing tests the loading point velocity is constant. This agreement is interesting for multiple reasons. First, an influence of the direct effect should be manifested if the loading point velocity is varied, as discussed in Chapter 4. In the present stick-slip experiments, different periods correspond to different velocities (as

shown in Fig. 6.3 (c)) and thus should involve different magnitudes of the direct effect. In static ageing tests, we have observed logarithmic increasing of static friction with loading point velocity for a given hold time (see Fig. 4.3 in Chapter 4). However, the trend observed in Fig. 6.3(a) is the opposite: static friction is higher at lower loading point velocities. Thus, the evolution effect occurring during each stick phase likely dominates over any influence of the direct effect. In addition, during each sticking phase, the lateral force increases with time (or equivalently, lateral displacement), whereas in static ageing tests in the AFM, during a hold, the lateral force is fixed (within the limits of drift of the AFM). The progressive increase in shear stress during sticking due to the relentless shear loading of the interface may affect the interfacial chemical bond formation process. In fact, the effect of shear on ageing has been observed in macroscopic experiments [6]. However, according to Fig. 6.3 (a), neither the direct effect nor the presence of an increasing shear stress is sufficient to prevent an increasing trend of peak force vs. $\log(\text{time})$, the same trend seen in static ageing tests. We note that in static ageing tests, no variation of the direct effect is expected since the loading point velocity is constant. The effect of changing shear stress can be ignored when the velocity and/or the hold time are chosen to be large enough that the time span of the lateral loading is much smaller than the hold time, as discussed in Chapter 3. Thus, these data put a limit on the magnitude of the direct effect in the presence of increasing shear stress at the interface. Further understanding of the influence of lateral loading rate and shear stress on the time dependence of friction is beyond the scope of this paper and requires additional studies.

The power law scaling of temporal period and velocity we observed (Fig. 6.3(c)) resembles that in macroscopic experiments [44], and is qualitatively consistent with Omori's law in seismology (*i.e.*, the frequency of aftershocks decreases inversely with time after the main shock) [44, 106]. In macroscale rock friction studies, this power law scaling is reproduced in numerical simulations based on conventional RSF laws [44]. However, since conventional RSF laws are empirical, this power law scaling still lacks a physical explanation. Why our nanoscale contacts also have this scaling, why the exponents of the power are always between -1 and -2, and the physics underlying this power law scaling require further study.

The logarithmic decrease of the peak force with loading point velocity (Fig. 6.3 (b)) also resembles that seen in macroscopic experiments of rock friction [44, 107], and is opposite to the logarithmically increasing trend seen in atomic stick-slip experiments on crystalline substrates for all but the highest velocities where the benefits to slip from thermal energy are no longer available [88-90, 99].

The levelling off of the peak force vs. log of velocity for higher velocities just before stick-slip behavior transitions into steady sliding (Fig. 6.3(b), above $\log(v) \sim 2.6$) is quite different than the sudden drop-off of peak force vs. log of velocity seen near the transition to smooth sliding in macroscopic steel-on-steel friction experiments [104], and in surface force apparatus experiments on thin molecular films between mica surfaces [108]. The levelling off observed in Fig. 6.3(b) is consistent with the levelling off in the small-time regime in Fig. 6.3(a), and the straight line of the power law scaling in Fig. 6.3(c), since the power law scaling of temporal period and velocity in Fig. 6.3(c) means that log of the period is linear with the log of the loading point velocity.

In Chapter 4 we reported a physically-based model for ICBI friction for nanoscale single-asperity contacts. Our model incorporates the evolution effect (*i.e.*, the ageing) into the Prandtl-Tomlinson with temperature (PTT) model [88, 89], which is one well-established physically-based model to describe atomic stick-slip behavior. In this model, it is the velocity of loading point rather than the tip (as it would be if analogous to conventional RSF laws) which determines the direct effect. Also, the direct effect and the evolution effect are not linearly combined, quite different than that in conventional RSF laws. We hope future theoretical and numerical studies based on PTTE model could reproduce and thus explain the stick-slip properties we observed in this work in a fundamental sense.

6.3: Summary

We measure friction between a silica tip and a hydroxylated silica surface. While the tip sticks, siloxane bonds form at the interface, leading to interesting interfacial dynamics and instabilities. We find

that stick-slip is quasi-periodic at the scale of several to tens of nanometers. Both the peak force and the spatial period of the stick-slip increase with the normal load and decrease with the loading point velocity. The peak force for each slip increases with the temporal period logarithmically, consistent with the logarithmic ageing with time seen in static ageing tests, implying that the stick-slip is induced by interfacial siloxane bond formation. Further, it indicates that the direct effect and the effect of increasing shear stress together have no influence on the logarithmically increasing trend in friction. Also, although the peak force decreases with velocity logarithmically, the minimum force for each slip is independent of velocity, which results from the dynamics of the tip and dissipation during slip that are not yet understood. The temporal period scales with velocity in a power law fashion, with the exponent always between -1 and -2. An understanding of the origins of this relation may be developed in the future via atomistic and numerical simulations. In addition, we observe that with increasing loading point velocity, stick-slip behavior eventually transitions into smooth sliding. In the transition regime between stick-slip and smooth sliding, for some slip events, the lateral force only drops partially, consistent with the physical picture of dangling bonds forming new bonds during slip. Finally, we provide a model to describe stick-slip, which illustrates how the competition of the dynamics of static friction (*i.e.*, the evolution effect) and spring force result in the stick-slip behaviors observed in the experiments. These results reveal different aspects of ICBI stick-slip, provide data that can guide and constrain future physically-based RSF models, and further elucidate rate and state behavior at the nanoscale.

Chapter 7: Concluding Remarks and Outlook

The contents of this thesis are results of the work I performed during my Ph.D. studies. Some of this work has already been published in a peer-reviewed journal [1]. The other contributions are now either close to submission or under review, as listed in Chapter 1. In this chapter, I will first summarize the work I have completed, namely, on the load and time dependence of ageing (Chapter 3; further demonstrating the evolution effect, and studying the effect of load), on developing a physically-based RSF law (Chapter 4; studying the direct effect in static friction, and exploring how the direct effect and evolution effect combine), on the friction memory distance (Chapter 5; demonstrating the memory effect in nanoscale contacts, and discussing the connection between the direct effect and evolution effect), and on nanoscale stick-slip instabilities (Chapter 6; showing the competition and synergy of the evolution effect, the direct effect, the effect of shear, and the system dynamics). These four interconnected studies further establish the ICBI friction mechanism for nanoscale silica-silica contacts and physically-based RSF laws at the nanoscale. The main connections between these studies include the following:

- The constant loading point velocity in our study of load and time dependence of ageing, presented in Chapter 3, enforces a constant direct effect (related to the physically-based RSF law we established);
- Kinetic friction is connected to static ageing through the memory distance; our development of a physically-based RSF law uses the result from our work that kinetic friction increases with velocity in the large velocity regime, where ageing is suppressed during sliding, as shown in Section 5.1;
- The phenomenon of partial slip in the transition regime between stick-slip and smooth sliding corroborates our model of the memory distance, which assumes that during sliding, after an interfacial chemical bond breaks, it remains in a high-energy state as a dangling bond which can readily form new bonds with other dangling bonds;

- The physically-based RSF law we establish (the PTTE model) helps in understanding our stick-slip results, such as the logarithmic increase of peak force with temporal period of stick-slip.

Following the summary of this work, open questions and future work will be discussed. Finally, I will discuss open questions and future work for other aspects of this project on rate and state friction at the nanoscale.

7.1: Load and time dependence of interfacial chemical bond-induced ageing at the nanoscale

The AFM experimental results presented in this thesis show that ageing is approximately proportional to the load multiplied by the contact time (Section 3.3.3, Eq. 3.9). In section 3.3, we present a physically-based model which explains the experimental findings well, based on previous theoretical studies of ICBI ageing [41]. Our experimental work corroborates these theoretical studies, and also establishes the first contact mechanics model to describe single-asperity contacts that exhibit ageing behavior.

A primary concern about this aspect of our work is that the time constant τ_0 we extracted from experimental ageing results using the model we constructed is far greater than expected. As discussed in Section 3.4, we hypothesize that this discrepancy is due to relying on a previous theoretical model for determining τ_0 from our experimental data; the model, which describes the time dependence of ageing [41], assumes that the initial distribution of reaction energy barriers is uniform, and there are no interactions between neighboring reaction sites. If more advanced analytical models of the time dependence of ageing which take account of various energy barrier distributions and interactions between neighboring sites are developed, we expect that the value of the time constant we extracted may be reasonable. If analytical derivations prove intractable, numerical simulations (MD, DFT, and kMC) could be conducted for the load and time dependence of ageing. The simulation results could be compared to our experimental results and we expect that some physically reasonable parameters could be extracted. Our collaborator (Prof. Izabela

Szulufarska) is currently working on this kind of simulation. In addition, uncovering ageing behavior at small time scales may help to extract reasonable values of τ_0 from the experimental data if analytical models of ageing vs. time at small time could be established. This is because at small time scales, only a small amount of siloxane bonds form, and thus the interactions between neighboring sites could be ignored as an approximation. Therefore, the limitation resulting from having to model interactions between neighboring bonding sites could be circumvented.

7.2: A physically-based rate and state friction law for interfacial chemical bond-induced friction at the nanoscale

As Presented in Chapter 4, we successfully incorporated the evolution effect into the well-established Prandtl-Tomlinson with temperature (PTT) model, which is a fundamental theory to describe atomic stick-slip for crystalline substrates. We call our new model the Prandtl-Tomlinson with temperature and evolution effect (PTTE) model, which could be seen as a physically-based RSF law for ICBI friction at the nanoscale. According to our PTTE model, the velocity determining the direct effect is the loading point velocity, rather than tip velocity as in conventional RSF laws. Also, in the PTTE model, the evolution effect and direct effect are not necessarily linearly combined, which contrasts with conventional RSF laws. We also provide experimental findings which corroborate the PTTE model including the logarithmic increase of static friction and kinetic friction with loading point velocity, and the difference between the rates of those two quantities. Our work also extends the PTT model to amorphous substrates.

Although the PTTE model and its experimental corroboration represent progress towards the goal of establishing fundamental RSF theories for ICBI friction at the nanoscale, and for understanding the physical origin of conventional macroscale RSF laws, the model still has a limitation: the effect of the shear force on ageing during the sticking regime (*i.e.*, the process of jumping over the barrier, whereby the applied lateral force is progressively increasing) must be relatively small compared to the magnitude of

ageing during holding in static ageing tests, where there is no shear force deliberately applied. This is because the PTT model assumes that the intrinsic energy barrier should be constant during the jumping process. This condition is satisfied in our experiments, because the hold time and the loading point velocities were chosen to be large enough that the sticking time is small. However, in cases where the sticking time is large, such as most stick-slip tests, our PTTE model might not be applicable. Models and theories which consider the effect of shear on ageing are needed for these cases. In order for these new theories to be established, AFM experimental studies of the shear effect on ageing are necessary in the future.

Another limitation of our work on the PTTE model is that we have not reached the plateau regime for the dependence of friction on velocity which is predicted for higher velocities. Without experimental data in the transition regime, it is impossible to extract important parameters (such as the saturation force and characteristic vibration frequency) in the PTT and PTTE models. The highest velocity in our work is at the limit of the piezoelectric scanner in the scan head and the control system of the RHK AFM we are using. Future experiments could explore the higher velocity regime by shearing a modified sample holder (which can provide much larger velocities than the piezoelectric scanner in the scan head of RHK AFM) as was accomplished by a previous Ph.D. student Xin-Zhou Liu from our group [90].

7.3: Kinetic friction and memory distance for interfacial chemical bond-induced friction at the nanoscale

In Section 5.1, we reported the observations that kinetic friction first decreases and then increases logarithmically with sliding velocity (which is the same as the loading point velocity in smooth sliding tests) in our experiments. We propose a fundamental explanation for the logarithmically decreasing regime of friction vs. velocity, which involves the concept of a memory distance. As illustrated in Fig. 5.4, our explanation contains two key points. One is the immediate reformation of a dangling bond with other

dangling bonds on the opposing surface after the original interfacial siloxane bond breaks during smooth sliding of the tip; the memory distance represents the average sliding distance before an active reaction site on the tip becomes passivated by, for example, -OH groups or substrate contamination. The second point is the conservation of interfacial bonds during smooth sliding. The first point is corroborated by our experimental finding that, in the transition regime between regular stick-slip and smooth sliding, the lateral force sometimes only drops partially. The second point is a reasonable assumption, but lacks direct experimental confirmation. Therefore, our explanation is partially corroborated by experiments.

Our explanation of the memory distance and the logarithmic decrease of kinetic friction with velocity is the first physically-based explanation ever proposed for ICBI (especially covalent bond-induced) friction nanoscale contacts, and may aid in the understanding of the memory distance in conventional RSF laws.

At present, this physically-based explanation is just a qualitative model. Future studies might establish a more quantitative model allowing for more rigorous experimental tests. Also, numerical simulations (including MD, DFT or kMC) should be performed to enhance and further corroborate these models.

One possible way to experimentally test our model of memory distance D_c is to measure D_c (by measuring the transition velocity of kinetic friction vs. velocity and the transition time of static friction vs. contact time and multiplying these two quantities together) at a given spot many times. On one hand, the substrate will absorb more and more contaminants with time. On the other hand, with more contamination, the density of surface -OH groups will be reduced. According to our model, both -OH groups and contaminants may passivate the reaction site. Thus, we expect that there might be some competition between the two factors. If in the experiments we consistently observe that D_c becomes smaller with time at a given spot, that would suggest that contamination is the dominant factor of passivation. If D_c becomes larger with time, then that would imply that surface -OH groups are the dominant element in passivation.

We also comment that direct measurement of interfacial chemical bonding for a nanoscale contact is very difficult, and no instrument can achieve this goal at the present. For example, spectroscopic methods like X-ray photoelectron spectroscopy (XPS) cannot analyse nanoscale contacts [109]. There are a handful of methods for obtaining a spectroscopic signature at a nanoscale interface, such as tip-enhanced Raman spectroscopy [110, 111], but the signal strength is weak and would be extremely difficult to differentiate from the background, as we would be looking for a small increase in Si-O-Si bonds between two silica surfaces. One possible method to better control the surface chemistry of silica (to have less contamination) is to perform experiments in liquid. In this way, the pH of the solution could be monitored and varied, which could affect the siloxane bonding but not creep [112]. This would provide more evidence for the chemical bonding mechanism.

7.4: Stick-slip instabilities for interfacial chemical bond-induced friction at the nanoscale

In Chapter 6, we find that stick-slip is quasi-periodic at the scale of several to tens of nanometers. Both the peak force and the spatial period of the stick-slip increase with normal load and decrease with loading point velocity. The peak force for each slip increases with the temporal period logarithmically, consistent with the logarithmic ageing with time seen in static ageing tests, implying that the stick-slip behavior is induced by interfacial siloxane bond formation. The temporal period scales with velocity in a power law manner, with an exponent between -1 and -2. Further understanding of the physics of this relation may be developed in the future with atomistic and numerical simulations. In addition, we provide a model to describe stick-slip, which illustrates how the competition of the dynamics of static friction (*i.e.*, the evolution effect) and spring force result in the stick-slip behavior observed in the experiments.

More work is needed to fully explain results such as the power law scaling of temporal period and loading point velocity. We expect that all these results could be reproduced and physically explained after

physically-based RSF laws that consider shear effects on ageing are established, and once atomistic and numerical simulations are performed based on these RSF laws.

7.5: Outlook

Besides the future work mentioned in the above sections, I discuss other directions for future work below.

The first direction is the study of friction behavior during velocity-stepping (VS) tests. In conventional rock friction studies, VS tests are important for measuring the direct and evolution effects, and the memory distance (the decaying distance of lateral force after the stepping of loading point velocity) [6]. Since the physically-based RSF law we established (*i.e.*, the PTTE model) is very different than conventional RSF laws, and the physical meaning of the memory distance for ICBI friction at the nanoscale is also different than that at the macroscale, we expect that VS tests for ICBI friction at the nanoscale will show different behaviors than macroscale VS tests. Relevant experiments are ongoing.

Another direction is to study ageing at small time scales. According to previous simulation studies [41] (see Fig. 1.15), with decreasing hold time, the dependence of static ageing amplitude on time will deviate from logarithmic and begin to level-off below *ca.* 0.1 s. Ongoing experimental work shows that this is indeed the case in experiments (see Fig. 5.3). We find that the transition time where the dependence deviates from logarithmic is always between 0.1 s and 1 s under various conditions in our experiments. In addition, we find that ageing is approximately linear with contact time below 0.1 s, as shown in Fig. 7.1. Simulation studies (conducted by our collaborators Prof. Izabela Szlufarska and Dr. Yun Liu) and analytical studies (by us) are now ongoing in hopes of explaining this linear ageing behavior.

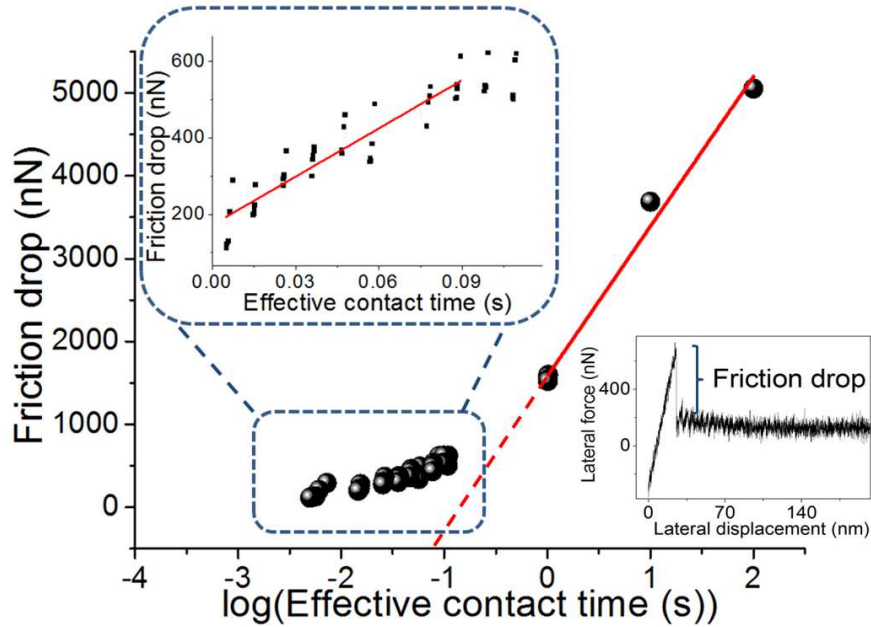


Fig. 7.1: Friction drop vs. effective contact time. Relative humidity (RH) = 80 %, applied normal load = 332 nN, adhesion undetermined (at least 976 nN), temperature $T = 24$ °C and the loading point velocity is $1.53 \mu\text{m/s}$. The upper left inset shows the data points from *ca.* 5 ms to 0.11 s, with a linear time scale. The friction drop increases linearly with effective contact time from *ca.* 5 ms to 0.09 s. The linear fit is the red solid line in the inset. Data points for contact times of 1 s, 10 s, and 100 s fall nicely on a linear fit, which is the red solid line in the main plot extended by the red dashed line. The data points for a contact time of 0.1 s are clearly above this red dash line. We thus estimate that the transition time where the logarithmic dependence of ageing on time ends is between 0.1 s and 1 s. The lower right inset shows one lateral force vs. lateral displacement curve for a 0.07 s hold time. The hold times are varied randomly to exclude systematic errors.

Also, according to previous simulations [41], ICBI ageing at the nanoscale should saturate for longer contact times. Experimental investigations of this saturation at long contact time are needed. The challenge in performing such measurements is that it requires holding the tip steady without changes in the

normal or lateral force over long periods of time (at least 1000 s), where the effects of drift become important; this issue can perhaps be addressed with drift-correction and/or a feedback-based approach.

Temperature is another parameter to tune in future experimental studies. To date, the temperature has been held constant at room temperature in our experiments. Testing the temperature dependence of ICBI friction could further verify previous theoretical studies on ageing [41] and also the PTTE model we developed.

Also, materials other than silica might be chosen and used to study ICBI friction. One difficulty in using piranha-treated silica is that the surfaces are quite reactive in ambient environments, and could easily absorb contaminations and thereby become unstable. These properties of piranha-treated silica lead to experimental difficulties and a lack of global reproducibility. For example, frictional properties such as ageing amplitude can vary by 2-3 times, even for the same tip under the same conditions. However, general trends such as the logarithmic ageing law, and the order of magnitude of most quantities, are quite reproducible. If other materials which form interfacial chemical bonds and possess more stable chemical properties could be identified, studies of ICBI friction at the nanoscale will be less difficult and perhaps more revealing.

In addition, nanoindentation experiments could be done to study the effect of creep on ageing at the nanoscale. Our collaborator Prof. David Goldsby obtained some results in this vein. He found that the contact area increases logarithmically with time for diamond-quartz nanoscale contacts in nanoindentation experiments [37] (see Fig. 7.2). In the future, a chemical bonding scenario may be incorporated into the creep experiments to study the combination of these two factors (contact quality and contact quantity) which both lead to ageing.

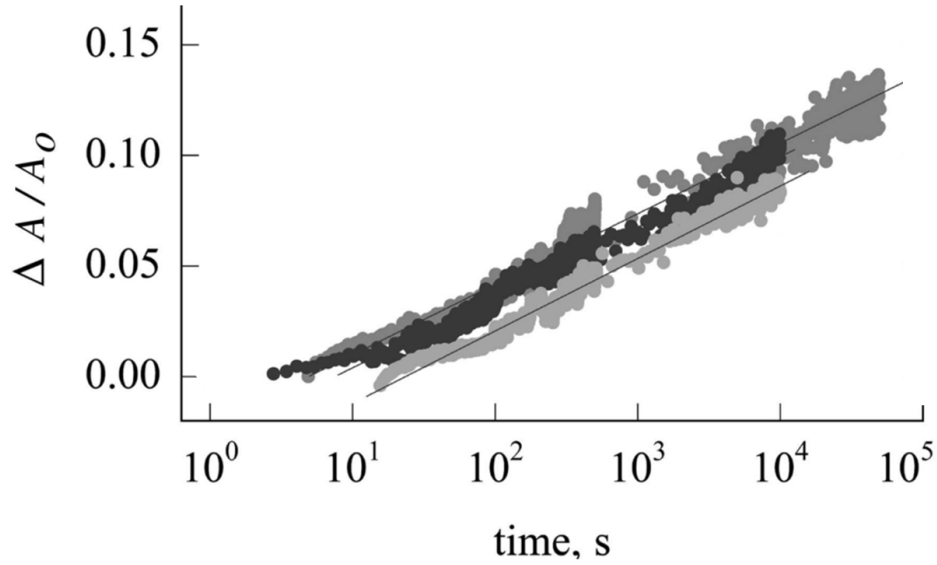


Fig. 7.2: Contact area vs. contact time of quartz in nanoindentation tests. The dark gray, black, and light gray data points correspond to loads of 15 mN, 50 mN and 150 mN respectively. The fractional contact area (the ratio of newly formed area over the initial area) increases with contact time logarithmically between 1 s and 10,000 s. From Goldsby *et al.* [37].

Finally, one important goal for future work is to incorporate the results of ICBI single-asperity friction at the nanoscale into macroscale RSF studies, such as the load and time dependence of ageing, small-time ageing, kinetic friction, and the memory distance. Such a connection between nanoscale and macroscale behavior will be necessary to further our understandings of rock friction and earthquakes beyond empiricism. At present, our collaborators (Prof. Izabela Szlufarska and her student Zhuohan Li) are conducting simulation and analytical research to incorporate our results on the load- and time-dependence of ageing for single-asperity contact into descriptions of the load and time dependence of ageing for multi-asperity contacts.

Although important results have been obtained and much scientific progress has been made in this project, more work remains to be done to achieve the long-term goals of fully establishing physical models/theories to describe RSF behaviors of nanoscale contacts, and understanding their implications for understanding the physical origins of conventional RSF laws.

BIBLIOGRAPHY

1. Tian, K., et al., *Load and Time Dependence of Interfacial Chemical Bond-Induced Friction at the Nanoscale*. Physical Review Letters, 2017. **118**(7): p. 076103.
2. Carpick, R.W. and M. Salmeron, *Scratching the surface: fundamental investigations of tribology with atomic force microscopy*. Chemical Reviews, 1997. **97**(4): p. 1163-1194.
3. Mate, C.M., *Tribology on the small scale*. Oxford University Press, Oxford, 2008.
4. Israelachvili, J.N., *Intermolecular and Surface Forces*. 2011: Academic Press.
5. Shroff, S.S., et al., *Rate-state friction in microelectromechanical systems interfaces: Experiment and theory*. Journal of Applied Physics, 2014. **116**(24): p. 244902.
6. Marone, C., *Laboratory-derived friction laws and their application to seismic faulting*. Annual Review of Earth and Planetary Sciences, 1998. **26**(1): p. 643-696.
7. Hutchings, I. and P. Shipway, *Tribology: friction and wear of engineering materials*. 2017: Butterworth-Heinemann.
8. Schey, J.A., *Tribology in metalworking: friction, lubrication, and wear*. Journal of Applied Metalworking, 1984. **3**(2): p. 173-173.
9. Bhushan, B., *Introduction to tribology*. 2013: John Wiley & Sons.
10. Nosonovsky, M. and B. Bhushan, *Multiscale friction mechanisms and hierarchical surfaces in nano-and bio-tribology*. Materials Science and Engineering: R: Reports, 2007. **58**(3): p. 162-193.
11. Katta, J., et al., *Biotribology of articular cartilage—a review of the recent advances*. Medical engineering & physics, 2008. **30**(10): p. 1349-1363.
12. Jin, Z., et al., (v) *Biotribology*. Current Orthopaedics, 2006. **20**(1): p. 32-40.
13. Taylor, C., *Automobile engine tribology—design considerations for efficiency and durability*. Wear, 1998. **221**(1): p. 1-8.
14. Wallman, C.-G. and H. Åström, *Friction measurement methods and the correlation between road friction and traffic safety: A literature review*. 2001: Statens väg-och transportforskningsinstitut.
15. de Koning, J.J., G. de Groot, and G.J. van Ingen Schenau, *Ice friction during speed skating*. Journal of biomechanics, 1992. **25**(6): p. 565-571.
16. Dieterich, J.H., *Time-dependent friction in rocks*. Journal of Geophysical Research, 1972. **77**(20): p. 3690-3697.
17. Dieterich, J.H., *Modeling of rock friction: 1. Experimental results and constitutive equations*. Journal of Geophysical Research, 1979. **84**(B5): p. 2161.
18. Rice, J.R. and A.L. Ruina, *Stability of steady frictional slipping*. Journal of Applied Mechanics, 1983. **50**(2): p. 343-349.
19. Beeler, N.M., T.E. Tullis, and J.D. Weeks, *The roles of time and displacement in the evolution effect in rock friction*. Geophysical Research Letters, 1994. **21**(18): p. 1987-1990.
20. Berthoud, P., et al., *Physical analysis of the state-and rate-dependent friction law: Static friction*. Physical Review B, 1999. **59**(22): p. 14313.
21. Baumberger, T., P. Berthoud, and C. Caroli, *Physical analysis of the state-and rate-dependent friction law. II. Dynamic friction*. Physical Review B, 1999. **60**(6): p. 3928.

22. Linker, M.F. and J.H. Dieterich, *Effects of variable normal stress on rock friction: Observations and constitutive equations*. Journal of Geophysical Research, 1992. **97**(B4): p. 4923.
23. Linker, M.F. and J.H. Dieterich, *Effects of variable normal stress on rock friction: Observations and constitutive equations*. 1992, Wiley Online Library. p. 4923-4940.
24. Dieterich, J.H., *Constitutive properties of faults with simulated gouge*. Mechanical Behavior of Crustal Rocks: The Handin Volume, 1981. **24**: p. 103-120.
25. Kosloff, D.D. and H.P. Liu, *Reformulation and discussion of mechanical behavior of the velocity - dependent friction law proposed by Dieterich*. Geophysical Research Letters, 1980. **7**(11): p. 913-916.
26. Dieterich, J.H., *Modeling of rock friction: 2. Simulation of preseismic slip*. Journal of Geophysical Research, 1979. **84**(B5): p. 2169.
27. Dieterich, J.H., *Time-dependent friction and the mechanics of stick-slip*. 1978, Springer. p. 790-806.
28. Ruina, A., *Slip instability and state variable friction laws*. Journal of Geophysical Research: Solid Earth, 1983. **88**(B12): p. 10359-10370.
29. Ruina, A.L., *Friction laws and instabilities: A quasistatic analysis of some dry frictional behavior*. 1982. p. 1982.
30. Heslot, F., et al., *Creep, stick-slip, and dry-friction dynamics: Experiments and a heuristic model*. Physical Review E, 1994. **49**(6): p. 4973.
31. Corwin, A.D. and M.P. de Boer, *Frictional aging and sliding bifurcation in monolayer-coated micromachines*. Microelectromechanical Systems, Journal of, 2009. **18**(2): p. 250-262.
32. Corwin, A.D. and M.P. de Boer, *Frictional aging, de-aging, and re-aging in a monolayer-coated micromachined interface*. Physical Review B, 2010. **81**(17): p. 174109.
33. Marone, C., C.B. Raleigh, and C. Scholz, *Frictional behavior and constitutive modeling of simulated fault gouge*. Journal of Geophysical Research: Solid Earth, 1990. **95**(B5): p. 7007-7025.
34. Rice, J.R., *Constitutive relations for fault slip and earthquake instabilities*. Pure and Applied Geophysics, 1983. **121**(3): p. 443-475.
35. Tullis, T.E. and J.D. Weeks, *Constitutive behavior and stability of frictional sliding of granite*, in *Friction and faulting*. 1987, Springer. p. 383-414.
36. Rice, J.R., N. Lapusta, and K. Ranjith, *Rate and state dependent friction and the stability of sliding between elastically deformable solids*. Journal of the Mechanics and Physics of Solids, 2001. **49**(9): p. 1865-1898.
37. Goldsby, D.L., et al., *Nanoindentation creep of quartz, with implications for rate-and state-variable friction laws relevant to earthquake mechanics*. Journal of Materials Research, 2004. **19**(1): p. 357-365.
38. Berthoud, P., et al., *Physical analysis of the state-and rate-dependent friction law: Static friction*. Physical Review B, 1999. **59**(22): p. 14313.
39. Bowden, F. and D. Tabor, *The area of contact between stationary and between moving surfaces*. Proceedings of the Royal Society of London. Series A, Mathematical and Physical Sciences, 1939: p. 391-413.

40. Szlufarska, I., M. Chandross, and R.W. Carpick, *Recent advances in single-asperity nanotribology*. Journal of Physics D: Applied Physics, 2008. **41**(12): p. 123001.
41. Liu, Y. and I. Szlufarska, *Chemical Origins of Frictional Aging*. Physical Review Letters, 2012. **109**(18).
42. Bar - Sinai, Y., et al., *On the velocity - strengthening behavior of dry friction*. Journal of Geophysical Research: Solid Earth, 2014. **119**(3): p. 1738-1748.
43. Scholz, C.H., *The mechanics of earthquakes and faulting*. 2002: Cambridge university press.
44. Karner, S.L. and C. Marone, *Effects of loading rate and normal stress on stress drop and stick-slip recurrence interval*. Geophysical Monograph Series, 2000. **120**: p. 187-198.
45. Shroff, S.S. and M.P. de Boer, *Full Assessment of Micromachine Friction Within the Rate–State Framework: Experiments*. Tribology Letters, 2016. **63**(3): p. 1-15.
46. Shroff, S.S. and M.P. de Boer, *Direct observation of the velocity contribution to friction in monolayer-coated micromachines*. Extreme Mechanics Letters, 2016. **8**: p. 184-190.
47. Shroff, S.S. and M.P. de Boer, *Constant velocity high force microactuator for stick-slip testing of micromachined interfaces*. Journal of Microelectromechanical Systems, 2015. **24**(6): p. 1868-1877.
48. Weeks, J., N. Beeler, and T. Tullis, *Glass is like a rock*. Eos Trans. AGU, 1991. **72**(44): p. 457.
49. Li, Q., et al., *Frictional ageing from interfacial bonding and the origins of rate and state friction*. Nature, 2011. **480**(7376): p. 233-236.
50. Li, A., Y. Liu, and I. Szlufarska, *Effects of Interfacial Bonding on Friction and Wear at Silica/Silica Interfaces*. Tribology Letters, 2014. **56**(3): p. 481-490.
51. Vigil, G., et al., *Interactions of silica surfaces*. Journal of Colloid and Interface Science, 1994. **165**(2): p. 367-385.
52. Wang, X., et al., *Humidity dependence of tribochemical wear of monocrystalline silicon*. ACS applied materials & interfaces, 2015. **7**(27): p. 14785-14792.
53. Plöchl, A. and G. Kräuter, *Wafer direct bonding: tailoring adhesion between brittle materials*. Materials Science and Engineering: R: Reports, 1999. **25**(1): p. 1-88.
54. Iler, K.R., *The chemistry of silica*. Solubility, Polymerization, Colloid and Surface Properties and Biochemistry of Silica, 1979.
55. Dongmo, L., et al., *Experimental test of blind tip reconstruction for scanning probe microscopy*. Ultramicroscopy, 2000. **85**(3): p. 141-153.
56. Sader, J.E., J.W.M. Chon, and P. Mulvaney, *Calibration of rectangular atomic force microscope cantilevers*. Review of Scientific Instruments, 1999. **70**(10): p. 3967-3969.
57. Meyer, E., H.J. Hug, and R. Bennewitz, *Scanning probe microscopy: the lab on a tip*. 2004: Springer.
58. Green, C.P., et al., *Normal and torsional spring constants of atomic force microscope cantilevers*. Review of Scientific Instruments, 2004. **75**(6): p. 1988.
59. Elmer, T.H., *Porous and reconstructed glasses*. ASM International, Engineered Materials Handbook., 1991. **4**: p. 427-432.
60. Lüthi, R., et al., *Nanotribology: an UHV-SFM study on thin films of C60 and AgBr*. Surface science, 1995. **338**(1-3): p. 247-260.

61. Li, Q., K.-S. Kim, and A. Rydberg, *Lateral force calibration of an atomic force microscope with a diamagnetic levitation spring system*. Review of Scientific Instruments, 2006. **77**(6): p. 065105.
62. Liu, X.Z., *Mechanisms controlling friction and adhesion at the atomic length-scale*. 2015: University of Pennsylvania.
63. Chinnery, M., *The stress changes that accompany strike-slip faulting*. Bulletin of the Seismological Society of America, 1963. **53**(5): p. 921-932.
64. Schorlemmer, D., S. Wiemer, and M. Wyss, *Variations in earthquake-size distribution across different stress regimes*. Nature, 2005. **437**(7058): p. 539-542.
65. Beroza, G.C. and T. Mikumo, *Short slip duration in dynamic rupture in the presence of heterogeneous fault properties*. Journal of Geophysical Research: Solid Earth, 1996. **101**(B10): p. 22449-22460.
66. Mo, Y., K.T. Turner, and I. Szlufarska, *Friction laws at the nanoscale*. Nature, 2009. **457**(7233): p. 1116-1119.
67. Mo, Y. and I. Szlufarska, *Roughness picture of friction in dry nanoscale contacts*. Physical Review B, 2010. **81**(3).
68. Schwaderer, P., et al., *Single-molecule measurement of the strength of a siloxane bond*. Langmuir, 2008. **24**(4): p. 1343-1349.
69. Jacobs, T.D. and R.W. Carpick, *Nanoscale wear as a stress-assisted chemical reaction*. Nature nanotechnology, 2013. **8**(2): p. 108-112.
70. Gibbs, G., *The Thermodynamics of Thermally - Activated Dislocation Glide*. physica status solidi (b), 1965. **10**(2): p. 507-512.
71. Taylor, G., *Thermally-activated deformation of BCC metals and alloys*. Progress in materials science, 1992. **36**: p. 29-61.
72. Rhee, S., *Surface energies of silicate glasses calculated from their wettability data*. Journal of Materials Science, 1977. **12**(4): p. 823-824.
73. Procelewska, J., et al., *Activation volume measurement for CH activation. Evidence for associative benzene substitution at a platinum (II) center*. Inorganic chemistry, 2002. **41**(11): p. 2808-2810.
74. Ogletree, D., R.W. Carpick, and M. Salmeron, *Calibration of frictional forces in atomic force microscopy*. Review of Scientific Instruments, 1996. **67**(9): p. 3298-3306.
75. Varenberg, M., I. Etsion, and G. Halperin, *An improved wedge calibration method for lateral force in atomic force microscopy*. Review of Scientific Instruments, 2003. **74**(7): p. 3362-3367.
76. Gao, J., et al., *Frictional forces and Amontons' law: from the molecular to the macroscopic scale*. The Journal of Physical Chemistry B, 2004. **108**(11): p. 3410-3425.
77. Lessel, M., et al., *Impact of van der Waals Interactions on Single Asperity Friction*. Physical Review Letters, 2013. **111**(3): p. 035502.
78. Flater, E.E., W.R. Ashurst, and R.W. Carpick, *Nanotribology of octadecyltrichlorosilane monolayers and silicon: self-mated versus unmated interfaces and local packing density effects*. Langmuir, 2007. **23**(18): p. 9242-9252.
79. Dieterich, J.H. and B.D. Kilgore, *Direct observation of frictional contacts: New insights for state-dependent properties*. Pure and Applied Geophysics, 1994. **143**(1-3): p. 283-302.

80. Dieterich, J.H. and B.D. Kilgore, *Imaging surface contacts: power law contact distributions and contact stresses in quartz, calcite, glass and acrylic plastic*. Tectonophysics, 1996. **256**(1): p. 219-239.
81. Nagata, K., M. Nakatani, and S. Yoshida, *Monitoring frictional strength with acoustic wave transmission*. Geophysical Research Letters, 2008. **35**(6).
82. Derjaguin, B.V., V.M. Muller, and Y.P. Toporov, *Effect of contact deformations on the adhesion of particles*. Journal of Colloid and Interface Science, 1975. **53**(2): p. 314-326.
83. Johnson, K., *Non-Hertzian contact of elastic spheres (P.26)*. (book) The mechanics of contact between deformable bodies, 1975.
84. Carpick, R.W., D.F. Ogletree, and M. Salmeron, *A general equation for fitting contact area and friction vs load measurements*. Journal of Colloid and Interface Science, 1999. **211**(2): p. 395-400.
85. Grierson, D.S., E.E. Flater, and R.W. Carpick, *Accounting for the JKR–DMT transition in adhesion and friction measurements with atomic force microscopy*. Journal of adhesion science and technology, 2005. **19**(3-5): p. 291-311.
86. Greenwood, J. *Adhesion of elastic spheres*. in *Proceedings of the Royal Society of London A: Mathematical, Physical and Engineering Sciences*. 1997: The Royal Society.
87. Frye, K.M., *Effect of humidity on granular friction at room temperature*. Journal of Geophysical Research, 2002. **107**(B11): p. 1-13.
88. Gnecco, E., et al., *Velocity dependence of atomic friction*. Physical Review Letters, 2000. **84**(6): p. 1172-1175.
89. Riedo, E., et al., *Interaction potential and hopping dynamics governing sliding friction*. Physical Review Letters, 2003. **91**(8): p. 084502.
90. Liu, X.-Z., et al., *Dynamics of Atomic Stick-Slip Friction Examined with Atomic Force Microscopy and Atomistic Simulations at Overlapping Speeds*. Physical Review Letters, 2015. **114**(14): p. 146102.
91. Mazo, J.J., et al., *Time Strengthening of Crystal Nanocontacts*. Physical Review Letters, 2017. **118**(24): p. 246101.
92. Li, Q., et al., *Speed dependence of atomic stick-slip friction in optimally matched experiments and molecular dynamics simulations*. Physical Review Letters, 2011. **106**(12): p. 126101.
93. Baumberger, T., F. Heslot, and B. Perrin, *Crossover from creep to inertial motion in friction dynamics*. 1994.
94. <Laboratory_derived friction laws and their application to seismic faulting_Marone.pdf>.
95. Baumberger, T., et al., *Nonlinear analysis of the stick-slip bifurcation in the creep-controlled regime of dry friction*. Physical Review E, 1995. **51**(5): p. 4005.
96. Shroff, S.S. and M.P. de Boer, *Full Assessment of Micromachine Friction Within the Rate–State Framework: Experiments*. Tribology Letters, 2016. **63**(3): p. 31.
97. Yoshizawa, H. and J. Israelachvili, *Fundamental mechanisms of interfacial friction. 2. Stick-slip friction of spherical and chain molecules*. The Journal of Physical Chemistry, 1993. **97**(43): p. 11300-11313.
98. Socoliuc, A., et al., *Transition from Stick-Slip to Continuous Sliding in Atomic Friction: Entering a New Regime of Ultralow Friction*. Physical Review Letters, 2004. **92**(13).

99. Sang, Y., M. Dubé, and M. Grant, *Thermal effects on atomic friction*. Physical Review Letters, 2001. **87**(17): p. 174301.
100. Dudko, O.K., et al., *Beyond the conventional description of dynamic force spectroscopy of adhesion bonds*. Proceedings of the National Academy of Sciences, 2003. **100**(20): p. 11378-11381.
101. Barel, I., et al., *Temperature Dependence of Friction at the Nanoscale: When the Unexpected Turns Normal*. Tribology Letters, 2010. **39**(3): p. 311-319.
102. Barel, I., et al., *Multibond Dynamics of Nanoscale Friction: The Role of Temperature*. Physical Review Letters, 2010. **104**(6).
103. Mate, C.M., et al., *Atomic-scale friction of a tungsten tip on a graphite surface*. Physical Review Letters, 1987. **59**(17): p. 1942.
104. Rabinowicz, E., *The intrinsic variables affecting the stick-slip process*. 1958, IOP Publishing. p. 668.
105. Carpick, R.W., D.F. Ogletree, and M. Salmeron, *Lateral stiffness: A new nanomechanical measurement for the determination of shear strengths with friction force microscopy*. Applied Physics Letters, 1997. **70**(12): p. 1548.
106. Omori, F., *On the after-shocks of earthquakes*. Vol. 7. 1894: The University.
107. Teng-Fong, W. and Z. Yusheng, *Effects of load point velocity on frictional instability behavior*. Tectonophysics, 1990. **175**(1): p. 177-195.
108. Berman, A., W. Ducker, and J. Israelachvili, *Experimental and theoretical investigations of stick-slip friction mechanisms*, in *Physics of sliding friction*. 1996, Springer. p. 51-67.
109. Watts, J.F. and J. Wolstenholme, *An introduction to surface analysis by XPS and AES*. 2003.
110. Stöckle, R.M., et al., *Nanoscale chemical analysis by tip-enhanced Raman spectroscopy*. Chemical physics letters, 2000. **318**(1): p. 131-136.
111. Pettinger, B., et al., *Nanoscale probing of adsorbed species by tip-enhanced Raman spectroscopy*. Physical Review Letters, 2004. **92**(9): p. 096101.
112. Batteas, J.D., M.K. Weldon, and K. Raghavachari, *Bonding and Interparticle Interactions of Silica Nanoparticles*, in *Nanotribology*. 2003, Springer. p. 387-398.